



**Max-Planck-Institut für Intelligente Systeme**  
(ehemals Max-Planck-Institut für Metallforschung)  
Stuttgart

---

## **Diffraction analysis of materials in a state of stress: elastic loading and phase transformations**

Margaret Kolbe Annellen Koker

Dissertation  
an der  
**Universität Stuttgart**

---

Bericht Nr. 244  
Januar 2013



# Diffraction analysis of materials in a state of stress: elastic loading and phase transformations

Von der Fakultät Chemie an der Universität Stuttgart zur Erlangung  
der Würde eines Doktors der Naturwissenschaften (Dr. rer. nat.)  
genehmigte Abhandlung

vorgelegt von

Margaret Kolbe Annellen Koker

aus Lafayette, Indiana, U.S.A.

Hauptberichter: Prof. Dr. Ir. E. J. Mittemeijer  
Mitberichter: Prof. Dr. J. Bill  
Prüfungsvorsitzender: Prof. Dr. Th. Schleid

Tag der Einreichung: 20.11.2012  
Tag der mündlichen Prüfung: 25.01.2013

MAX-PLANCK-INSTITUT FÜR INTELLIGENTE SYSTEME  
(EHEMALS MAX-PLANCK-INSTITUT FÜR METALLFORSCHUNG)  
INSTITUT FÜR MATERIALWISSENSCHAFT DER UNIVERSITÄT STUTTGART

Stuttgart 2012

*To the achievement of girls in science and math*



# Contents

<b>1</b>	<b>Introduction</b>	<b>1</b>
1.1	General introduction . . . . .	1
1.2	Stress analysis using diffraction . . . . .	2
1.2.1	The $\sin^2 \psi$ method . . . . .	4
1.2.2	Specimen curvature from rocking curves . . . . .	4
1.3	Mechanical grain interaction . . . . .	5
1.3.1	Grain-interaction models . . . . .	5
1.3.2	X-ray diffraction-line broadening induced by external mechanical elastic loading . . . . .	7
1.4	Effect of stress on phase transformations: equiatomic NiTi . . . . .	7
1.4.1	Martensitic transformation in shape memory NiTi . . . . .	8
1.4.2	The shape memory effect and psuedoelasticity . . . . .	9
1.4.3	Diffraction studies of equiatomic NiTi . . . . .	10
1.5	Focus of thesis . . . . .	11
1.6	Methodology . . . . .	11
1.6.1	Thin film preparation . . . . .	12
1.6.2	Computational application of grain-interaction models . . . . .	12
1.6.3	XRD experiments . . . . .	13
1.6.4	Rietveld analysis . . . . .	14
1.7	Outline of Thesis . . . . .	15
<b>2</b>	<b>Elastic mechanical grain interactions in polycrystalline materials; analysis by diffraction-line broadening</b>	<b>23</b>
2.1	Introduction . . . . .	24
2.2	Grain-interaction models . . . . .	26
2.3	Calculation of diffraction-line broadening induced by external loading . . . . .	29
2.3.1	Procedure . . . . .	29
2.3.2	Preliminary notes on lattice strain induced broadening in the case of isotropic grain interaction . . . . .	32
2.3.3	Material and model parameters . . . . .	33
2.4	Lattice-strain distributions predicted by grain-interaction models . . . . .	35

2.4.1	Tensile vs. compressive states of stress; scaling of line broadening . . . . .	37
2.4.2	States of loading . . . . .	39
2.4.3	Degree of intrinsic elastic anisotropy . . . . .	42
2.4.4	Isotropic grain interactions . . . . .	42
2.4.5	Anisotropic grain interactions . . . . .	44
2.4.6	Preferred orientation . . . . .	46
2.4.7	$H00$ and $HHH$ reflections . . . . .	50
2.5	Strain variation predictions by finite element analysis . . . . .	51
2.6	General discussion . . . . .	58
2.7	Conclusions . . . . .	59
2.8	Appendix: Definition of grain orientation for FEA calculations . . . . .	61
<b>3</b>	<b>Measurement of x-ray diffraction-line broadening induced by elastic mechanical grain interaction</b>	<b>67</b>
3.1	Introduction . . . . .	68
3.2	Theoretical background . . . . .	69
3.2.1	Reference frames and calculations of diffraction averages . . . . .	69
3.2.2	Lattice strain vs. mechanical stress relationships . . . . .	72
3.2.3	Grain interaction and diffraction-line broadening . . . . .	73
3.3	Experimental procedures . . . . .	73
3.3.1	Loading set-up . . . . .	74
3.3.1.1	Biaxially rotationally symmetric loading . . . . .	74
3.3.1.2	Uniaxial loading . . . . .	75
3.3.2	Materials . . . . .	75
3.3.2.1	Biaxially rotationally symmetric loaded specimens . . . . .	76
3.3.2.2	Uniaxially loaded specimens . . . . .	77
3.3.3	Evaluation of diffraction data . . . . .	77
3.4	Results and discussion . . . . .	78
3.5	Conclusions . . . . .	88
<b>4</b>	<b>X-ray diffraction study of the temperature-induced reverse martensitic transformation in near-equiatomic NiTi shape memory thin films</b>	<b>93</b>
4.1	Introduction; thermal cycling and stress development . . . . .	94
4.2	Experimental procedures . . . . .	95
4.2.1	Film preparation and characterization . . . . .	95
4.2.2	Diffraction experiments . . . . .	97
4.2.2.1	Reference frames . . . . .	97
4.2.2.2	XRD measurements . . . . .	97
4.3	Results and discussion . . . . .	101
4.3.1	Phase fraction, lattice parameters, crystallite size, and microstrain; Rietveld refinements . . . . .	103

4.3.2	Macrostressses . . . . .	107
4.3.2.1	Stress in austenite; diffraction analysis . . . . .	107
4.3.2.2	Overall macroscopic stress in the thin film; curvature mea- surements . . . . .	110
4.3.2.3	Stress in martensite; mechanical equilibrium of the film . .	112
4.4	Conclusions . . . . .	113
<b>5</b>	<b>Summary</b>	<b>121</b>
<b>6</b>	<b>Zusammenfassung</b>	<b>127</b>
	<b>List of Publications</b>	<b>133</b>
	<b>Acknowledgments</b>	<b>135</b>
	<b>Curriculum Vitae</b>	<b>137</b>
	<b>Declaration of Authorship</b>	<b>139</b>



# Chapter 1

## Introduction

### 1.1 General introduction

Stress plays a significant role in material behavior. In the absence of external loading, most materials experience internal stresses, termed residual stress, which is often the result of the thermomechanical history (e.g. processing and forming). In many cases, residual stress leads to undesirable effects, significantly influencing the yield and fatigue strength of machined parts. Stress (and stress gradients) in parts can lead to cracking, peeling, or distortion of components. However, at times, a residual stress (gradient) can improve the quality and the lifetime of such parts. An example of this is the introduction of surface hardening (such as via shot-peening or chemical treatments such as nitriding) of materials such as steel, where the induced compressive stress on the surface provides resistance to cracking. It can be concluded that understanding the stress in a polycrystalline material is important for the analysis of the properties and the behavior of the material.

As the magnitude and state of stress in a material are very important, numerous methods exist for measuring and predicting stress yielding in a material based on its material properties (e.g. Young's modulus, yield strength, etc.). Various methods are also available for the modeling (or predicting) the stress and strain in a body as a function of thermomechanical processing or environmental conditions.

In most cases, the individual crystallites in an aggregate are intrinsically elastically anisotropic; however, in the absence of texture (i.e. grains are randomly oriented in the bulk), the grains form an elastically, macroscopically isotropic body. This means a polycrystalline aggregate will macroscopically comply isotropically under external elastic loading. Such a body is termed "quasi-isotropic" [1]. Yet it should be recognized that the behavior of each grain is dependent on its orientation with respect to the applied load. The interaction of grains in the loaded aggregate leads to distributions of stress and strain [2]; each individual crystallite is confined by its neighbors, not allowing it to freely deform. Therefore, knowledge of the strain variation in a loaded body can be crucial for understanding material properties.

The single-crystal elastic constants can be used to define the degree of anisotropy of the

material's elastic behavior defined by the parameter  $\mathcal{A}$  (known as the Zener's anisotropy ratio), meaning the compliance of a single grain is strongly dependent on the direction of the applied loading:

$$\mathcal{A} = \frac{2(s_{11} - s_{12})}{s_{44}} = \frac{2 \cdot c_{44}}{c_{11} - c_{12}} \quad (1.1)$$

where  $s_{ij}$  and  $c_{ij}$  are the single-crystal elastic constants for compliance and stiffness, respectively. If the elastic response of an isolated grain for a specific material is independent of its orientation with respect to the (anisotropic) state of loading, which holds for tungsten, the material is called intrinsically elastically isotropic ( $\mathcal{A} = 1$ ). For such materials, all grains experiencing the same imposed stress state will exhibit identical (average) lattice strains, independent of grain orientation.

## 1.2 Stress analysis using diffraction

X-ray diffraction (XRD) is a common non-destructive technique for analyzing the stress in a material from the lattice strain. When the X-ray beam hits a specimen, the beam is diffracted in a manner unique to the crystallographic structure of the material. This method can be used to extract the (average) spacing of lattice planes in a crystalline material and the fitting of the unit cell [3]. The measured diffraction line is the result of numerous contributing factors. The angle between the diffraction and the incident beam  $2\theta$  can be related to the lattice spacing  $d^{\text{HKL}}$  of a specific reflection HKL as a function of the radiation wavelength  $\lambda$ :

$$\lambda = 2d^{\text{HKL}} \sin \theta. \quad (1.2)$$

This relationship is termed Bragg's law [4]. The lattice spacing for a cubic material is calculated as a function of the HKL describing the lattice planes and the lattice parameter  $a$ :

$$d^{\text{HKL}} = a \cdot \sqrt{H^2 + K^2 + L^2}. \quad (1.3)$$

The measured lattice spacing  $d$  is a function of the HKL reflection and the orientation of the diffraction vector, defined by  $\phi$  and  $\psi$ .

Any variation from the *perfect* diffraction conditions can cause the measured peaks to both broaden and shift in  $2\theta$  [3]. Grains that are less than infinitely large (especially nanocrystals), defect structures in the crystals, non-ideal instrumental conditions, and variation of strain (lattice spacing) within the diffraction volume can all contribute to an increased width of the diffraction lines.

Measuring the lattice spacing as a function of applied load provides information about strain on the granular level. A strain distribution in the aggregate induces a variation in lattice-plane spacing, which results in broadening and possibly a shift in  $2\theta$  of the measured x-ray diffraction (XRD) lines [3]. An average strain for grains sharing a specified diffraction vector will result in a shift of the diffraction line. The induced peak shift is

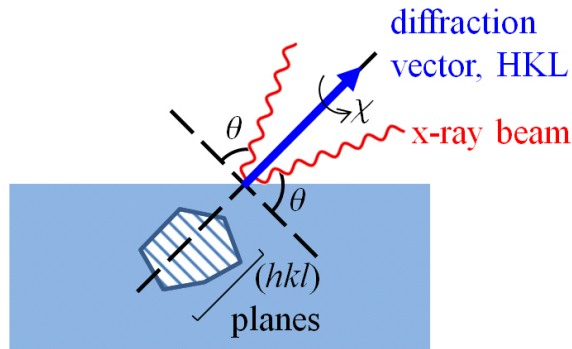


Figure 1.1: Schematic of single grain diffraction within a polycrystalline aggregate, also demonstrating the degree of grain rotational freedom, in a diffraction experiment, given as the angle  $\chi$ , defining the rotation about the  $HKL$  diffraction vector, which is perpendicular to a set of  $(hkl)$  planes.

well understood and can be described using Bragg's law (Equation 1.2) and by expressing the elastic strain in terms of the average lattice strain of the diffracting crystallites [2, 5, 6]. Studies have been performed to relate the (average) lattice strain to macroscopic (residual) stress in a specimen using x-ray diffraction (XRD) techniques [7, 8]. The local stress variation in macroscopically elastically loaded polycrystalline bodies (consisting of elastically anisotropic grains) can affect diffraction-line broadening.

Diffraction-line broadening has been a topic of great interest since the discovery of x-ray diffraction by crystal. The broadening of diffraction lines occurs in different manners (e.g. symmetrically versus asymmetrically, change in shape, etc.) due to (and depending on) a number of causes, e.g. smallness of crystallite size and microstrain. Much of the research focusing on diffraction-line broadening works to separate the numerous contributions and then draw conclusions about the microstructure of a specimen. The measured diffraction line  $h(2\theta)$  can be thought of as a convolution of the intrinsically broadened diffraction line  $f(2\theta)$  with the instrumental broadening contribution  $g(2\theta)$  [9]:

$$h(2\theta) = g(2\theta) \otimes f(2\theta). \quad (1.4)$$

Identifying and extracting the individual intrinsic profile contributions is non-trivial. The intrinsic broadening is also thought of as a convolution of several broadening contributions which result from the microstructure of the specimen. Much work in the field of strain variation (namely that which occurs within individual grains) approximates the microstrain contribution as a Gaussian-shaped line profile. However, realistically, a combinations of both Gaussian- and Lorentzian-shaped profiles have been observed [10]. For a rigorous discussion on (also line-profile shape of) micro-(lattice-)strain broadening, see Reference [11].

### 1.2.1 The $\sin^2 \psi$ method

Strain induced by elastic loading is generally defined as a change in length over the initial length. The (average) change in interatomic spacing along the diffraction vector will be used to define (average) lattice strain:

$$\epsilon_{\phi,\psi}^{\text{HKL}} = \frac{d_{\phi,\psi}^{\text{HKL}} - d_o^{\text{HKL}}}{d_o^{\text{HKL}}}, \quad (1.5)$$

where  $d_o^{\text{HKL}}$  is the lattice-plane spacing in the absence of stress, which is dependent, among other things, on the material, HKL, and temperature. The lattice-plane spacing is directly calculated from the diffraction-line position, as indicated in Equation 1.2. In addition to depending on the applied loading (magnitude and state), the lattice spacing  $d_{\phi,\psi}^{\text{HKL}}$  is dependent on the HKL reflection, as well as the measurement angles  $\psi$  and  $\phi$ , the tilting and rotation of the sample, respectively [6].

In terms of the diffraction geometry, the average lattice strain along the diffraction vector can be expressed as:

$$\epsilon_{\phi,\psi}^{\text{HKL}} = F_{ij}^{\text{HKL}}(\phi, \psi) \cdot \langle \sigma_{ij} \rangle. \quad (1.6)$$

where  $F_{ij}^{\text{HKL}}(\phi, \psi)$  are the x-ray diffraction *stress factors* and  $\langle \sigma_{ij} \rangle$  describes the loading-induced state of mechanical stress. For a proof of this relationship, see Reference [5]. This relationship remains valid also for macroscopically elastically anisotropic bodies (e.g. textured). If a material is untextured, and found to behave macroscopically isotropically, the following relationship can be derived by relating the XRD measurement geometry to the average lattice strain  $\epsilon_{\phi,\psi}^{\text{HKL}}$  along the diffraction vector for a planar state of stress:

$$\epsilon_{\phi,\psi}^{\text{HKL}} = \frac{1}{2} S_2^{\text{HKL}} [\cos^2 \phi \cdot \sigma_{11} + \sin(2\phi) \sigma_{12} + \sin^2 \phi \cdot \sigma_{22}] \sin^2 \psi + S_1^{\text{HKL}} (\sigma_{11} + \sigma_{22}), \quad (1.7)$$

where  $S_1^{\text{HKL}}$ ,  $\frac{1}{2} S_2^{\text{HKL}}$  are the (x-ray) diffraction *elastic constants* and  $\sigma_{11}$ ,  $\sigma_{12}$ ,  $\sigma_{22}$  define the planar macroscopic stress state in the body [12].

For a uniaxial ( $\sigma_{11} \neq 0$ ,  $\sigma_{12} = \sigma_{22} = 0$ ) or a biaxially, rotationally symmetric state of stress ( $\sigma_{\parallel} \equiv \sigma_{11} = \sigma_{22} \neq 0$ ,  $\sigma_{12} = 0$ ), which are the two stress states investigated in this thesis, the expression given in Equation 1.7 can be significantly simplified. A linear fit of the strain data  $\epsilon_{\phi,\psi}^{\text{HKL}}$ , for a fixed angle  $\phi$ , plotted as a function of  $\sin^2 \psi$  can be used to calculate the stress in the material. The uniaxial and biaxially, rotationally symmetric states of stress will be applied and discussed further in the experiments and calculations discussed in Chapters 2-4.

### 1.2.2 Specimen curvature from rocking curves

Residual stress in a substrate-bound thin film will cause the substrate-film system to bend. For a thin film (thin being relative in comparison to the substrate thickness), the



strain  $\epsilon$  due to curvature is given by [13]:

$$\epsilon = \frac{H^2}{6h} \cdot \left( \frac{1}{R} \right), \quad (1.8)$$

where  $h$  is the thickness of the film,  $H$  is the thickness of the substrate, and  $R$  is the radius of curvature, assuming a flat substrate when the magnitude of stress is null [14].

Of course, stress calculated using specimen curvature is always a relative value. Even a completely strain-free substrate will have some characteristic curvature, which will change as soon as the film is deposited due to residual stress. A complimentary method for measuring stress (or information about the pre-deposition curvature of the substrate) is therefore always necessary to know the absolute value found using curvature. Using Hooke's law, the change in stress which causes a change in curvature (from  $R_1$  to  $R_2$ ) is defined as:

$$\Delta\sigma = M \cdot \epsilon = M \cdot \frac{H^2}{6h} \cdot \left( \frac{1}{R_2} - \frac{1}{R_1} \right), \quad (1.9)$$

where  $M$  is the biaxial modulus of the substrate (defined from the Young's modulus  $E$  and Poisson's ratio  $\nu$ ).

Curvature can be investigated by making rocking curve scans of an HKL reflection (i.e. the detector position is fixed at  $2\theta$  and the specimen is rocked in a small range of  $\omega$  angles for  $\omega \approx \frac{2\theta}{2}$ ) while transversing the film. The shift in peak position  $\Delta\omega$ , when combined with the distance between measurement locations on the specimen  $\Delta x$ , can be used to assess the curvature  $R$  [15]:

$$R = \frac{\Delta x}{2 \sin\left(\frac{\Delta\omega}{2}\right)}. \quad (1.10)$$

This method can be used for both crystalline and amorphous films deposited on (usually single-crystal) substrates.

## 1.3 Mechanical grain interaction

### 1.3.1 Grain-interaction models

Several elastic grain-interaction models (described in the following section) can be used to calculate that the average lattice strain (or stress factors and diffraction elastic constants) for polycrystalline specimens under macroscopic loading. Each model uses a set of constitutive assumptions which enforce certain conditions within the aggregate in order to calculate the stress and strain of a crystallite based on its orientation and the macroscopic loading state. The validity of each model is highly dependent on the specimen characteristics (e.g. surface effects, non-spherical grain shape, etc.). Models can be classified into two separate categories: *isotropic* (equality of grain interactions in all directions) and *anisotropic* (direction dependent grain interactions). A summary of the commonly applied models can be found in Table 2.1 (Chapter 2). These models vary

greatly in their complexity and in their applicability.

The Voigt [16] and Reuss [17] models represent the extreme cases for (isotropic) grain interactions, providing the lower and upper bounds in strain, respectively. The Voigt assumptions follow that all crystallites in the body are tightly connected, meaning they must deform together. This results in all grains being under identical state of strain (*isostrain*) in the specimen frame of reference. The opposite approach is taken for the Reuss model. The crystallites in the aggregate are assumed to deform freely, resulting in all grains under identical state of stress (*isostress*) in the specimen frame of reference. A major advantage to these models is that they can be solved analytically.

The effective grain-interaction models use linear combinations of the results found according to the extreme Voigt and Reuss models in an attempt to more accurately match experimental values. The Neerfeld-Hill [18, 19] model is an isotropic model, which uses the arithmetic averages of the Voigt and Reuss bounds. Both the Vook-Witt [20, 21] and inverse Vook-Witt [22] imply different grain-interaction assumptions for directions parallel and perpendicular to the specimen surface, making them anisotropic grain-interaction models. For the Vook-Witt model, the *isostress* conditions are enforced perpendicular to the surface (i.e. Reuss) and *isostrain* restrictions are made parallel to the surface (i.e. Voigt). The inverse Vook-Witt model enforces exactly the opposite conditions (i.e. *isostrain* perpendicular to the surface and *isostress* parallel to the surface).

Each of the above discussed models does not enforce continuity between the grains. The Eshelby-Kröner [23, 24] model, however, enforces continuity between each crystallite and the aggregate, taken as a representative effective medium, i.e. an homogeneous body with its properties being defined as averages over all grains in the aggregate. All of the grains of identical orientation are treated as one. A grain shape factor  $\eta$  can be introduced to deal with non-spherical grains (morphological texture) [25]. The solutions from the Eshelby-Kröner model are much more representative of the average lattice strain observed experimentally (in comparison to models such as the Voigt and Reuss, but not better than the results from the Neerfeld-Hill model), but the calculation process is rather computationally intensive.

Similar models also exist to describe grain interaction during plastic deformation. The Taylor model (based on the same *isostrain* assumptions as the Voigt models) is the true upper bound [26]. The Sachs model is comparable to the Reuss model, acting as the lower bound, as grains are assumed to have equivalent stress states (in the specimen frame of reference). More complex models also exist which have additional assumptions to provide more accurate approximations of the plastic deformation. Such models integrate slip and dislocation movement within the grains, as well as enforcing continuity the individual grains and the aggregate. These models, however, much like the elastic grain-interaction models, do *not* incorporate local heterogeneity of the neighborhood of each grain in a quasi-isotropic aggregate.

Constricting the discussion to elastic loading only, through the application of one

of the elastic grain-interaction models, the average lattice strain as a function of grain orientation with respect to the aggregate (in the specimen frame of reference) can be calculated for all possible grain orientations. The calculated information for lattice strain can also be applied to predict the expected diffraction-line broadening by convoluting diffraction peaks with a function describing the strain distribution within a set of grains sharing a common diffraction vector. (Refer to Section 1.6.2.)

### 1.3.2 X-ray diffraction-line broadening induced by external mechanical elastic loading

A diffraction line includes information about all ( $hkl$ ) lattice planes lying perpendicular to the diffraction vector. As shown in Figure 1.1, this leaves a degree of freedom, indicated by the angle  $\chi$ . Variation in the lattice parameter for grains sharing the same diffraction vector, within the diffraction volume, will result in diffraction-line broadening. Therefore, diffraction lines will broaden due to the strain distribution induced by external mechanical loading. This broadening is a result of the anisotropic behavior of the individual grains. The broadening is fully reversible upon the unloading of the specimen.

Theoretical calculations of the strain variation in a quasi-isotropic polycrystalline aggregate provide support that diffraction-line broadening results from elastic loading [27]. The calculated broadening (according to the isotropic elastic grain-interaction models) have been compared directly with experimentally measurable diffraction-line broadening during *in situ* loading experiments [28, 29].

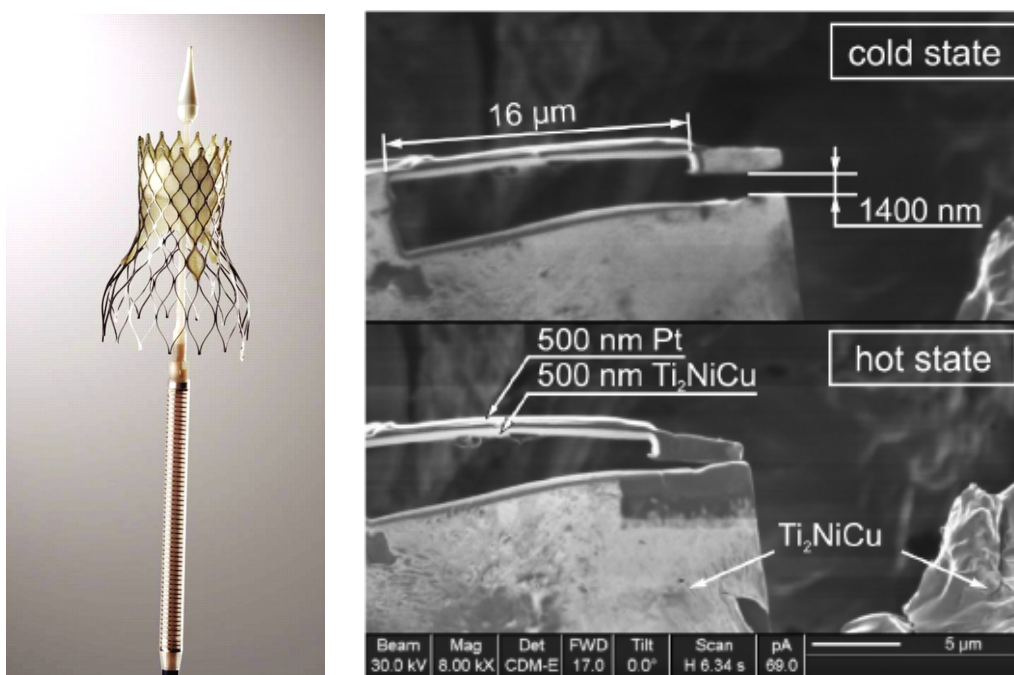
It has been shown computationally that only the deviatoric stress (not hydrostatic stress) will contribute to the induced diffraction-line broadening, when isotropic grain interaction is considered [28]. The broadening (and lattice strain variation) is strongly dependent on HKL [27–29].) Reflections which satisfy H00 or HHH, for cubic materials, do not broaden under applied elastic loading when grain interactions are isotropic. Texture is also an important factor in diffraction-line broadening (for both isotropic and anisotropic grain interaction), as a grain's anisotropic behavior is clearly dependent on the orientation of the grains in the aggregate. (This discussion is presented in Chapters 2 and 3.)

The broadening of diffraction lines, i.e. by a comparison of calculations and experiments, can be used to gain fundamental insight into the intergranular (and even intragranular) mechanics in an aggregate.

## 1.4 Effect of stress on phase transformations: equiatomic NiTi

Shape memory properties are characteristic of a unique set of materials which can undergo seemingly severe and permanent deformation, yet still return to their original state through a load and temperature induced phase transformation. This special behavior was first documented for an Au-Cd alloy in 1951 [30]. Additional shape memory materials

were discovered in the following years, including equiatomic NiTi in 1963 [31]. The high work output to volume ratio and the more or less perfect reversibility makes NiTi an ideal candidate for an ever-growing number of applications, e.g. see References [32–35]. Near equiatomic compositions of NiTi are one of the of the most widely researched and applied shape memory materials due to its high strength and relatively simple composition. Moreover, the functioning temperature range can be tuned by thermomechanical treatments, making the application in a wide range of environments possible. This material is used in the aeronautical field as well as for medical applications. Recently, there is a large interest in small scale components made from NiTi for the construction of microelectromechanical systems (MEMS). Figure 1.2 shows some specialized applications of NiTi shape memory alloys.



(a) Stent used to keep arteries open after a heart attack. Image taken from Reference [34].

(b) Microtweezers made from NiTi-based alloy where components move and mechanically function with thermal variation. Image taken from Reference [35].

Figure 1.2: Examples of the implementation of NiTi shape memory alloys

### 1.4.1 Martensitic transformation in shape memory NiTi

There are two prominent phases of interest in near equiatomic NiTi alloys: *austenite* and *martensite* [36]. NiTi shape memory alloys undergo a martensitic transformation between the austenite and martensite phases. Both thermal and mechanical loading can be imposed on the material to induce the phase transformation [37]. The massive, first-

order martensitic transformation is known to be diffusionless and athermal [38].

Austenite, the high temperature phase, has a cubic structure; the martensitic phase has a monoclinic crystalline structure and occurs at low temperatures. During cooling, it is possible for an intermediate phase, coined R-phase due to its rhombohedral unit cell, to form before martensite does. The appearance of this intermediate phase complicates the transformation and it will not be discussed in this work. Full crystallographic characterization of the austenite, martensite, and intermediate R-phase (and some of the common precipitates such as  $\text{Ti}_2\text{Ni}$ ) have been performed in numerous studies [39–41].

The martensitic phase transformation in NiTi is realized through a shear and a rotation of the cubic (austenite) unit cell [36]. As the transformation is diffusionless, the displacement of individual atoms is minimal, not exceeding the atomic distance. The forward transformation is realized, in a sense, by a stretching of the cubic (austenite) lattice along the  $z$ -axis (lengthening of  $c$ ) and a shearing of the unit cell to slightly increase the angle  $\beta$ . Twelve unique variants of martensite can form during the cubic to monoclinic phase transformation. These variants form in such a manner as to reduce the overall stress of the material, giving it the title self-accommodating. Often, multiple twin bands are formed within a single cubic austenite phase. This process leads to martensite being referred to as self-accommodating, also providing the mechanism for shape memory. The martensitic transformation in NiTi shape memory alloys is heavily influenced by the stress state (and temperature) of the material [36].

## 1.4.2 The shape memory effect and psuedoelasticity

Martensitic shape memory materials exhibit two unique behaviors: *pseudoelasticity* (also called super elasticity) and *shape memory effect* [37]. These characteristic behaviors of near-equiatomic NiTi alloys are driven by the (forward or reverse) martensitic transformation of the material. A schematic of the understanding of the microstructural changes for these two phenomena is shown in Figure 1.3.

*Pseudoelasticity* can be observed when austenite (high temperature phase) is loaded. Instead of resulting in permanent deformation of the material, applied loading induces the formation of a single variant of martensite [37]. This phase is, of course, unstable at high temperatures in the absence of loading. So, upon unloading, the material transforms entirely back to its undeformed parents phase (austenite). Permanent deformation can be induced in the martensite phase if loading exceeds the elastic loading limit. However, in both the SME and PSE, induced macroscopic strain up to 8-10% are still fully reversible [37].

The *shape memory effect* occurs at low temperatures, i.e. characteristic behavior of the martensite phase. During deformation, the material *detwins* to the most favorable monoclinic variant with respect to the applied load [36]. When the external loading is removed, the material will remain in this deformed state. The material must then be heated to induce the reverse martensitic transformation. This erases the deformation, resulting

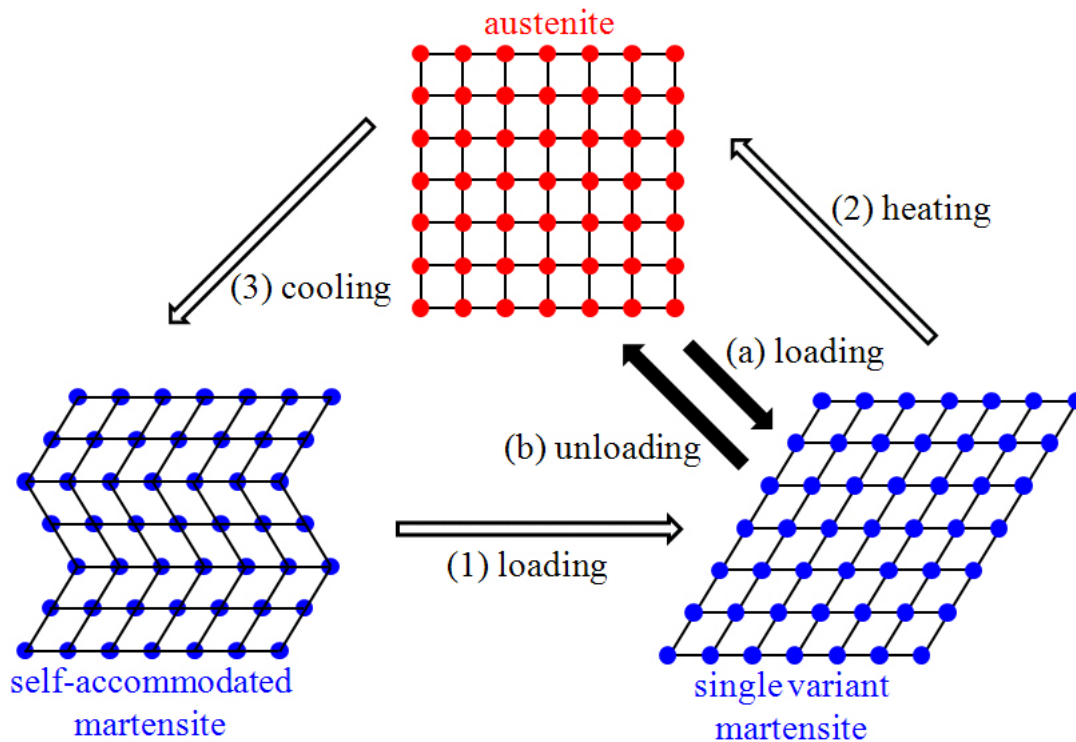


Figure 1.3: Schematic of martensitic transformation in NiTi due to thermal and mechanical loading. *Shape memory effect* is indicated by open arrows: (1) loading from self-accommodated martensite to a single variant martensite, (2) heating above the austenite finish temperature  $A_f$  to transform entirely to austenite, and (3) cooling from austenite to below the martensite finish temperature  $M_f$  returns material to original shape. The solid arrows indicate the path taken for *pseudoelasticity*: (a) the material is mechanically loaded in the austenite phase, inducing a strained aggregate which transforms to a single variant of martensite and (b) upon unloading, the material returns to the austenite phase, as the martensite phase is unstable at temperatures above the austenite finish temperature. Figure drawn from Reference [36].

in the parent austenite phase. Upon cooling, the material returns to the undeformed, multi-variant martensite. In this sense, the material has *remembered* its original state, hence the name *shape memory effect*.

These behaviors (and phases) are of great interest to industrial and biomedical applications, especially those where components on the microscale are needed [32–35]. Scientifically, the unique transformation behavior is rather complex and remains a prevalent research focus in materials science. The effect of thermal cycling on the material and the interplay of stress and transformation temperatures are yet to be fully understood, e.g. see References [42–45]. The influence thermal cycling on the stress during the reverse martensitic transformation is the focus of the investigation discussed in Chapter 4.

### 1.4.3 Diffraction studies of equiatomic NiTi

Due to the dramatic structural transition associated with the phase transformation, the material lends itself very well to investigation via XRD. Diffraction-line analysis of phase content and stress during *in situ* experiments is a powerful tool, especially to the extent

where Rietveld analysis techniques can be utilized. Examples of diffraction patterns for austenite (cubic) and martensite (monoclinic) are shown for a thin film specimen measured in Figure 1.4.

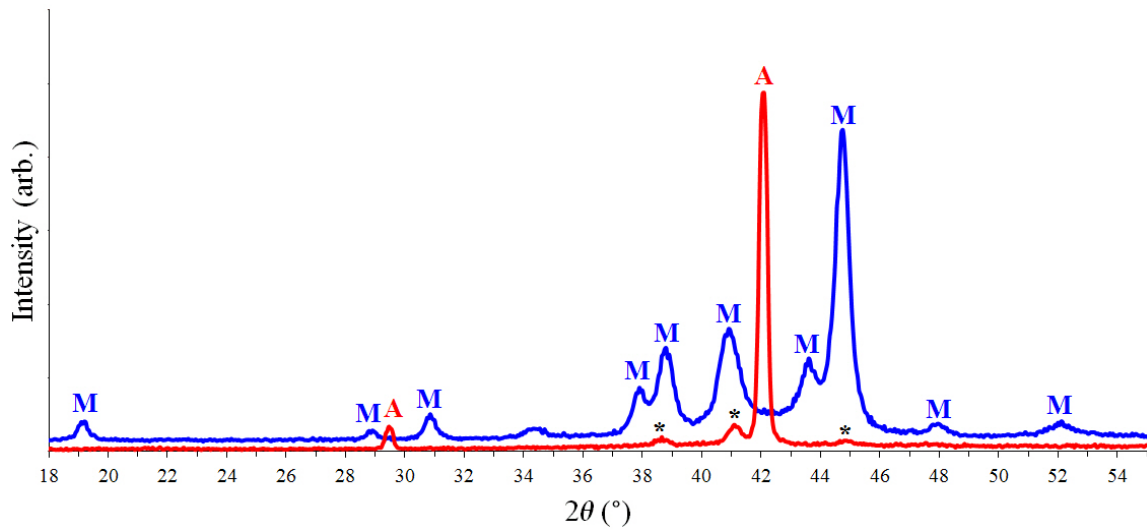


Figure 1.4: Diffraction patterns taken using synchrotron radiation ( $\lambda = 1.5307 \text{ \AA}$ ) of a NiTi thin film specimen containing  $\text{Ti}_2\text{Ni}$  precipitates (cubic phase) in the austenite state (shown in red;  $120^\circ\text{C}$ ) and the martensite state (shown in blue;  $20^\circ\text{C}$ ). The martensite and austenite reflections are indicated with the letters M and A. The additional reflections from the  $\text{Ti}_2\text{Ni}$  precipitates are only visible when the material is in the austenite phase. These are indicated with stars (\*).

## 1.5 Focus of thesis

The general theme of this thesis is the investigation of the influence of stress on materials during *in situ* experiments (such as mechanical loading or thermal cycling) using X-ray diffraction techniques. Various methods have been applied for obtaining stress and strain information:  $\sin^2 \psi$ -method, curvature measurements via  $\omega$ -rocking curves, and loading-induced peak broadening to extract essential knowledge about the strain distribution. These established measurement methods have been applied in such a manner as to deduce information about stress and strain during mechanical, thermal, and structural changes in the material. Both substrate-bound thin films and bulk material have been investigated. The majority of reported data has been collected using synchrotron radiation for XRD experiments.

## 1.6 Methodology

This section provides information about the main calculation and analysis techniques used in the research discussed in this thesis.

### 1.6.1 Thin film preparation

All of the films presented in this work were grown by sputter deposition from single-element targets. Prior to sputtering, the deposition chamber was evacuated and a bake-out process was performed to clear the chamber of any impurities. The single-crystal substrates were rotated during the deposition, which occurred in a high purity argon atmosphere.

Argon ions were directed at the target(s), which resulted in the ejection of target atoms. As these atoms reached the stage, they started to cover the substrate surface, eventually forming a closed layer. The rate of film growth is dependent on the power applied to the target(s) and the argon pressure in the chamber. When co-sputtering (using two targets of different materials), the ratio between the power applied to the targets is indicative of the composition in the deposited film. Depending on the substrate material and the desired film properties, the substrate can be heated during deposition. All of the discussed parameters can be tuned to affect the microstructure and residual stress of the deposited film.

### 1.6.2 Computational application of grain-interaction models

In order to calculate the variation in lattice spacing, a model is selected, and the loading conditions are applied to the aggregate. The stress-strain state of the single grain is solved based on its orientation (elastic constants) and boundary conditions. This calculation method, when applied to each grain in the aggregate, provides information which can be used directly to predict the (average) lattice strain in each grain as a function of grain orientation. From this, both the average strain and the strain distribution can be calculated. Broadening of diffraction peaks depends on the strain variation in a body.

The strain variation about the diffraction vector is heavily dependent on selected grain-interaction model, as shown in Figure 1.5 for a fixed diffraction geometry (and loading conditions). Due to the *isostrain* condition for the Voigt model (shown in black), a solution results where all grains experience the same strain; this means that the strain will be homogeneous throughout the entire body, resulting in a peak shift but no peak broadening. For other grain-interaction models, the strain calculated in each grain is dependent on its orientation with respect to the aggregate, and the strain variation through the aggregate can be used to predict diffraction-line broadening (and shift).

The strain variation in quasi-isotropic materials is dependent on the orientation of the grains considered and is defined as  $\epsilon_{\phi,\psi}^{\text{HKL}}(\chi)$ . (This parameter is fully defined in Chapter 2.) The angle  $\chi$  defines the orientation of a grain with respect to the diffraction vector, as shown in Figure 1.1. The grain-interaction models are applied to calculate the strain for all possible orientations. Next, the diffraction geometry (HKL or  $2\theta$  and specimen orientation,  $\phi$  and  $\psi$ ) need to be defined. Using this information, the set of grains sharing a fixed diffraction vector orientation are compiled to compose  $\epsilon_{\phi,\psi}^{\text{HKL}}(\chi)$ . It is the magnitude of variation in the function  $\epsilon_{\phi,\psi}^{\text{HKL}}(\chi)$  that determines the degree of



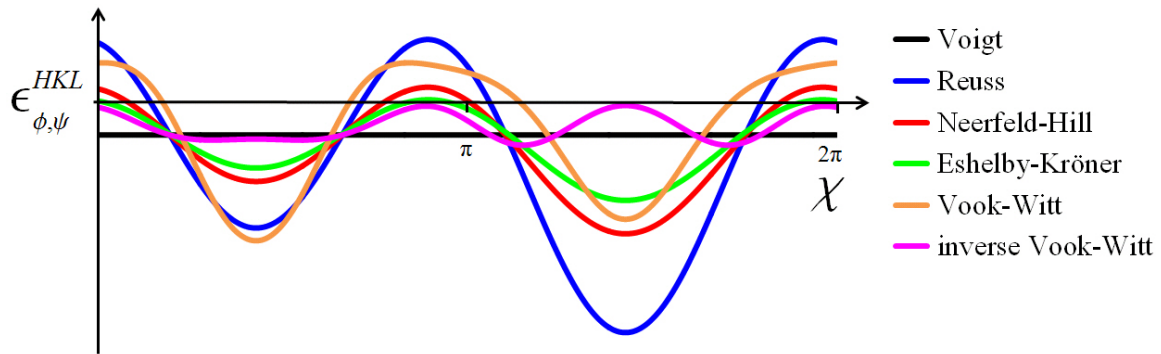


Figure 1.5:  $\epsilon_{\phi,\psi}^{\text{HKL}}$  as a function of  $\chi$  for the 331 reflection with the orientation of the diffraction vector given by  $\phi = 0^\circ$  and  $\psi = 25^\circ$  for an untextured specimen according to all of the isotropic and anisotropic elastic grain-interaction models discussed in Section 1.3.1 and Table 2.1

broadening. The average, i.e.  $\epsilon_{\phi,\psi}^{\text{HKL}}$ , provides information about the diffraction-line shift. Further details on these calculations can be found in Chapter 2.

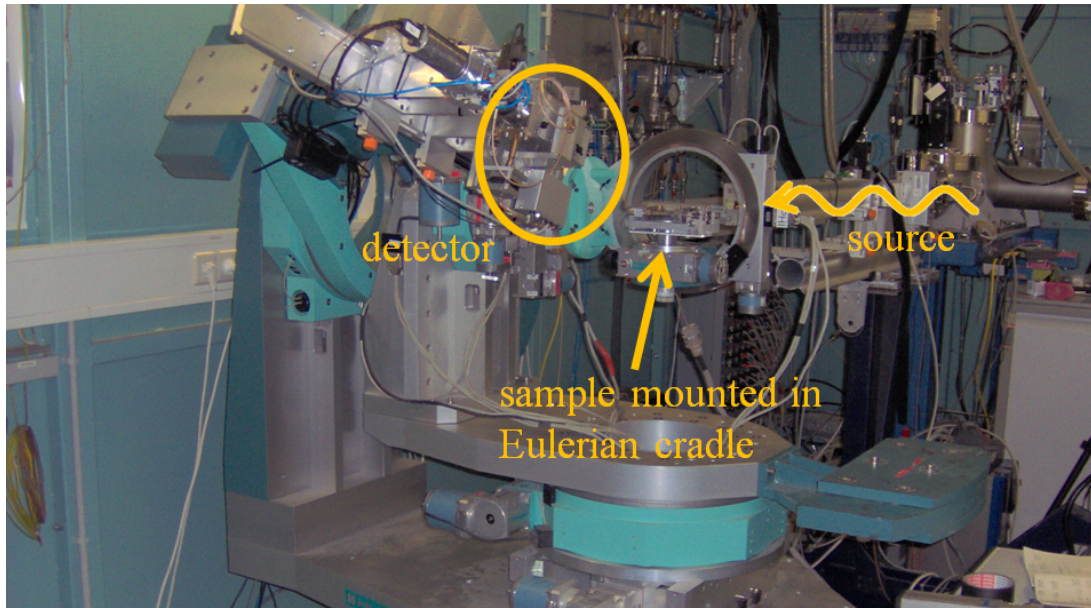
The calculated elastic strain variation about the diffraction vector  $\epsilon_{\phi,\psi}^{\text{HKL}}(\chi)$  is used to predict the broadened x-ray line broadening by convoluting the strain variation contribution with the diffraction line of an unstrained specimen.

### 1.6.3 XRD experiments

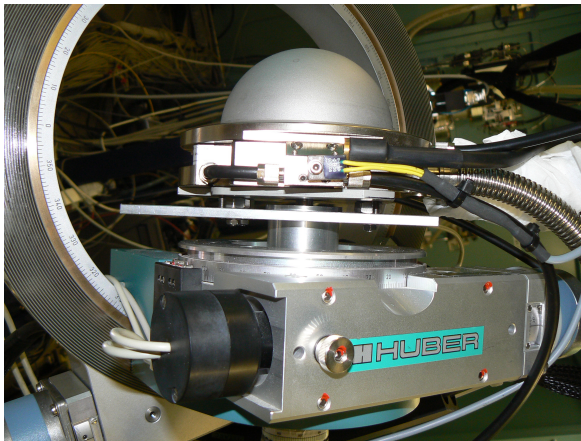
All diffraction patterns, unless otherwise mentioned (e.g. rocking curves), were measured in reflection according to the Bragg-Brentano geometry, where  $\theta$ - $2\theta$  scans were made. The presented data were all measured at the MPI surface diffraction beam line at the ANKA light source (KIT, Karlsruhe, Germany) using a NaI point detector. The experimental set-up at the beamline is shown in Figure 1.6(a). The diffraction experiments discussed in this thesis were performed using energies between 8 and 10 keV. The measurement wavelength for each experiment was calculated by performing calibration scans on an  $\text{LaB}_6$  (NIST Standard Reference Material SRM-660) powder specimen.

Individual HKL diffraction lines were always fitted with a Pearson VII shape function, with an exception for the NiTi thin film measurements discussed in Chapter 4. Rietveld analysis was performed on this data, which will be discussed in the next section. Fitting parameters for the single diffraction lines include integral area, full width at half maximum (FWHM), and asymmetry. The peak position was always taken to be the position of the greatest intensity for the calculated fit.

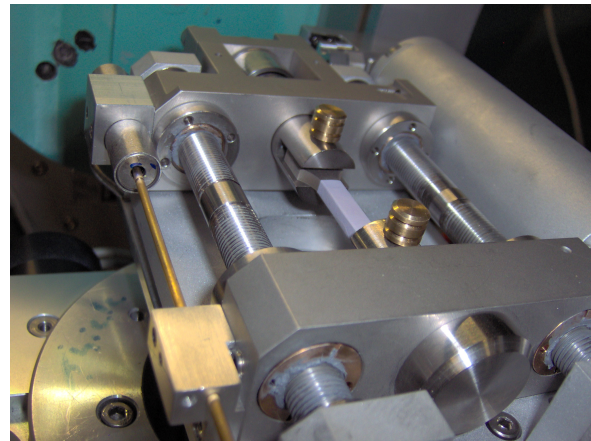
Numerous *in situ* experiments were performed at the MPI beamline, including both thermal and mechanical loading specimens. The *in situ* heating and cooling was imposed using a chamber (Figure 1.6(b); MRI Physikalische Geräte GmbH, Karlsruhe, Germany) equipped with a Be-dome, transparent to x-rays, and mounted on a six-circle Eulerian cradle. The specimens were fixed with metal clamps on the surface of the heating stage. During heating and cooling, a vacuum of approximately  $10^{-3}$  Pa was maintained in the chamber. The temperature was controlled with an accuracy of  $\pm 1^\circ\text{C}$ . The mechanical



(a) MPI surface diffraction beamline located at ANKA light source (Karlsruhe Institute of Technology), Karlsruhe, Germany



(b) Heating and cooling chamber (MRI Physikalische Geräte GmbH, Karlsruhe, Germany)



(c) Tensile machine (Kammrath & Weiss GmbH, Dortmund, Germany)

Figure 1.6: Experimental set-up for synchrotron diffraction measurements

loading was achieved through the use of a tensile machine (Kammrath & Weiss GmbH, Dortmund, Germany) mounted on an Eulerian cradle. So-called “dog-bone” specimens were uniaxially loaded during diffraction measurements.

#### 1.6.4 Rietveld analysis

One method for extracting a wealth of (micro)structural information from the entire diffraction pattern is Rietveld analysis [46]. This technique refines the parameters of a known crystal structure (or multiple crystal structures in the case for a mixed phase material) and/or of the microstructure of a polycrystalline specimen to provide the best fit with data.

Diffraction peaks are not fitted individually. Instead, the diffraction pattern is calculated using various realistic (and user-definable) parameters. Contributions such as instrument broadening and effects of the optics on the measurement are included in this calculation [46]. Numerous models for considering the intrinsic broadening parameters can be integrated in the computation scheme. Depending on the quantity and quality of the diffraction data, several parameters describing both the specimen and diffraction experiment (often termed *global* parameters) can be refined in parallel [46]. The Rietveld method allows for pattern decomposition. The willingness of H. Rietveld to share his code with others helped establish *Rietveld refinement* as one of the most commonly applied methods for profile analysis used today. Even time of flight (TOF) and energy-dispersive data can be processed using this method.

The best fit between measurement and calculation is that which has the lowest point-by-point difference, defined as

$$S_y = \sum_i \frac{1}{y_i} (y_i - y_i^c)^2 \quad (1.11)$$

where  $i$  is the number of data points,  $y_i$  is the set of measured intensities, and  $y_i^c$  is the calculated function. The solution  $y^c$  is solved in an iterative manner by a least-squares refinement. As the least-squares function is nonlinear, the initial input for parameters must be relatively close to the actual solutions. If this is not the case, the iteration may converge to a false local minimum or diverge. Most importantly, the routine attempts to improve each parameter (e.g. phase content, texture, and grain size) independently.

The Rietveld analysis performed in this work was done using a software package developed at Los Alamos National Laboratory (LANL) called General Structure Analysis System or GSAS [47, 48]. An example of a refinement using this software can be seen in Figure 1.7, where the typical final crystallographic residuals  $R_{wp}$  were between 6 and 15% for all XRD patterns refined. (See Chapter 4 for further discussion about Rietveld refinement procedures.)

## 1.7 Outline of Thesis

This thesis is divided into two sections. The first section (Chapters 2 and 3) focuses on the behavior of intrinsically elastically anisotropic grains in polycrystalline specimens under elastic loading. The second section provides an account of the investigation of the thermally-induced reverse martensitic phase transformation in equiatomic NiTi shape memory thin films and related stress development.

X-ray diffraction (XRD) has been used to observe changes in lattice spacing  $\Delta d$  due to either macroscopically applied external or internal residual stresses in bulk materials. These variations in spacing correspond to shifts in measured  $2\theta$  diffraction peak positions, as described by Bragg's law. The diffraction lines are also seen to broaden when stresses are applied to a material due to inhomogeneous stress and broadening in the aggregate.

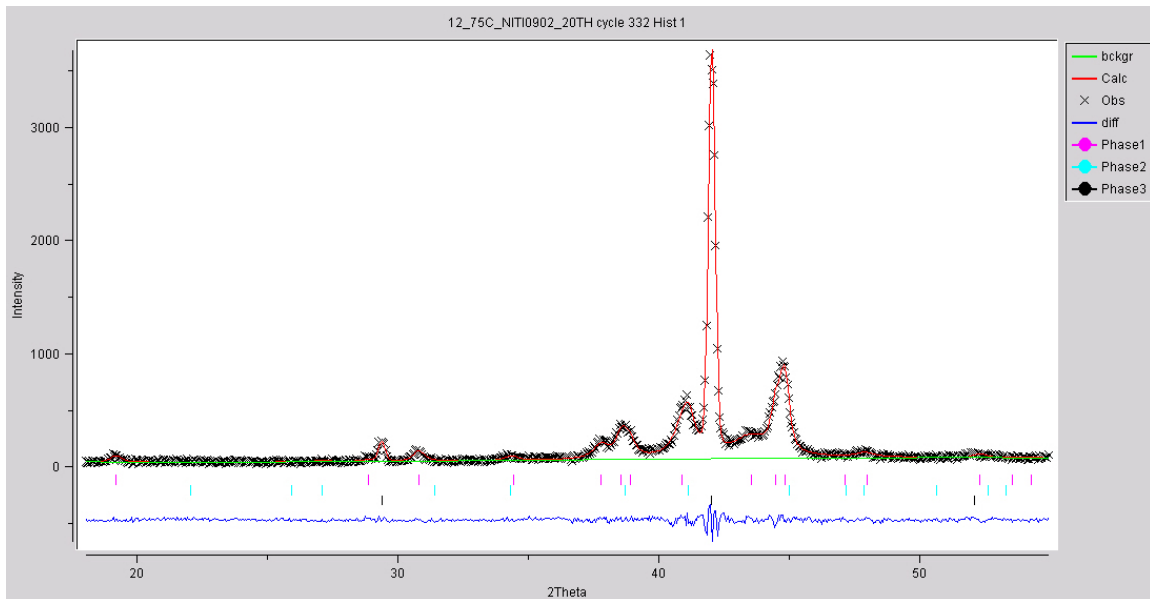


Figure 1.7: Typical pattern from Rietveld analysis using the GSAS software package; for NiTi09-02 thin film specimen, 20th heating cycle,  $T = 75^\circ\text{C}$ ,  $R_{wp} = 9.8\%$  (more details about thin film measurements and analysis method give in Chapter 4).

This is caused by the dependence of a grain's elastic behavior on its orientation, resulting in elastic grain interactions which scale with the elastic anisotropy of the material.

Elastic grain-interaction models have been used to varying degree of accuracy to describe the average elastic properties and stress-strain behavior in massive, polycrystalline materials. By applying such grain-interaction models, as demonstrated in Chapter 2, it is also possible to describe the variation in stress and strain within the aggregate. The distribution in (average) lattice strain provides contributes to the diffraction-line broadening of an elastically loaded specimen. However, a portion of broadening is also caused by local variations in the lattice strain (such as within a single grain). These additional types of strain variation (not accounted for by the elastic grain-interaction models) have been calculated through the used of finite element analysis. By considering the contributions from both the average lattice-strain variation and the local variation in lattice strain, the diffraction-line broadening due to elastic grain-interactions is discussed.

Both isotropic and anisotropic materials have been studied experimentally to measure the diffraction-line broadening induced by elastic loading. As discussed in Chapter 3, a major pitfall of the above elastic grain-interaction models is that the local heterogeneity of an quasi-isotropic aggregate is not considered. The absence of local variations in strain means that the predicted diffraction-line broadening from the discussed grain-interactions models only provides a lower bound to the experimentally observed diffraction-line broadening.

In Chapter 4, the overall effect of thermal cycling on NiTi substrate-bound films has also been investigated. The function of phase content as it depends on temperature throughout the transformation has been characterized. The change in magnitude of stress

---

at room temperature, as well as the shift in transformation temperatures, has been observed. Parameters for macroscopic stress, stress of individual phases, grain size, and texture have been studied as a function of the transformed fraction using diffraction techniques.

# Bibliography

- [1] V. Hauk, *Structural and Residual Stress Analysis by Nondestructive Methods*. Elsevier, 1997.
- [2] U. Welzel, J. Ligot, P. Lamparter, A. C. Vermeulen, and E. J. Mittemeijer, “Stress analysis of polycrystalline thin films and surface regions by X-ray diffraction,” *Journal of Applied Crystallography*, vol. 38, pp. 1–29, 2005.
- [3] B. E. Warren, *X-ray Diffraction*. Dover Publications, 1969.
- [4] W. H. Bragg and W. L. Bragg, “The reflection of X-rays by crystals,” *Proceedings of the Royal Society A*, vol. 88, no. 605, pp. 428–438, 1913.
- [5] U. Welzel and E. J. Mittemeijer, “Diffraction stress analysis of macroscopically elastically anisotropic specimens: On the concepts of diffraction elastic constants and stress factors,” *Journal of Applied Physics*, vol. 93, no. 11, pp. 9001–9011, 2003.
- [6] H. Dölle, “The influence of multiaxial stress states, stress gradients and elastic anisotropy on the evaluation of (residual) stress by x-rays,” *Journal of Applied Crystallography*, vol. 12, pp. 489–501, 1979.
- [7] S. L. Smith and W. A. Wood, “A stress-strain curve for the atomic lattice of mild steel, and the physical significance of the yield point of a metal,” *Proceedings of the Royal Society A*, vol. 179, pp. 450–460, 1942.
- [8] W. A. Wood, “The behaviour of the lattice of polycrystalline iron in tension,” *Proceedings of the Royal Society A*, vol. 192, pp. 218–231, 1948.
- [9] F. W. Jones, “The measurement of particle size by X-ray diffraction,” *Proceedings of the Royal Society A*, vol. A166, pp. 16–43, 1938.
- [10] A. C. Vermeulen, R. Delhez, T. H. de Keijser, and E. J. Mittemeijer, “Changes in the densities of dislocations on distinct slip systems during stress relaxation in thin aluminum layers: the interpretation of x-ray diffraction line broadening and line shift,” *Journal of Applied Physics*, vol. 77, no. 10, pp. 5026–50497, 1995.
- [11] A. Leineweber and E. J. Mittemeijer, “Notes on the order-of-reflection dependence of microstrain broadening,” *Journal of Applied Crystallography*, vol. 43, pp. 981–989, 2010.



- [12] U. Welzel, S. Fréour, and E. J. Mittemeijer, “Direction-dependent elastic grain-interaction models - a comparative study,” *Philosophical Magazine*, vol. 85, no. 21, pp. 2391–2414, 2005.
- [13] L. B. Freund and S. Suresh, *Thin Film Materials: Stress, Defects Formation and Surface Evolution*. Cambridge University Press, 2003.
- [14] G. Stoney, “The tension of metallic films deposited by electrolysis,” *Proceedings of the Royal Society*, vol. A82, pp. 172–175, 1909.
- [15] A. Segmüller, I. C. Noyan, and V. S. Speriosu, “X-ray diffraction studies of thin films and multilayer structures,” *Progress in Crystal Growth and Characterization of Materials*, vol. 18, pp. 21–66, 1989.
- [16] W. Voigt, *Lehrbuch der Kristallphysik*. Teuber, Leipzig-Berlin, 1910.
- [17] A. Reuss, “Account of the liquid limit of mixed crystals on the basis of the plasticity condition for single crystal,” *Zeitschrift für Angewandte Mathematik und Mechanik*, vol. 9, pp. 49–58, 1929.
- [18] H. Neerfeld, “Zur Spannungsberechnung aus röntgenographischen Dehnungsmessungen,” *Mitteilung Kaiser-Wilhelm-Institut-Eisenforschung*, vol. 24, pp. 61–70, 1942.
- [19] R. Hill, “The elastic behaviour of a crystalline aggregate,” *Proceedings of the Physical Society A*, vol. 65, no. 389, pp. 349–355, 1952.
- [20] R. W. Vook and F. Witt, “Thermally induced strains in evaporated films,” *Journal of Applied Physics*, vol. 36, no. 7, pp. 2169–2171, 1965.
- [21] F. Witt and R. W. Vook, “Thermally induced strains in cubic metal films,” *Journal of Applied Physics*, vol. 39, no. 6, pp. 2773–2776, 1968.
- [22] U. Welzel, M. Leoni, and E. J. Mittemeijer, “The determination of stresses in thin films; modelling elastic grain interaction,” *Philosophical Magazine*, vol. 83, no. 5, pp. 603–630, 2003.
- [23] J. D. Eshelby, “The determination of the elastic field of an ellipsoidal inclusion, and related problems,” *Proceedings of the Royal Society A*, vol. 241, no. 1226, pp. 379–396, 1957.
- [24] E. Kröner, “Berechnung der elastischen konstanten des vielkristalls aus den konstanten des einkristalls,” *Zeitschrift für Physik*, vol. 151, no. 4, pp. 504–518, 1958.
- [25] N. Koch, U. Welzel, H. Wern, and E. J. Mittemeijer, “Mechanical elastic constants and diffraction stress factors of macroscopically elastically anisotropic polycrystals: the effect of grain-shape (morphological) texture,” *Philosophical Magazine*, vol. 84, no. 33, pp. 3547–3570, 2004.

- [26] U. F. Kocks, C. N. Tomé, and H.-R. Wenk, *Texture and Anisotropy*. New York, NY: Cambridge University Press, 4th ed., 1998.
- [27] C. M. Sayers, “The strain distribution in anisotropic polycrystalline aggregates subjected to an external stress field,” *Philosophical Magazine A*, vol. 49, no. 2, pp. 243–262, 1984.
- [28] N. Funamori, M. Funamori, R. Jeanloz, and N. Hamaya, “Broadening of X-ray powder diffraction lines under nonhydrostatic stress,” *Journal of Applied Physics*, vol. 82, no. 1, pp. 142–146, 1997.
- [29] A. K. Singh and C. Balasingh, “X-ray diffraction line broadening under elastic deformation of polycrystalline sample: An elastic-anisotropy effect,” *Journal of Applied Physics*, vol. 90, no. 5, pp. 2296–2302, 2001.
- [30] L. C. Chang and T. A. Read, “Plastic deformation and diffusionless phase changes in metals - the gold-cadmium  $\beta$ -phase,” *Transactions of the American Institute of Mining and Metallurgical Engineers*, vol. 191, no. 1, pp. 47–52, 1951.
- [31] W. J. Buehler, R. C. Wiley, and J. V. Gilfrich, “Effect of low-temperature phase changes on mechanical properties of alloys near composition TiNi,” *Journal of Applied Physics*, vol. 34, no. 5, p. 1475, 1963.
- [32] J. Van Humbeeck, “Non-medical applications of shape memory alloys,” *Materials Science & Engineering A*, vol. 273, pp. 134–148, 1999.
- [33] K. Otsuka and T. Kakeshita, “Science and technology of shape-memory alloys. New developments,” *Materials Research Society Bulletin*, vol. 2, pp. 91–100, 2002.
- [34] R. D. Christofferson, S. R. Kapadia, V. Rajagopal, and E. M. Tuzcu, “Emerging transcatheter therapies for aortic and mitral disease,” *Heart*, vol. 95, no. 2, pp. 148–155, 2009.
- [35] D. Zakharov, G. Lebedev, A. Irzhak, V. Afonina, A. Mashirov, V. Kalashnikov, V. Koledov, A. Shelyakov, D. Podgorny, and N. Tabachkova, “Submicron-sized actuators based on enhanced shape memory composite material fabricated by FIB-CVD,” *Smart Materials and Structures*, vol. 21, p. 052001, 2012.
- [36] S. Miyazaki, Y. Q. Fu, and W. M. Huang, *Thin Film Shape Memory Alloys: Fundamentals and Device Applications*. Cambridge University Press, 1st ed., 2009.
- [37] K. Otsuka and C. M. Wayman, eds., *Shape Memory Materials*. Cambridge University Press, 1999.
- [38] S. Kustov, D. Salas, R. Santamarta, E. Cesari, and J. van Humbeeck, “Isothermal and athermal martensitic transformation in the B2-R-B19' sequence in Ni-Ti shape memory alloys,” *Scripta Materialia*, vol. 63, no. 12, pp. 1240–1243, 2010.



- [39] Y. Kudoh, M. Tokonami, S. Miyazaki, and K. Otsuka, "Crystal structure of the martensite in Ti-49.2% alloy analyzed by the single crystal X-ray diffraction method," *Acta Metallurgica*, vol. 33, pp. 2049–2056, 1985.
- [40] Z. Zhaoyi, H. Cuie, C. Lingcang, C. Xiangrong, and J. Fuqian, "Lattice dynamics and phase transition of Ni Ti Alloy," *Solid State Communications*, vol. 149, pp. 2164–2168, 2009.
- [41] S. Sridharan, H. Nowotny, and S. F. Wayne, "Investigations within the quaternary system Ti-Ni-Al-C," *Monatshefte für Chemie und verwandte Teile anderer Wissenschaften*, vol. 114, pp. 127–135, 1983.
- [42] C. Urbina and S. De la Flor, "Effect of thermal cycling on the thermomechanical behaviour of NiTi shape memory alloys," *Materials Science & Engineering A*, vol. 501, pp. 197–206, 2009.
- [43] Y. Q. Fu and H. J. Du, "Effects of film composition and annealing on residual stress evolution for shape memory TiNi film," *Materials Science & Engineering A*, vol. A342, pp. 236–244, 2003.
- [44] Y. Q. Fu and H. J. Du, "Relaxation and recovery of stress during martensitic transformation for sputtered shape memory TiNi film," *Surface and Coatings Technology*, vol. 153, pp. 100–105, 2002.
- [45] A. Kumar, S. K. Sharma, S. V. Kamat, and S. Mohan, "Stress evolution with temperature in titanium-rich NiTi shape memory alloy films," *Strain*, vol. 47, no. 6, pp. 469–475, 2011.
- [46] R. A. Young, *The Rietveld Method*. Oxford University Press, 1993.
- [47] A. C. Larson and R. B. V. Dreele, "General Structure Analysis System (GSAS)," *Los Alamos National Laboratory Report LAUR*, pp. 86–748, 2005.
- [48] B. H. Toby, "EXPGUI, a graphical user interface for GSAS," *Journal of Applied Crystallography*, vol. 34, pp. 210–213, 2001.



## Chapter 2

# Elastic mechanical grain interactions in polycrystalline materials; analysis by diffraction-line broadening

M. K. A. Koker, U. Welzel, and E. J. Mittemeijer

### Abstract

Experimental investigations have revealed that the Neerfeld-Hill and Eshelby-Kröner models, for grain interactions in massive, bulk (in particular, macroscopically isotropic) polycrystals, and a recently proposed effective grain-interaction model for macroscopically anisotropic polycrystals, as thin films, provide good estimates for the macroscopic (mechanical and) x-ray elastic constants and stress factors of such polycrystalline aggregates. These models can also be used to calculate the strain variation among the diffracting crystallites, i.e. the diffraction-line broadening induced by elastic grain interactions can thus be predicted. This work provides an assessment of diffraction-line broadening induced by elastic loading of polycrystalline specimens according to the various grain-interaction models. It is shown that the variety of environment, and thus the heterogeneity of the stress-strain states experienced by each of the individual grains exhibiting the same crystallographic orientation in a real polycrystal, *cannot* be accounted for by traditional grain-interaction models, where all grains of the same crystallographic orientation in the specimen frame of reference are considered to experience the same stress-strain state. A significant degree of broadening which is induced by the heterogeneity of the environments of the individual crystallites is calculated on the basis of a finite element algorithm. The obtained results have vast implication for diffraction-line broadening analysis and modeling of the elastic behavior of massive polycrystals.

## 2.1 Introduction

In a massive polycrystalline aggregate, each of the generally anisotropic grains cannot deform freely to comply with an imposed state of mechanical stress; instead, each grain must adapt its mechanical response to its surroundings. For the case of elastic loading, various grain-interaction models have been proposed to describe the (overall) stress and strain behavior of the individual grains within an aggregate. These models can be employed for calculating mechanical and so-called diffraction (x-ray) elastic constants (in the case of macroscopic elastic isotropy) and stress factors (in the case of macroscopic elastic anisotropy) of polycrystalline specimens from single-crystal elastic data [1].

A number of grain-interaction models to describe the strain and stress of individual crystallites, recognizing their orientations within the aggregate, in a massive polycrystalline body subjected to a specific state of elastic loading have been reviewed in Reference [2]. Such models are used to calculate the effective, macroscopic elastic constants of a material, from single-crystal elastic data, employing the crystallographic orientation distribution function (ODF) to account for the occurrence of crystallographic texture [3]. Such models yield very good agreement of the thus calculated macroscopic and diffraction elastic constants/stress factors with experimentally determined values (e.g. see Reference [4]). The following discussion presents a comparison of the known grain-interaction models proposed [5–14], considering both direction-independent (here termed isotropic) and direction-dependent (here termed anisotropic) grain-interaction models and the role of crystallographic texture.

The behavior of individual grains within a massive, polycrystalline material under elastic loading is quite complicated. Grain-interaction models seek to provide a “simplified” description of the (overall) stress and strain in each grain dependent on its orientation with respect to the aggregate (and thus the elastic behavior of the body as a whole). In this work, the strain variation among the diffracting crystallites will be calculated according to six different elastic grain-interaction models (see Section 2.4) for the purpose of theoretically determining the elastic loading-induced diffraction-line broadening.

Due to elastic grain interactions, a polycrystalline aggregate under elastic loading exhibits a strain and stress distribution which varies through the body dependent especially on the grain-orientation distribution and the intrinsic, anisotropic elasticity of the individual grains. This will be the case even when the macroscopic elastic properties are isotropic (i.e. the polycrystal is “quasi-isotropic” [15]) and the imposed stress state of the body is homogeneous. A strain distribution in the aggregate induces a variation in lattice-plane spacing, which results in broadening and possibly a shift of the measured x-ray diffraction (XRD) lines [16]. The induced peak shift is well understood and can be described using Bragg’s law and by expressing strain in terms of the average lattice strain of the diffracting crystallites [1]. Here the effect of the lattice-strain variation on diffraction-line broadening is considered.

The measured diffraction line  $h$  is the convolution of the individual diffraction profiles pertaining to the instrumental line broadening  $g$  and the different specimen-related, structural sources of diffraction-line broadening  $f$ , such as grain interactions, finite crystallite size, dislocations, etc. [17, 18, and references therein]:

$$h(2\theta) = g(2\theta) \otimes f_{size}(2\theta) \otimes f_{grain\ interactions}(2\theta) \otimes f... \quad (2.1)$$

where  $2\theta$  is the diffraction angle. If the individual profiles in Equation 2.1 are known, the convoluted profile can be calculated straightforwardly. The reverse calculation (i.e. the extractions of the  $f$  profiles from the  $g$  and  $h$  profiles) is not generally straight-forward, and various methods for the separation of the different structural contributions to the overall diffraction-line shape have been developed [17].

Loading-induced broadening of diffraction peaks depends on the strain distribution (or variation of the lattice spacing) throughout the polycrystalline aggregate. Consider the measurement geometry shown in Figure 2.1. Both the average lattice spacing in the direction of the diffraction vector and the distribution of lattice spacing in this direction (caused by elastic loading) can be calculated through the use of grain-interaction models for analyzing the contribution of all grains with  $hkl$  planes perpendicular to the  $HKL$  diffraction vector. The strain variation which occurs as a function of rotation about the diffraction vector (rotation angle  $\chi$ ; Figure 2.1) can be used to predict the diffraction-line broadening by convoluting the calculated strain distribution function with the diffraction peak recorded for the same diffraction vector from the unloaded polycrystalline aggregate.

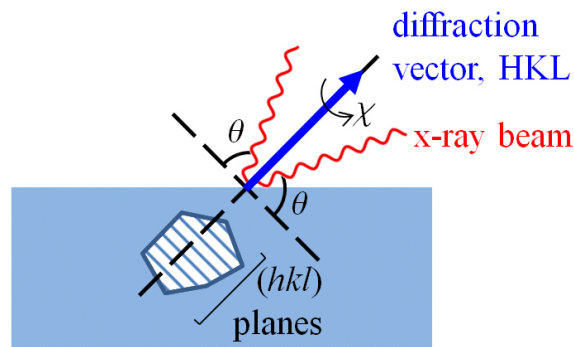


Figure 2.1: Schematic to demonstrate the degree of grain rotational freedom, in a diffraction experiment, given as the angle  $\chi$ , defining the rotation about the  $HKL$  diffraction vector, which is perpendicular to a set of  $(hkl)$  planes.

The overall extent of the variation in lattice strain as a function of the angle of rotation about the diffraction vector  $\chi$  is not dependent on the overall compliance of the material, but, instead, on the degree of elastic anisotropy of the material [19], which can be given as a ratio of intrinsic elastic constants. For cubic materials, the elastic anisotropy parameter

$\mathcal{A}$  (also known as the Zener's anisotropy ratio) is defined as [20]:

$$\mathcal{A} = \frac{2(s_{11} - s_{12})}{s_{44}} = \frac{2 \cdot c_{44}}{c_{11} - c_{12}}, \quad (2.2)$$

where  $s_{ij}$  and  $c_{ij}$  are the single-crystal elastic constants for compliance and stiffness, respectively. If the elastic response of an isolated grain for a specific material is independent of its orientation with respect to the (anisotropic) state of loading, which holds for tungsten, the material is called intrinsically elastically isotropic ( $\mathcal{A} = 1$ ). For such materials, all grains experiencing the same imposed stress state will exhibit identical (average) lattice strains, independent of grain orientation, i.e. the (average) lattice strain will not depend on the angle  $\chi$ .

Diffraction-line broadening has been studied extensively in order to understand and separate contributions due to factors such as finite crystallite/domain size and microstrain [17]. Few studies have focused on the lattice-strain variation induced broadening as a result of isotropic and anisotropic elastic grain interactions. Preliminary work consists of theoretical lattice-strain distribution calculations made according to classical, isotropic grain-interaction models (see Section 2.2) for polycrystalline cubic material under uniaxial elastic loading [16].

Simulated lattice-strain distributions using the Reuss model demonstrated that line broadening is only induced by deviatoric components of the applied mechanical stress [21], which means that, for this case, hydrostatic stress (often termed pressure) does not influence the measurable diffraction-line broadening. A simplified analytical expression was derived for the variance of strain in elastically loaded specimens, using the Voigt and Reuss models as lower and upper bounds [22]. For a given HKL reflection and a fixed diffraction geometry, the strain variance was found to scale with the square of the magnitude of the applied load  $\sigma^2$  and with the elastic anisotropy parameter  $\mathcal{A}$ . An empirical scaling factor was introduced into the expression in order to provide agreement with the experimental data.

The work presented here provides a comprehensive and in depth investigation into lattice-strain variation and the resulting diffraction-line broadening induced by elastic loading. Several grain-interaction models and finite element calculation of strain distributions are employed. The observed trends, i.e. those found in previous works and those exposed for the first time, will be discussed providing fundamental understanding of diffraction-line broadening induced by elastic loading. The effects of both crystallographic and morphological textures are considered as well [4, 11].

## 2.2 Grain-interaction models

Elastic grain-interaction models provide a framework for the calculation of stress and strain as a function of crystallographic orientation of a crystal within a macroscopically

elastically loaded specimen. Such models can be applied to calculate the (average) lattice strain or the macroscopic elastic constants and the diffraction elastic constants (or stress factors) of a material. Either isotropic grain interaction (in all directions within the body, the grain interaction is treated identically) or anisotropic grain interaction (e.g. due to the presence of surface and/or as caused by non-equiaxed grain shape) are adopted in such models.

The Voigt [5] and Reuss [6] grain-interaction models are the classical, extreme approaches for describing the isotropic elastic behavior of grains within a polycrystal under applied elastic loading. Neither of the models portrays a realistic picture of the stress-strain variation within actual polycrystalline aggregates, since both imply discontinuities of either the stress (Voigt) or the strain (Reuss) at the grain boundaries. These models are often used to assess the (supposedly; see [14]) lower and upper bounds of macroscopic elastic behavior of a polycrystalline material. The Voigt and Reuss models are often applied because their solutions can be found analytically. To approach reality, effective grain-interaction models, such as the Neerfeld-Hill [7,8] model, use a linear combination of the solutions from the extreme Voigt and Reuss models, and thus yield results for the average lattice strain and macroscopic elastic constants which compare well with experimental measurements. Grain shape is not explicitly considered in the isotropic grain-interaction models, but as all directions are taken as equivalent for the grain interaction in the specimen frame of reference, the isotropic models are incompatible with the occurrence of a grain-shape texture [11].

In the Eshelby-Kröner [9,10] model, instead of making an assumption about the state of stress or strain in the individual crystallites (as with the Voigt and Reuss models), continuity in stress and strain at the interface of a grain and the aggregate is enforced: all grains of identical crystallographic orientation in the specimen are taken together as a single inclusion in a homogeneous aggregate, which thus functions as an effective medium, meaning that each of its properties is an average over all grains in the specimen. The stress and strain which satisfy continuity at the interface between the grain and this effective medium are then calculated in a computationally intensive way. Additionally, the Eshelby-Kröner [9–11] model allows for the incorporation of grain shape through a parameter  $\eta$ , the grain-aspect ratio, where  $\eta = 1$  represents spherical grains.

Models for anisotropic grain interaction, e.g. due to surface anisotropy, are the Vook-Witt model [12,13], in particular, see Reference [23], and the inverse Vook-Witt model [14], which imply different grain-interaction assumptions for directions parallel and perpendicular to the specimen surface.

An overview of these isotropic and anisotropic elastic grain-interaction models, all of which will be applied in this paper for the analysis of the corresponding diffraction-line broadening, is provided by Table 2.1.

Table 2.1: Grain-interaction models, where  $\mathbf{c}$  is the single-crystal elasticity tensor for stiffness,  $\mathbf{C}$  is the macroscopic elastic stiffness tensor, and  $\mathbf{S}$  is the macroscopic elastic compliance tensor for the polycrystal. (Color corresponds to models used for the calculations shown in Figures 2.5-2.16.) Models can be classified into two separate categories: *isotropic* (equality of grain interactions in all directions) and *anisotropic* (direction dependent grain interactions).

	Model	Basics	
Isotropic models	Voigt [5]	Crystallites tightly connected, deforming together; all grains under identical state of strain	$\boldsymbol{\epsilon} = \langle \boldsymbol{\epsilon} \rangle,$ $\boldsymbol{\sigma} = \mathbf{c} \langle \boldsymbol{\epsilon} \rangle = \mathbf{c} \mathbf{S} \langle \boldsymbol{\sigma} \rangle$
	Reuss [6]	Crystallites deform freely; all grain under identical state of stress	$\boldsymbol{\sigma} = \langle \boldsymbol{\sigma} \rangle$
	Neerfeld-Hill [7, 8]	Strain and stress distributions, as well as elastic constants, taken as the arithmetic averages of the Voigt ( $V$ ) and Reuss ( $R$ ) bounds	$\mathbf{C} = \frac{1}{2} \{ \mathbf{C}_V + \mathbf{C}_R \}$
(Shape dependent)	Eshelby-Kröner [9–11]	Continuity of stress and strain at interface between inclusion and homogeneous aggregate; inclusion: all grains of identical orientations and/or shape (shape factor, $\eta$ ); aggregate: effective medium	$\eta = 1$ : spherical $\eta \rightarrow \infty$ : needle-like $\eta \rightarrow 0$ : disc-shaped
Anisotropic models	Vook-Witt [12, 13]	All grains under same stress perpendicular to the surface, experiencing identical strains parallel to the surface	$\epsilon_{ij} = \langle \epsilon_{ij} \rangle, \quad i, j \neq 3$ $\sigma_{ij} = \langle \sigma_{ij} \rangle, \quad i, j = 3$
	Inverse Vook-Witt [14]	All grains under same stresses parallel to the surface, and experiencing identical strain perpendicular to the surface	$\epsilon_{ij} = \langle \epsilon_{ij} \rangle, \quad i, j = 3$ $\sigma_{ij} = \langle \sigma_{ij} \rangle, \quad i, j \neq 3$



## 2.3 Calculation of diffraction-line broadening induced by external loading

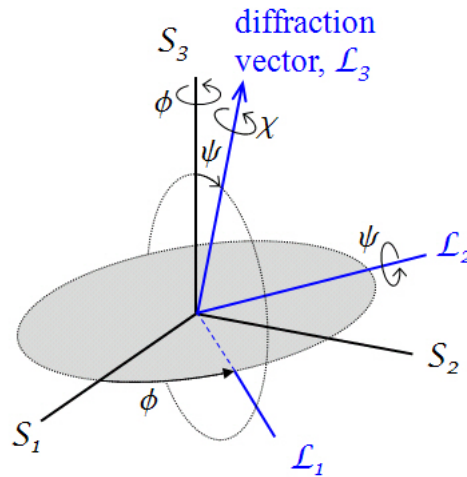
### 2.3.1 Procedure

It is convenient to introduce the following three Cartesian frames of reference as shown in Figure 4.2(b):

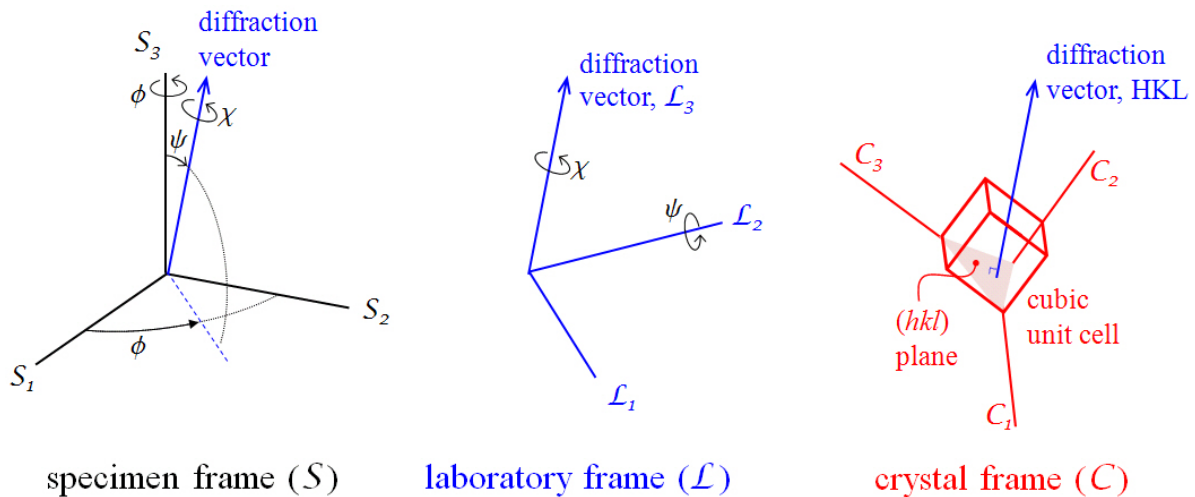
- The *crystal frame of reference* ( $\mathcal{C}$ ): The conventional definition of an orthonormal crystal system, such as the one given in [20] (for a detailed treatment, see also [24]), is adopted. For cubic crystal symmetry, the axes coincide with the  $a$ ,  $b$ , and  $c$  axes of the crystal lattice, with the  $\mathcal{C}_1$  axis along the 100 direction, the  $\mathcal{C}_2$  axis along the 010 direction, and the  $\mathcal{C}_3$  axis along the 001 direction.
- The *specimen frame of reference* ( $\mathcal{S}$ ): The  $\mathcal{S}_3$  axis is orientated perpendicular to the specimen surface, and the  $\mathcal{S}_1$  and  $\mathcal{S}_2$  axes are in the surface plane.
- The *laboratory frame of reference* ( $\mathcal{L}$ ): This frame is chosen in such a way that the  $\mathcal{L}_3$  axis coincides with the diffraction vector in the (x-ray) diffraction experiment.

The relative orientation of the laboratory frame of reference with respect to the specimen frame of reference is specified by the angles  $\phi$  and  $\psi$ , where  $\psi$  is the inclination angle of the sample surface normal (i.e. the  $\mathcal{S}_3$  axis) with respect to the diffraction vector (i.e. the  $\mathcal{L}_3$  axis) and  $\phi$  denotes the rotation of the sample around the sample surface normal (Figure 4.2(a)). The angle  $\chi$  is defined as a rotation of the laboratory frame about the  $\mathcal{L}_3$  axis, where, for  $\phi = \psi = \chi = 0^\circ$ , the  $\mathcal{L}$  frame of reference coincides with the  $\mathcal{S}$  frame of reference. The direction of the diffraction vector is especially important as this is the direction along which lattice strain is measured in XRD experiments. In the following, a superscript ( $\mathcal{C}$ ,  $\mathcal{S}$ , or  $\mathcal{L}$ ) is used for indicating the reference frame adopted for the representation of a tensor.

The orientation of each crystallite in the  $\mathcal{S}$  system can be identified by three Euler angles:  $\alpha$ ,  $\beta$ , and  $\gamma$  [25]. These angles represent consecutive rotations of the  $\mathcal{C}$  frame, with respect to the  $\mathcal{S}$  frame. The  $\mathcal{C}$  frame is first rotated by  $\alpha$  about  $\mathcal{C}_3$ , then by  $\beta$  about  $\mathcal{C}_1$ , and finally by  $\gamma$  about  $\mathcal{C}_2$  (following the Bunge convention; see [26, 27] and Figure 2.20). It is usual to associate a set of Euler angles with a vector  $\mathbf{g} = (\alpha, \beta, \gamma)$  in the three-dimensional orientation (Euler) space  $G$  [28]. In this way, each point in the orientation space  $G$  represents a possible orientation of the  $\mathcal{C}$  frame of reference with respect to the  $\mathcal{S}$  frame of reference. Only in the absence of texture does it hold that the volume fraction of crystallites, which have an orientation in the infinitesimal orientation range  $d^3\mathbf{g} = \sin(\beta)d\alpha d\beta d\gamma$  around  $\mathbf{g}$ , is independent of  $\mathbf{g}$ . Texture can be quantified by introducing the ODF,  $\mathcal{F}(\alpha, \beta, \gamma)$ , which is a function of the Euler angles, specifying the volume fraction of crystallites having an orientation in the infinitesimal orientation range



(a) Laboratory frame ( $\mathcal{L}$ ) defined with respect to the specimen frame ( $\mathcal{S}$ ) by the diffraction angles  $\phi$ ,  $\psi$ , and  $\chi$



(b) Orientation of reference frames defined by the orientation of the diffraction vector (for a fixed HKL,  $\phi$ ,  $\psi$ , and  $\chi$ )

Figure 2.2: Introduction of the three standard coordinate systems and the corresponding orientation angles necessary for the discussion of diffraction experiments.

$d^3\mathbf{g} = \sin(\beta)d\alpha d\beta d\gamma$  around  $\mathbf{g}$ :

$$\frac{dV(\mathbf{g})}{V} = \frac{\mathcal{F}(\mathbf{g})}{8\pi^2} d^3\mathbf{g} = \frac{\mathcal{F}(\alpha, \beta, \gamma)}{8\pi^2} \sin(\beta)d\alpha d\beta d\gamma \quad (2.3)$$

The ODF is normalized:  $\int \int \int_G \frac{\mathcal{F}(\mathbf{g})}{8\pi^2} d^3\mathbf{g} = 1$ .

In the following, angular brackets  $\langle \dots \rangle$  denote volume-weighted averages for all crystallites in the volume considered (i.e. mechanical averages) where as braces  $\{ \dots \}$  denote volume-weighted averages for diffracting crystallites only (i.e. diffraction averages). In

the context of diffraction analysis, the analyzed volume is generally only a fraction of the volume of the polycrystalline specimen.

Mechanical averages of a tensor  $\Omega$  can be calculated by integration over all Euler angles, using the ODF  $\mathcal{F}(\mathbf{g})$  as a weighting factor:

$$\begin{aligned}\langle \Omega \rangle &= \frac{1}{8\pi^2} \int \int \int_G \mathcal{F}(\mathbf{g}) d^3\mathbf{g} \\ &= \frac{1}{8\pi^2} \int_{\gamma=0}^{2\pi} \int_{\beta=0}^{2\pi} \int_{\alpha=0}^{2\pi} \Omega(\alpha, \beta, \gamma) \mathcal{F}(\alpha, \beta, \gamma) \sin(\beta) d\alpha d\beta d\gamma\end{aligned}\quad (2.4)$$

A diffraction line contains data pertaining to only the subset of crystallites for which the diffraction planes are perpendicular to the chosen measurement direction. Since only the measurement direction (i.e. the direction of the diffraction vector) is defined, a degree of freedom occurs for the diffracting crystallites: the rotation about the diffraction vector (denoted by the angle  $\chi$  in the following). For a HKL diffraction line, the group of diffracting crystallites is selected by specifying the HKL of the reflection and the orientation of the diffraction vector with respect to the specimen reference frame  $\mathcal{S}$ , which can be identified by the angles  $\phi$  and  $\psi$ . Therefore the sub- ( $\phi, \psi$ ) and superscripts (HKL) are attached to the corresponding average:

$$\{\Omega\}_{\phi, \psi}^{\text{HKL}} = \frac{\int_0^{2\pi} \Omega(\text{HKL}, \chi, \phi, \psi) \mathcal{F}^*(\text{HKL}, \chi, \phi, \psi) d\chi}{\int_0^{2\pi} \mathcal{F}^*(\text{HKL}, \chi, \phi, \psi) d\chi}.\quad (2.5)$$

$\mathcal{F}^*(\text{HKL}, \chi, \phi, \psi) d\chi$  is the representation of the ODF in terms of the measurement parameters and the rotation angle  $\chi$ . The ODF as defined in Equation 2.3 cannot be directly used in Equation 2.5, in analogy to Equation 2.4, since the angles  $\chi$ ,  $\phi$ , and  $\psi$  are *not* Euler angles representing a rotation of the  $\mathcal{C}$  system with respect to the  $\mathcal{S}$  system. (They provide the rotation of the system  $\mathcal{L}$  with respect to the system  $\mathcal{S}$ .) However, the values of  $\alpha$ ,  $\beta$ , and  $\gamma$ , and thus the  $\mathcal{F}(\alpha, \beta, \gamma)$  and thereby  $\mathcal{F}^*(\text{HKL}, \chi, \phi, \psi)$  at every  $\chi$ , can be calculated from HKL,  $\chi$ ,  $\phi$ , and  $\psi$ . (For a more detailed treatment, see [14].)

Using the above approach, for a fixed diffraction vector (i.e. HKL,  $\phi$ , and  $\psi$  have been specified), the average lattice strain  $\epsilon_{\phi, \psi}^{\text{HKL}}$  and the lattice-strain distribution by rotation about the diffraction vector  $\epsilon_{33}^{\mathcal{L}}(\text{HKL}, \phi, \psi, \chi)$  are related according to:

$$\epsilon_{\phi, \psi}^{\text{HKL}} = \{\epsilon_{33}^{\mathcal{L}}\}_{\phi, \psi}^{\text{HKL}} = \frac{\int_0^{2\pi} \epsilon_{33}^{\mathcal{L}}(\text{HKL}, \chi, \phi, \psi) \mathcal{F}^*(\text{HKL}, \chi, \phi, \psi) d\chi}{\int_0^{2\pi} \mathcal{F}^*(\text{HKL}, \chi, \phi, \psi) d\chi}.\quad (2.6)$$

In order to compute the strain-broadened diffraction line, both the average lattice strain  $\epsilon_{\phi, \psi}^{\text{HKL}}$  (directly related to peak position upon loading) and the strain distribution  $\epsilon_{\phi, \psi}^{\text{HKL}}(\chi)$  ( $\epsilon_{33}^{\mathcal{L}}(\chi)$  at fixed HKL,  $\phi$ , and  $\psi$ ) are required.

The strain distribution  $\epsilon_{\phi, \psi}^{\text{HKL}}(\chi)$  can be converted into a frequency function  $f(\epsilon)$  which describes the fraction of grains in the considered diffraction volume sharing the same diffraction vector and which experience the same (average) strain. Using Bragg's law

(for a specified radiation wavelength and the material's strain-free lattice parameter  $d_o$  corresponding to  $\epsilon = 0$ ), the frequency function  $f(\epsilon)$  can be converted to the  $2\theta$  scale. This transformation results in the *strain-induced broadening contribution function*  $f(2\theta)$ . The function  $f(2\theta)$ , when convoluted with the diffraction profile corresponding to the diffraction line contribution for the unloaded state  $g(2\theta)$ , yields the “measured” diffraction peak  $h(2\theta)$  (see Equation 2.1). It is important to note that here  $g(2\theta)$  incorporates all broadening contributions (such as grain size and instrumental broadening) other than that induced by the external mechanical loading. Upon unloading, the diffraction line  $h(2\theta)$  relaxes to  $g(2\theta)$ , as all broadening induced by elastic loading is fully reversible.

### 2.3.2 Preliminary notes on lattice strain induced broadening in the case of isotropic grain interaction

The general expression for the measurable average lattice strain along the diffraction vector obeys (for proof, see [1]):

$$\epsilon_{\phi,\psi}^{\text{HKL}} = \{\epsilon_{33}^{\mathcal{L}}\}_{\phi,\psi}^{\text{HKL}} = F_{ij}^{\text{HKL}}(\phi, \psi) \cdot \langle \sigma_{ij} \rangle. \quad (2.7)$$

where  $F_{ij}^{\text{HKL}}(\phi, \psi)$  are the x-ray stress factors and  $\langle \sigma_{ij} \rangle$  describes the loading-induced state of mechanical stress. Equation 2.7 is valid even in the case of highly textured or macroscopically elastically anisotropic specimens.

For a quasi-isotropic aggregate (i.e. in the case of macroscopic elastic isotropy), the stress factors can be replaced by the x-ray elastic constants,  $S_1^{\text{HKL}}$  and  $\frac{1}{2}S_2^{\text{HKL}}$  [1,2]. Then, in the case of uniaxial (i.e.  $\sigma_{ij} = 0$  for all  $i, j$  except for  $ij = 11$ ) and biaxially, rotationally symmetric ( $\sigma_{11} = \sigma_{22} \neq 0$ ;  $\sigma_{ij} = 0$ , for  $ij \neq 11 \neq 22$ ) stress states, Equation 2.7 simplifies to a linear relationship between the measured average lattice strain  $\epsilon_{\phi,\psi}^{\text{HKL}}$  and  $\sin^2 \psi$ . The sign of the slope of the straight line obtained by plotting the average lattice strain  $\epsilon_{\phi,\psi}^{\text{HKL}}$  versus  $\sin^2 \psi$  will be positive for tensile uniaxial loading and negative for compressive (uniaxial and biaxially, rotationally symmetric) loading [2].

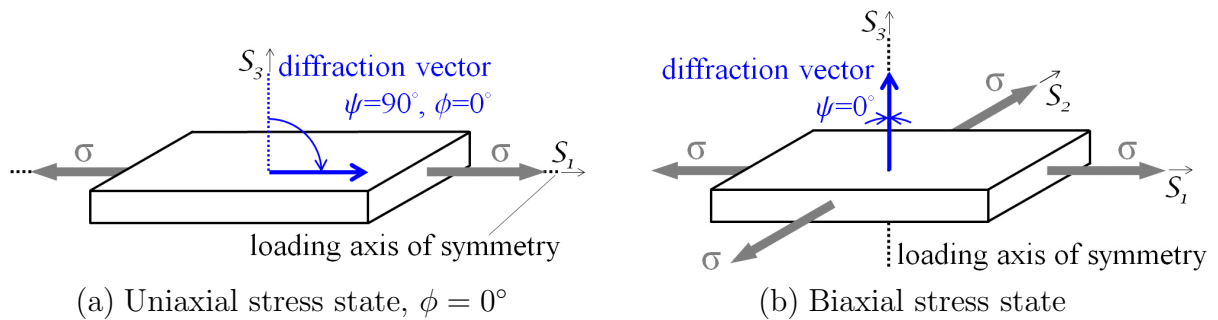


Figure 2.3: Alignment of the loading axis of symmetry with the diffraction vector for two (simple) states of stress as a function of the specimen inclination angle  $\psi$ .

Within the context of isotropic grain interaction, in a quasi-isotropic aggregate for cubic materials, some straight-forward consequences for the lattice-strain distribution induced broadening can be given. The Voigt model implies that the strain components of all grains (in the specimen frame of reference) are identical, i.e. no strain variation and thus no strain-variation induced diffraction-line broadening is predicted by this model. All other isotropic grain-interaction models predict strain variation as a function of grain orientation (in the specimen frame of reference), *also* as a function of  $\chi$ , which results in diffraction-line broadening.

If an isotropic model can be applied for grain interaction, the sign of the uniaxial loading stress  $\sigma$  does not play a role in the magnitude of  $|\epsilon_{\phi,\psi}^{\text{HKL}}(\chi)|$ . Additionally, no strain distribution occurs for the diffracting grains (and hence, no diffraction-line broadening is induced), i.e.  $\epsilon_{\phi,\psi}^{\text{HKL}}(\chi) = \text{const.}$  for variable  $\chi$ , at (i)  $\psi = 90^\circ$  with  $\phi = 0^\circ$  for uniaxial loading along  $\mathcal{S}_1$  [16, 21, 22] and at (ii)  $\psi = 0^\circ$ , independent of  $\phi$  for biaxially rotationally symmetric loading in the  $\mathcal{S}_1, \mathcal{S}_2$  plane. (See Figures 2.3(a) and 2.3(b).) Also, no lattice-strain variation  $\epsilon_{\phi,\psi}^{\text{HKL}}(\chi)$  is expected at fixed  $\phi$  and  $\psi$  angles for  $H00$  and  $HHH$  reflections according to isotropic grain-interaction models for an untextured aggregate of material of cubic crystal symmetry [16, 21, 22]

The lattice-strain distribution  $\epsilon_{\phi,\psi}^{\text{HKL}}(\chi)$  depends strongly on on both stress state and diffraction geometry ( $HKL, \psi, \phi$ ). This can be made clear for the case of isotropic grain interaction by identifying the symmetry axis of the loading state; see Figure 2.3. When the diffraction vector is aligned with the axis of loading symmetry ( $\mathcal{S}_1$  for uniaxial loading,  $\mathcal{S}_3$  for biaxially, rotationally symmetric loading), all *diffracting* grains, independent of their orientations about the diffraction vector, as indicated by the angle  $\chi$ , will experience the same stress state, resulting in no variation in lattice strain in this set of diffracting crystallites. This explain why, at  $\psi = 90^\circ, \phi = 0^\circ$  (for uniaxial loading along  $\mathcal{S}_1$ ) and at  $\psi = 0^\circ$  (independent of  $\phi$ ) for biaxially rotationally symmetric loading (in the  $\mathcal{S}_1, \mathcal{S}_2$  plane), no lattice-strain variation is expected. A special case is a hydrostatic stress state, where any direction represents a loading axis of symmetry, implying, according to the above reasoning, that no line broadening is expected for any orientation of the diffraction vector.

### 2.3.3 Material and model parameters

The strain distribution  $\epsilon_{\phi,\psi}^{\text{HKL}}(\chi)$ , which can be extracted from the grain-interaction models, is dependent on the orientation of the diffraction vector (which is defined by the diffraction planes  $hkl$ , and thus by HKL, sample rotation  $\phi$ , and sample inclination  $\psi$ ), specimen texture (crystallographic and morphological [11]), loading magnitude and state, the type of grain interaction, and the intrinsic elastic single-crystal anisotropy. This work focuses on the diffraction-line broadening induced by mechanical loading of materials of cubic crystal symmetry. The “unloaded” peak width/shape is incorporated

upon convolution with the strain variation profile. Calculations have been made for untextured and (predominantly) 111-fiber textured gold Au ( $a_o = 4.0786 \text{ \AA}$  [29]) and for Cu-K $\alpha_1$  radiation ( $\lambda = 1.54056 \text{ \AA}$  [30]).

Chosen values for the full width at half maximum (FWHM) of reflections for the “unloaded” case are presented in Table 2.2; a Pearson VII profile-shape function, with a shape factor of 1.5 [31], was used for the “unloaded” peak of all reflections. These width values and the shape factor are realistic representations of what could be measured for an Au specimen using synchrotron radiation with a wavelength equal to that of Cu-K $\alpha_1$ .

Table 2.2: FWHM values for various reflections,  $g(2\theta)$ , of Au in unloaded state, representative of synchrotron radiation with a wavelength equal to that of Cu-K $\alpha_1$ . The peaks are described with a Pearson VII profile-shape function with a shape factor of 1.5.

<b>Reflection</b>	111	200	220	311	331
<b>FWHM (<math>^\circ 2\theta</math>)</b>	0.08	0.11	0.23	0.29	0.43

The peak parameters for the diffraction lines of the “loaded” condition  $h(2\theta)$  were determined by fitting the calculated peaks  $h(2\theta)$  (also) with a Pearson VII profile-shape function (see above). The width of each diffraction line is represented by the integral breadth  $\beta$ , which is the integral area of the peak  $A$  divided by the maximum peak intensity  $I$ :

$$\beta = \frac{A}{I}, \quad (2.8)$$

The loading-induced contribution to the total diffraction-line broadening was then taken as the corresponding change in integral breadth:

$$\Delta\beta = \beta^{\text{loaded}} - \beta^{\text{unloaded}}. \quad (2.9)$$

The integral breadth was chosen (as opposed to the FWHM) to define the width of the diffraction peaks as it is less sensitive to the peak shape.

## 2.4 Lattice-strain distributions predicted by grain-interaction models

The results from the grain-interaction model calculations will be displayed as a function of  $\sin^2 \psi$  (at fixed HKL and  $\phi$ ) in three forms: (i) lattice-strain distribution  $\epsilon_{\phi,\psi}^{\text{HKL}}(\chi) = \epsilon_{33}^{\mathcal{L}}(\chi)$  at fixed HKL,  $\phi$ , and  $\psi$ , where the strain of each diffracting grain is plotted separately on an  $\epsilon$ - $\sin^2 \psi$  plot, implying that at fixed ( $HKL$ ,  $\phi$ , and)  $\psi$ , a range of  $\epsilon_{\phi,\psi}^{\text{HKL}}(\chi)$  values occurs, (ii) the average lattice strain  $\epsilon_{\phi,\psi}^{\text{HKL}} = \{\epsilon_{33}^{\mathcal{L}}\}_{\phi,\psi}^{\text{HKL}}$  (this corresponds with the diffraction peak position), and (iii) the diffraction-line broadening  $\Delta\beta$  induced by the elastic loading as corresponding with the lattice-strain distribution  $\epsilon_{33}^{\mathcal{L}}(\chi)$ .

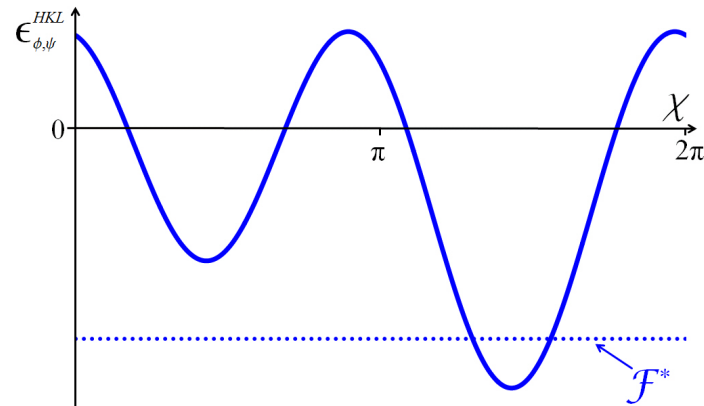
The consequences of the type of grain interaction are investigated by varying the loading conditions (stress state and magnitude), HKL reflection, and texture (both morphological and crystallographic).

### Calculation method

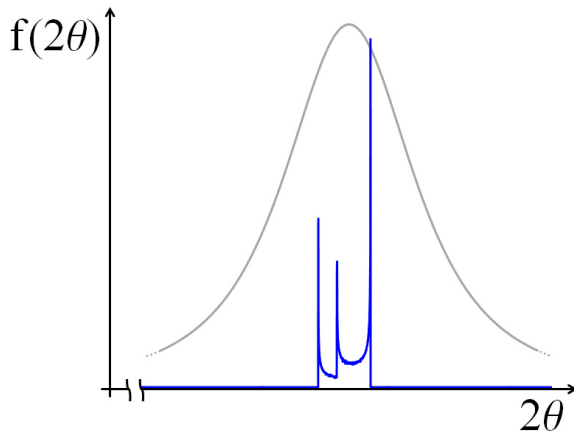
As an example, the lattice-strain variation  $\epsilon_{\phi,\psi}^{\text{HKL}}(\chi)$ , with  $0 \leq \chi \leq 2\pi$ , as induced by uniaxial tensile loading with loading axis along  $\mathcal{S}_1$  (see Figure 2.2), and as observed at  $\phi = 0^\circ$ ,  $\psi = 25^\circ$  ( $\phi$  and  $\psi$  determine the direction of the diffraction vector) for the 331 reflection, as calculated by applying the Reuss model for an untextured Au aggregate (i.e.  $\mathcal{F}$  is constant for all  $\chi$ ; see Section 2.3.1), is shown in Figure 2.4(a). The *strain-induced broadening contribution function*  $f(\epsilon)$  (or  $f(2\theta)$  after transformation to the  $2\theta$  scale by application of Bragg's law) is shown in Figure 2.4(b) and is calculated by mathematically binning the lattice-strain distribution  $\epsilon_{\phi,\psi}^{\text{HKL}}(\chi)$ . This function  $f(\epsilon)$  (or  $f(2\theta)$ ) represents, for this specific diffraction vector, the fraction of diffracting grains which exhibit a given strain (and give rise to a diffraction peak at a corresponding value of  $2\theta$ ). Upon the convolution of  $f(2\theta)$  with  $g(2\theta)$ , the measurable function  $h(2\theta)$  is obtained; see Figure 2.4(c).

In the case of a textured specimen, the role of texture is incorporated upon the calculation of  $f(\epsilon)$ ,  $f(2\theta)$ , where  $\mathcal{F}^*$  is used as a weighting factor. This will be discussed in more detail in Section 2.4.6.

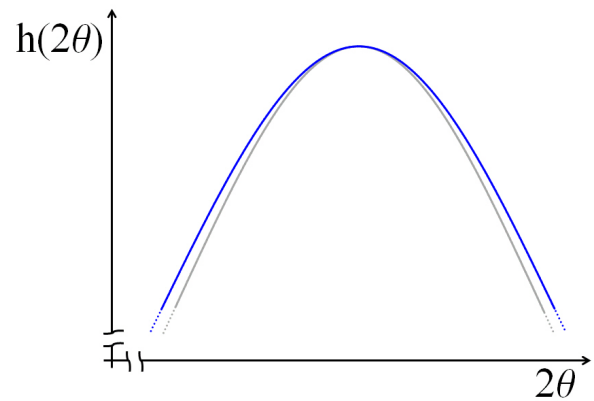
Finally, the average lattice strain  $\epsilon_{\phi,\psi}^{\text{HKL}}$  and the induced broadening  $\Delta\beta$  are extracted from the diffraction lines  $g(2\theta)$  (“unloaded”) and  $h(2\theta)$  (“loaded”) by determining profile parameters by fitting a Pearson VII profile-shape function. For a fixed HKL and  $\phi$  (for a specified ODF, loading state, etc.), the algorithm is executed as a function of  $\psi$ .



(a)  $\epsilon_{\phi,\psi}^{\text{HKL}}$  as a function of  $\chi$  for the 331 reflection with the orientation of the diffraction vector given by  $\phi = 0^\circ$  and  $\psi = 25^\circ$  for an untextured specimen ( $\mathcal{F}^* = \text{const.}$ ); the strain-distribution function shown here corresponds with the strain variation at  $\sin^2 \psi = 0.18$  in Figure 2.10(b)



(b) The *strain-induced broadening contribution function*  $f(2\theta)$  calculated from the strain distribution shown in Figure 2.4(a); the “unloaded” diffraction line  $g(2\theta)$  is shown in gray



(c) “Loaded” peak  $h(2\theta)$ , where the “unloaded” diffraction line  $g(2\theta)$  is shown in gray

Figure 2.4: Steps of the calculation of the strain variation  $\epsilon_{\phi,\psi}^{\text{HKL}}(\chi)$  ( $= \epsilon_{33}^{\mathcal{L}}(\chi)$  at fixed HKL,  $\phi$ , and  $\psi$ ) and the associated diffraction-line broadening as performed for the isotropic, Reuss grain-interaction model for the 331 reflection with the orientation of the diffraction vector given by  $\phi = 0^\circ$  and  $\psi = 25^\circ$  for an untextured Au specimen ( $\mathcal{F}^* = \text{const.}$ ). Uniaxial loading along the  $\mathcal{S}_1$  axis (see Figure 2.2) with  $\sigma_{11} = 100$  MPa.



### 2.4.1 Tensile vs. compressive states of stress; scaling of line broadening

Results obtained for the states of tensile and compressive uniaxial loading along the  $\mathcal{S}_1$ -axis (Figure 2.2) are shown in Figure 2.5 for the 311 reflection ( $\phi = 0^\circ$ ) of an untextured Au aggregate, using the Reuss model for grain interaction. From Figure 2.5(d), it can be seen that even though the sign of the average strain  $\epsilon_{\phi,\psi}^{\text{HKL}}$  at each  $\psi$  differs for the two loading conditions (Figure 2.5(c)), the magnitude of line broadening is identical for both cases because the broadening scales with the width of the strain distribution (Figures 2.5(a) and 2.5(b)), i.e. the range of the *strain-induced broadening contribution function*  $f(2\theta)$ , which is equal for both types of loading. This is a result of linear elasticity.

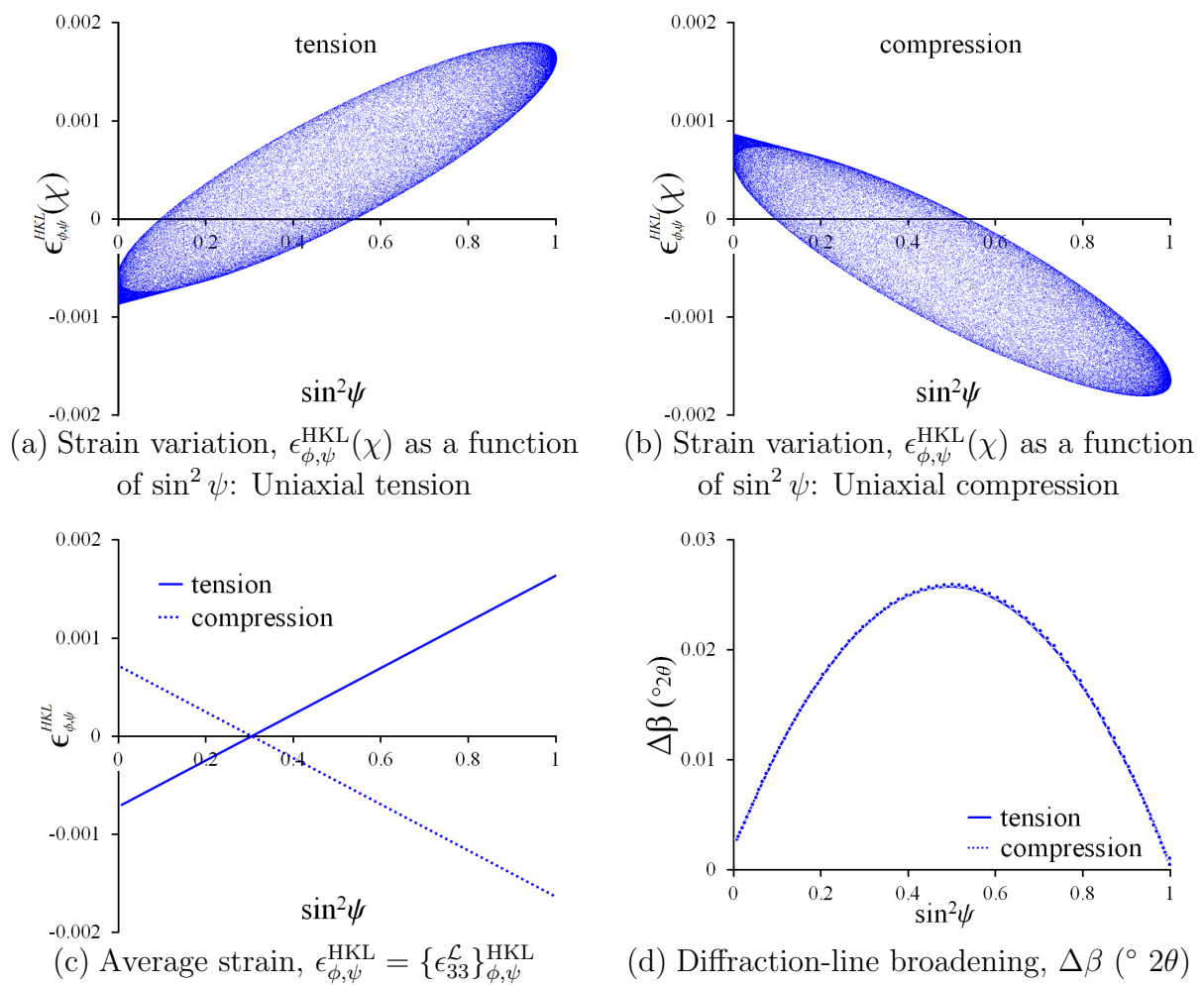


Figure 2.5: Lattice strain and diffraction-line broadening for the cases of tensile and compressive uniaxial loading along the  $\mathcal{S}_1$ -axis ( $|\sigma_{11}| = 100$  MPa) of an untextured Au aggregate; results are shown for the 311 reflection, with the diffraction vector orientations pertaining to  $\phi = 0^\circ$  and variable  $\psi$ , and adopting the Reuss model for grain interaction.

For the same loading axes and the same magnitude of load, a tensile or compressive nature of the load has no effect on the lattice-strain variation  $\epsilon_{\phi,\psi}^{\text{HKL}}(\chi)$ , independent of the type of state of stress and the type of isotropic grain interaction. Line broadening is independent of the sign of the load. For the same state of stress, the induced diffraction-line broadening  $\Delta\beta$  is observed to scale roughly with  $\sigma^2$ ,<sup>1</sup> only as long as the strain broadening is small as compared to the instrumental broadening and for Gaussian shaped instrumental and strain-broadened line profiles. This is approximately the case for the example shown in Figure 2.6(b).

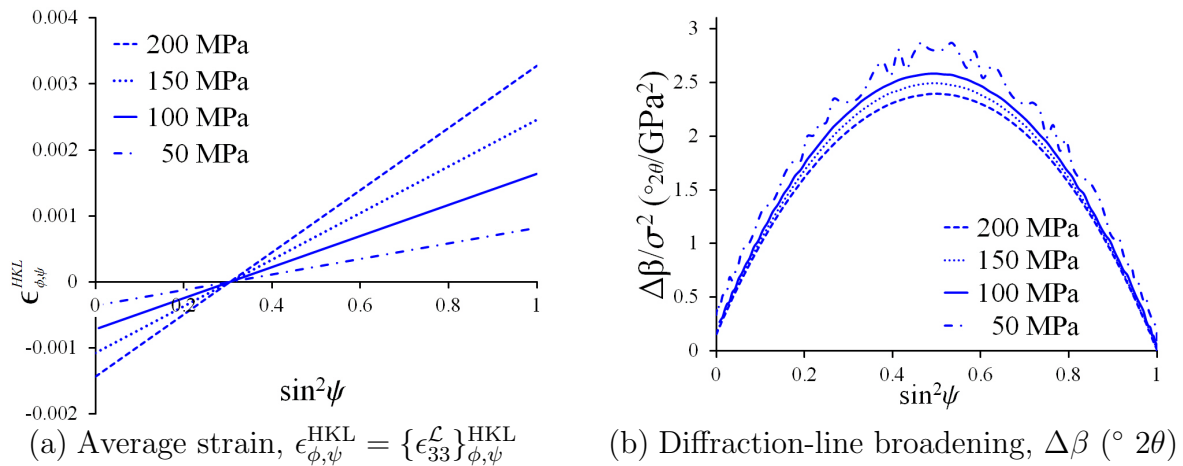


Figure 2.6: Lattice strain and diffraction-line broadening for the case of uniaxial loading along the  $\mathcal{S}_1$ -axis of various magnitudes (ranging from  $\sigma_{11} = 50$  to 200 MPa) of an untextured Au aggregate; results are shown for the 311 reflection, with the diffraction vector orientations pertaining to  $\phi = 0^\circ$  and variable  $\psi$ , and adopting the Reuss model for grain interaction.

<sup>1</sup> Generally, the integral breadth of the only strain broadened profile is proportional to the square root of the strain variance [17, 32–34]. If the strain broadening is small as compared to the instrumental broadening, then, if a Gaussian-shape function is adopted for the instrumental and the only strain-broadened profiles, upon convolution, it follows that the additional broadening in the  $h$  profile as compared to the  $g$  profile (see Equation 2.1) roughly scales with the strain variance, which, in turn, scales with  $\sigma^2$  for isotropic grain interaction [22]. Note, however, that if a Lorentzian (Cauchy) shape function is adopted for the instrumental and the only strain-broadened profiles, then the additional line broadening in the  $h$  profile as compared to the  $g$  profile would scale with the square root of the strain variance, and thus with  $\sigma$ . For a rigorous discussion on (also line-profile shape of) micro-(lattice-)strain broadening, see Reference [35].

## 2.4.2 States of loading

The strain variation  $\epsilon_{\phi,\psi}^{\text{HKL}}(\chi)$  for the 220 reflection of an untextured Au aggregate, under uniaxial tensile loading (along  $\mathcal{S}_1$ ,  $\sigma_{11} = 100$  MPa) and biaxially rotationally symmetric tensile loading ( $\sigma_{\parallel} = \sigma_{11} = \sigma_{22} = 100$  MPa in the  $\mathcal{S}_1, \mathcal{S}_2$  plane), pertaining to  $\phi = 0^\circ$  and variable  $\psi$ , and adoption the Reuss model for grain interaction, is shown as a function of  $\sin^2 \psi$  in Figures 2.7(a) and 2.7(b), respectively. (Note the striking difference with the result for the 311 reflection in Figure 2.5(a), calculated for the same conditions.) Here, for the case of uniaxial loading, clearly no strain variation is observed at  $\psi = 90^\circ$ ,  $\phi = 0^\circ$ , whereas, for biaxial loading, the variation in lattice strain is zero at  $\psi = 0^\circ$ . When, for the applied state of stress and in case of isotropic grain interaction, the loading axis of symmetry (see Figure 2.3) and the diffraction vector are aligned, all grains sharing this diffraction vector will experience the same loading state. Therefore, in such cases, despite the intrinsic elastic anisotropy and as long as isotropic grain interaction holds, no variation of the (average per grain) lattice strain occurs and no diffraction-line broadening is induced. The specific orientation of the specimen (defined by the tilt angle  $\psi$  and the rotation angle  $\phi$ ) establishing that the diffraction vector coincides with the loading axis of symmetry depends on the specific loading state (uniaxial, biaxially symmetric, etc.). For the uniaxial loading case, both the average lattice strain  $\epsilon_{\phi,\psi}^{\text{HKL}}$  and the diffraction-line broadening  $\Delta\beta$ , both at  $\phi = 0^\circ$ , are sensitive to changes in  $\psi$ , whereas at  $\phi = 90^\circ$ ,  $\epsilon_{\phi,\psi}^{\text{HKL}}$  and  $\Delta\beta$  are independent of  $\psi$  (see Figure 2.8). Obviously, for the case of biaxially rotationally symmetric loading, variation of  $\phi$  does not have any effect on  $\epsilon_{\phi,\psi}^{\text{HKL}}$  and  $\Delta\beta$ . (See Section 2.3.2.)

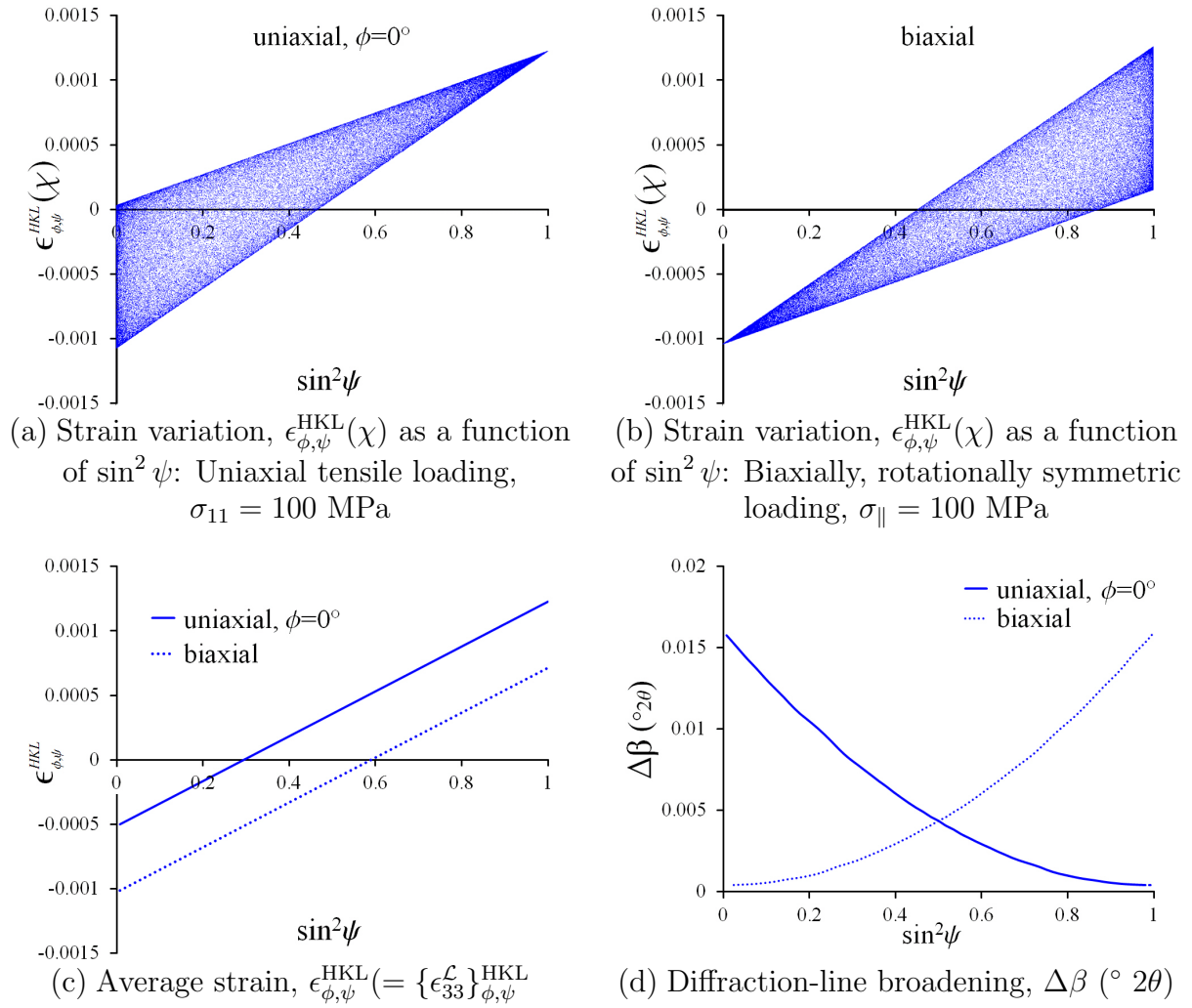


Figure 2.7: Lattice strain and diffraction-line broadening for the cases of tensile uniaxial loading along the  $\mathcal{S}_1$ -axis ( $\sigma_{11} = 100$  MPa) and biaxially, rotationally symmetric tensile loading in the  $\mathcal{S}_1, \mathcal{S}_2$  plane ( $\sigma_{\parallel} = 100$  MPa) of an untextured Au aggregate. Results are shown for the 220 reflection, with the diffraction vector orientations pertaining to  $\phi = 0^{\circ}$  and variable  $\psi$ , and adopting the Reuss model for grain interaction.

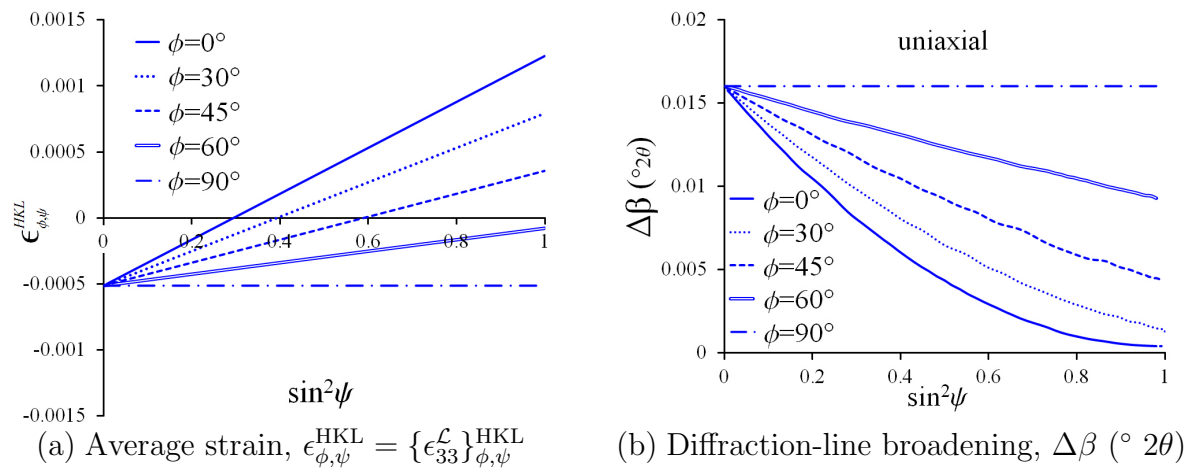


Figure 2.8: Lattice strain and diffraction-line broadening for the case of tensile uniaxial loading along the  $\mathcal{S}_1$ -axis ( $\sigma_{11} = 100$  MPa) of an untextured Au aggregate; results are shown for the 220 reflection, with the diffraction vector orientations pertaining to multiple fixed values of  $\phi$  and variable  $\psi$ , and adopting the Reuss model for grain interaction.

### 2.4.3 Degree of intrinsic elastic anisotropy

The magnitude of the loading-induced diffraction-line broadening will depend on the degree of the intrinsic elastic anisotropy. The diffraction-line broadening according to the Reuss grain-interaction model for three materials is shown in Figure 2.9: Au ( $\mathcal{A} = 2.9$ ), Ni ( $\mathcal{A} = 2.5$ ), and W ( $\mathcal{A} = 1$ ).

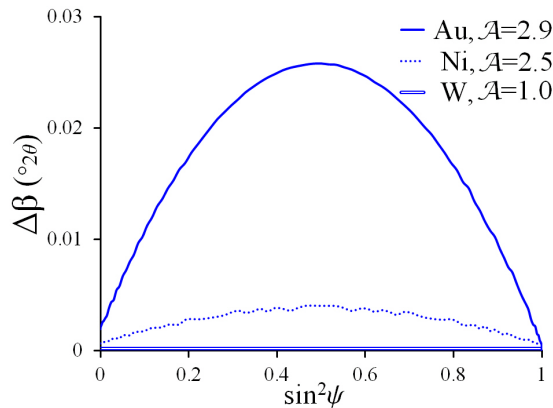


Figure 2.9: Diffraction-line broadening  $\Delta\beta$  ( $^\circ 2\theta$ ) for the case of tensile uniaxial loading along the  $\mathcal{S}_1$ -axis ( $\sigma_{11} = 100$  MPa) of untextured aggregates of Au, Ni, and W. Results are shown for the 220 reflection, with the diffraction vector orientations pertaining to  $\phi = 0^\circ$  and variable  $\psi$ , and adopting the Reuss model for grain interaction.

### 2.4.4 Isotropic grain interactions

The lattice-strain variation  $\epsilon_{\phi,\psi}^{\text{HKL}}(\chi)$  calculated for the 331 reflection at  $\phi = 0^\circ$  as a function of  $\psi$  is shown in Figure 2.10 for an untextured Au aggregate under uniaxial tensile loading ( $\sigma_{11} = 100$  MPa loading along the  $\mathcal{S}_1$ -axis; see Figure 2.3) for the Voigt, Reuss, Neerfeld-Hill, and Eshelby-Kröner ( $\eta = 1$ ) grain-interaction models. The shading of the plots represents the number of grains in the diffracting volume which experience a given average lattice strain. The inset in Figure 2.10(b) illustrates the shading by showing the strain distribution at a fixed  $\psi$ , which is the *strain-induced broadening contribution function*  $f(\epsilon)$  at this fixed value of  $\psi$ . (The calculations shown in Figure 2.4 correspond to the strain variation in Figure 2.10(b) at  $\sin^2\psi = 0.18$ .)

The Voigt model, obviously, reveals no strain variation, independent of  $\psi$ . The Reuss model induces the most extreme degree of strain variation at each  $\psi$ , as compared to the other isotropic grain-interaction models. The lattice-strain broadening calculated through the implementation of the Neerfeld-Hill model is half of that obtained for the Reuss model. The result for the Neerfeld-Hill model is quantitatively similar to the result obtained by application of the Eshelby-Kröner ( $\eta = 1$ ) model (see Figures 2.10(c) and 2.10(d)). This similarity of the strain variations  $\epsilon_{\phi,\psi}^{\text{HKL}}(\chi)$  (and also of the average lattice strains  $\epsilon_{\phi,\psi}^{\text{HKL}}$ ) is in line with the perception that the Eshelby-Kröner model is a compromise between

the two extreme models of Voigt and Reuss [14], and the recognition that the Neerfeld-Hill model is the simple arithmetic “average” of these extreme models. These results thereby indicate that *also* for the prediction of lattice-strain distributions, the use of the simple, analytical Neerfeld-Hill approach can be worthwhile as an alternative for the more advanced, but cumbersome, Eshelby-Kröner approach.

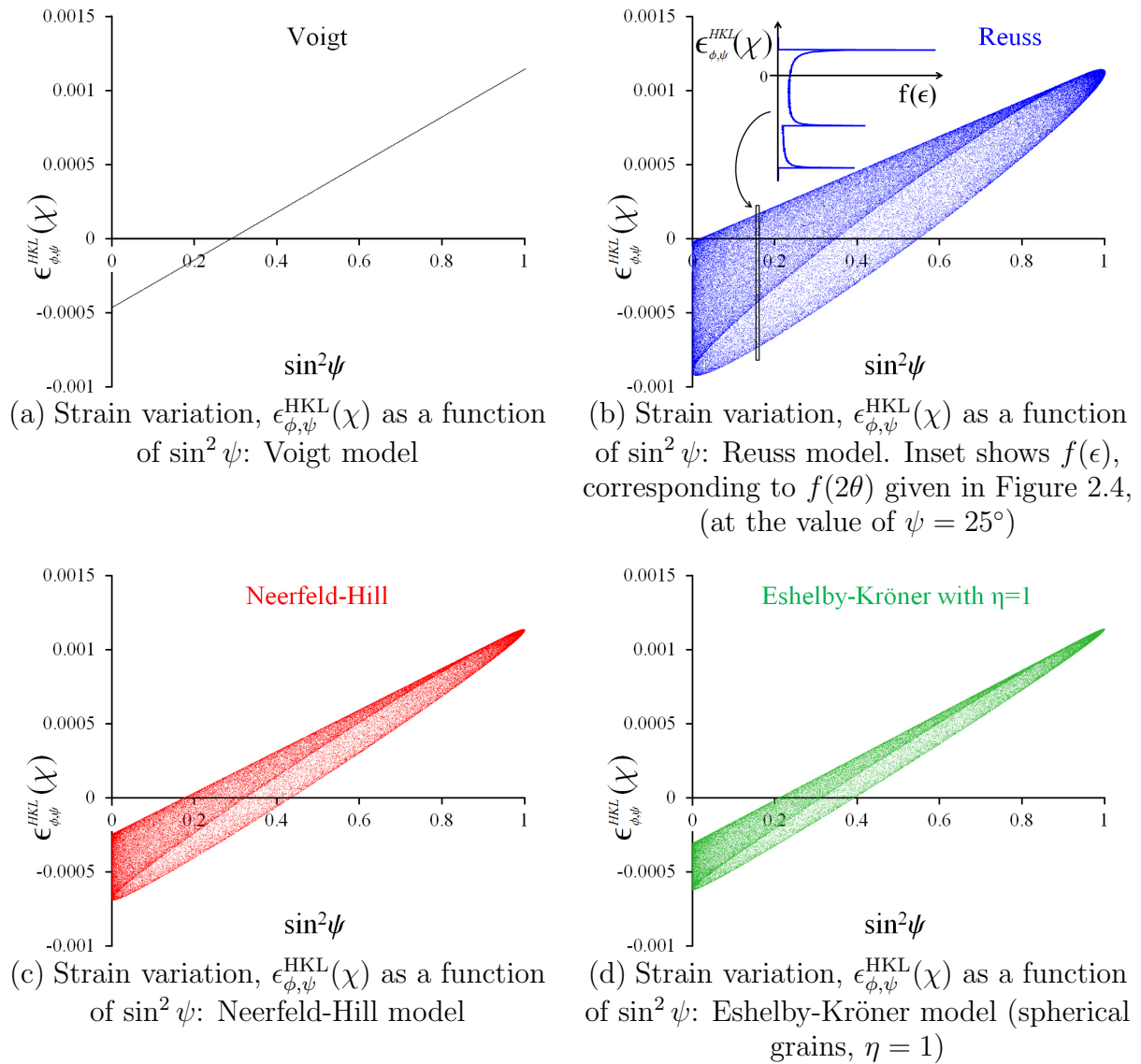


Figure 2.10: Strain variation,  $\epsilon_{\phi,\psi}^{\text{HKL}}(\chi)$  at  $\phi = 0^\circ$  for variable  $\psi$  using various isotropic grain-interaction models for the 331 reflection of an untextured Au aggregate under uniaxial tensile loading along the  $\mathcal{S}_1$  axis ( $\sigma_{11} = 100$  MPa).

### 2.4.5 Anisotropic grain interactions

Results for the direction-dependent grain-interaction models (the Vook-Witt model, the inverse Vook-Witt model, and the Eshelby-Kröner model, with  $\eta = 0.01$  and with  $\eta = 100$ ) are shown in Figure 2.11 for the same conditions as applied for the isotropic grain-interaction models with results shown in Figure 2.10. As was demonstrated in Reference [36] for the average lattice strain  $\epsilon_{\phi,\psi}^{\text{HKL}}$ , the Vook-Witt model approaches the Eshelby-Kröner model for disk-shaped ( $\eta \rightarrow 0$ ) grains, which, as now shown here, apparently also holds for the lattice-strain distribution  $\epsilon_{\phi,\psi}^{\text{HKL}}(\chi)$ ; see Figures 2.11(a) and (b). The inverse Vook-Witt model differs in a fundamental way with the Eshelby-Kröner model for needle-like grains (i.e.  $\eta \rightarrow \infty$ ). This expresses that the Eshelby-Kröner model for needle-like grains cannot satisfy equilibrium if all of the grains experience the same in-plane stress [36]. Indeed, the solutions of both models for also the lattice-strain distributions  $\epsilon_{\phi,\psi}^{\text{HKL}}(\chi)$  exhibit similarities but are not identical. (See Figures 2.11(c) and 2.11(d).)

The overall magnitude of the predicted strain variation differs only in a minor way for the isotropic and anisotropic grain-interaction models (compare Figures 2.10 and 2.11). However, the lattice-strain distribution at a fixed value of  $\psi$ , and thus the corresponding diffraction-line broadening, depends strongly on the choice of the grain-interaction model (see Figures 2.10 and 2.11). The measured diffraction-line *broadening* as a function of  $\phi$  and  $\psi$  (i.e. as a function of the orientation of the diffraction vector) can provide more information on the operating type of grain interaction than possible by inspection of the behavior of only the average lattice strain  $\epsilon_{\phi,\psi}^{\text{HKL}}$  as a function of  $\phi$  and  $\psi$ .



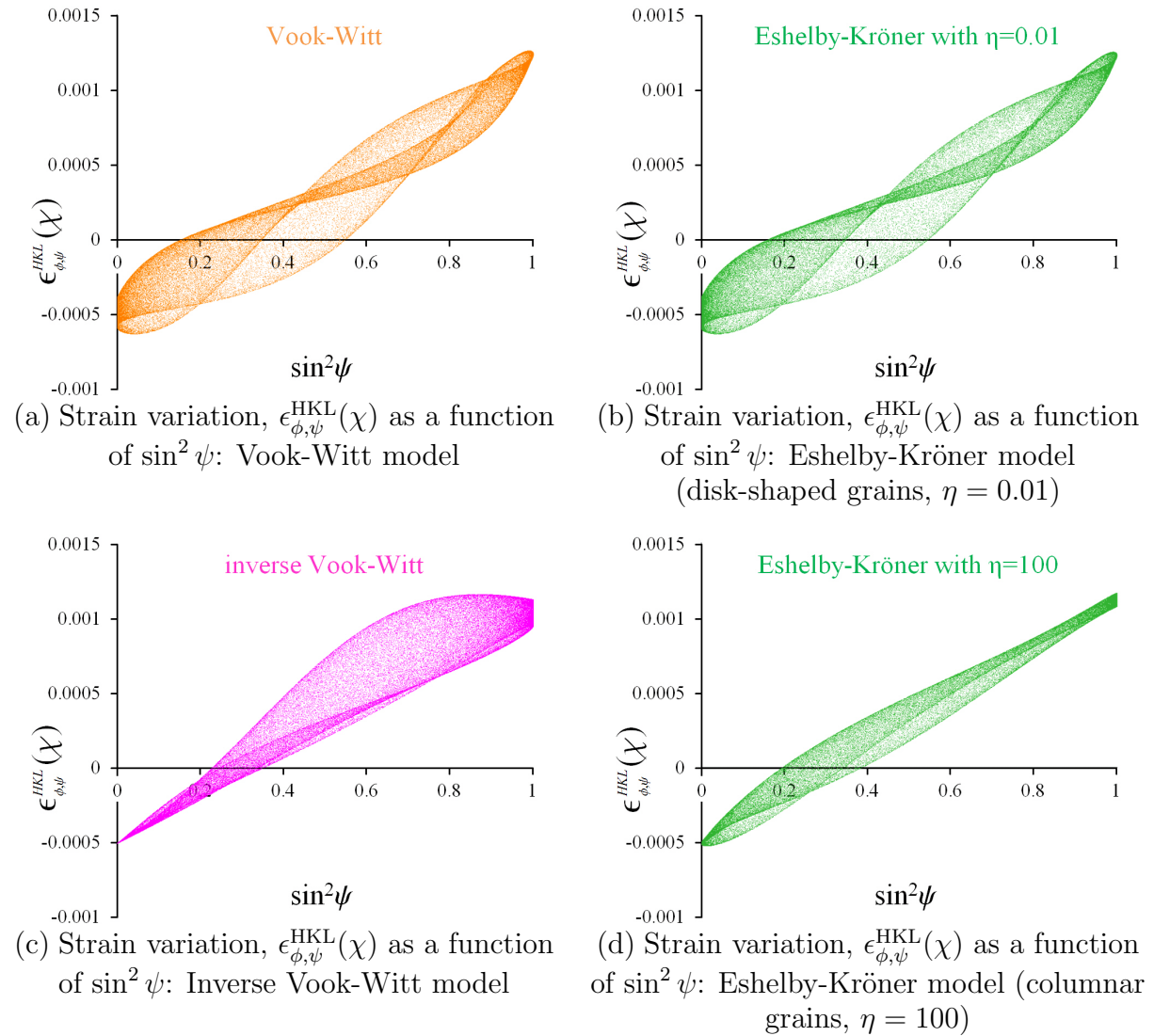


Figure 2.11: Strain variation,  $\epsilon_{\phi,\psi}^{\text{HKL}}(\chi)$  at  $\phi = 0^\circ$  for variable  $\psi$  using anisotropic grain-interaction models for the 331 reflection of an untextured Au aggregate under uniaxial tensile loading along the  $\mathcal{S}_1$  axis ( $\sigma_{11} = 100$  MPa).

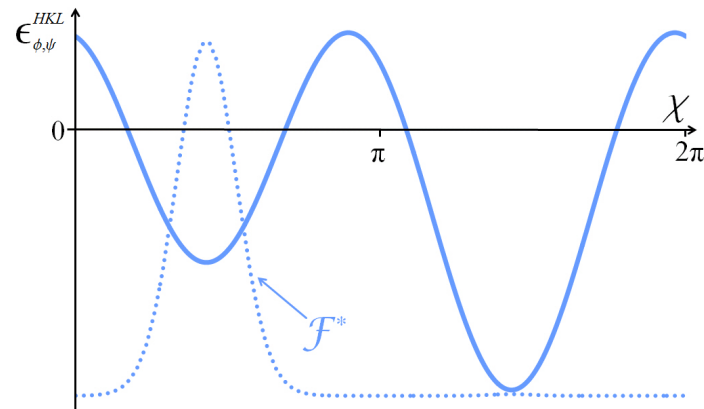
## 2.4.6 Preferred orientation

The alignment of crystallites along a preferred direction will noticeably affect the strain variation in the case of a massive aggregate constituted of elastically anisotropic grains. Therefore, the extent of diffraction-line broadening due to lattice-strain variation (induced by grain interaction) is dependent on the crystallographic texture of the aggregate. As already indicated in the beginning of Section 2.4, the ODF, i.e.  $\mathcal{F}^*$ , is used as a weighting function in the calculation of the *strain-induced broadening contribution function*  $f(\epsilon)$ , and thus  $f(2\theta)$ : compare Figures 2.4(a) and 2.4(b) for an untextured specimen with Figures 2.12(a) and 2.12(b) for a textured specimen. Evidently, for the textured specimen pertaining to Figure 2.12(a), practically no grains are oriented such that they would capture the maximum (or minimum) strain of the calculated strain variation  $\epsilon_{\phi,\psi}^{\text{HKL}}(\chi)$ . As a result, the texture-free aggregate exhibits a higher degree of strain-variation induced broadening than the strongly textured specimen.

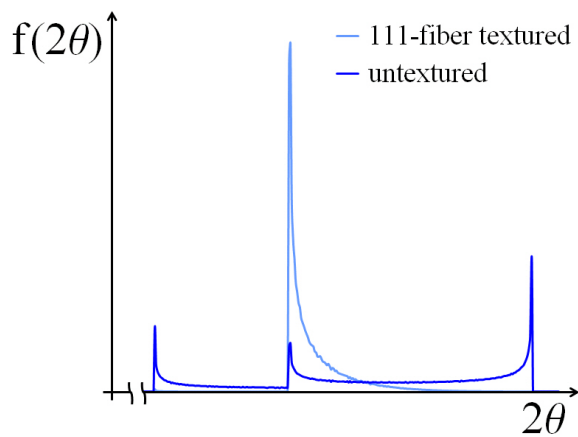
The average lattice strain and the diffraction-line broadening for both an untextured specimen and for a specimen with a (111)-fiber texture, for the same type of uniaxial loading, and for all types of isotropic and anisotropic grain interaction considered in this work, are shown in Figures 2.13 and 2.14. Evidently, texture reduces the overall broadening for almost all sample inclinations  $\psi$ .

Thus, it can be concluded that texture acts as a suppressant of line broadening induced by (external) loading, because the (random) distribution of grains about the diffraction vector is reduced for a textured aggregate (see Figures 2.4(a) and 2.12(a)): a reduced distribution of orientations means a reduced degree of lattice-strain variation and, consequently, a reduced diffraction-line broadening.

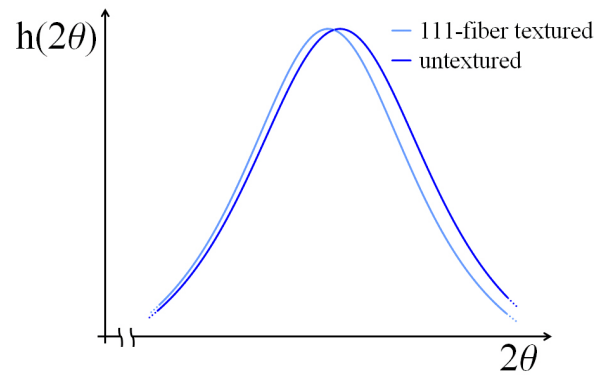
The isotropic and anisotropic grain-interaction models result in comparable magnitudes of diffraction line broadening in the absence of texture, as illustrated by Figures 2.13(c) and 2.14(c). However, texture influences the strain variation much stronger when isotropic grain interaction occurs. This can be understood because in the case of anisotropic grain interaction, texture has a smaller relative contribution to the “anisotropic behavior” of the specimen.



(a)  $\epsilon_{\phi,\psi}^{HKL}$  as a function of  $\chi$  for the 331 reflection with the orientation of the diffraction vector given by  $\phi = 0^\circ$  and  $\psi = 25^\circ$  for an untextured specimen ( $\mathcal{F}^*$  shown for a 111-fiber texture); compare with Figure 2.4(a), where  $\mathcal{F}^* = \text{const.}$

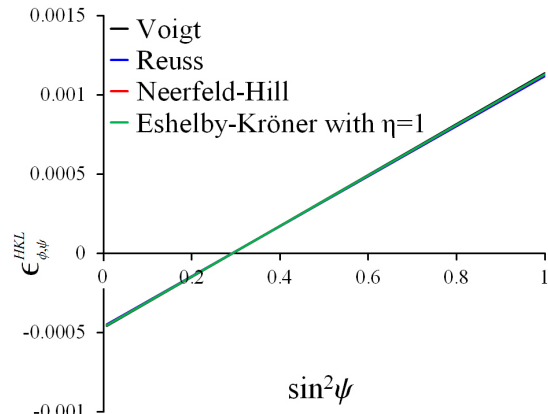


(b) Comparison of *strain-induced broadening contribution functions*  $f(2\theta)$  (calculated from  $\epsilon_{\phi,\psi}^{HKL}(\chi)$ ) for an untextured aggregate ( $\mathcal{F}^* = \text{const.}$ , Figure 2.4(a)) shown in dark blue and a 111-fiber textured aggregate ( $\mathcal{F}^* \neq \text{const.}$ , Figure 2.12(a)) shown in light blue

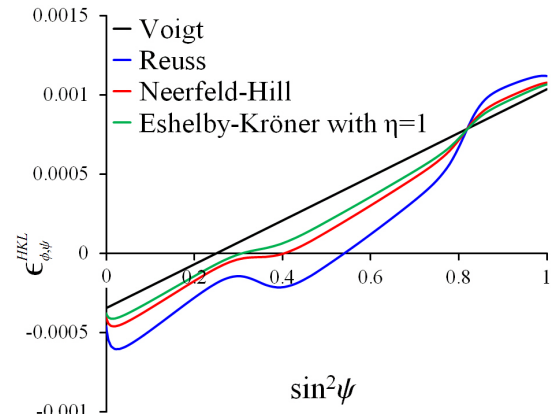


(c) “Loaded” diffraction lines  $h(2\theta)$  demonstrating the role of texture on broadening and peak shift. The “unloaded” diffraction line  $g(2\theta)$  is not shown. See Figure 2.4(a) for an untextured aggregate ( $\mathcal{F}^* = \text{const.}$ , shown here in dark blue) and Figure 2.12(a) for a 111-fiber textured aggregates ( $\mathcal{F}^* \neq \text{const.}$ , shown here in light blue).

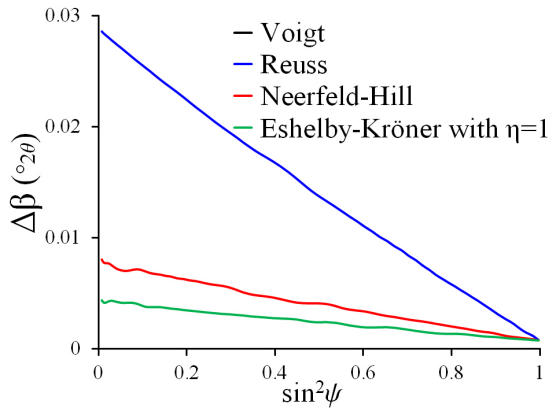
Figure 2.12: Steps of the calculation of the strain variation  $\epsilon_{\phi,\psi}^{HKL}(\chi)$  ( $= \epsilon_{33}^{\mathcal{L}}(\chi)$  at fixed HKL,  $\phi$ , and  $\psi$ ) and the associated diffraction-line broadening as performed for the isotropic, Reuss grain-interaction model for the 331 reflection with the orientation of the diffraction vector given by  $\phi = 0^\circ$  and  $\psi = 25^\circ$  for a textured Au specimen ( $\mathcal{F}^*$  for a 111-fiber texture). Compare with Figure 2.4 for an untextured Au aggregate. Uniaxial loading along the  $\mathcal{S}_1$  axis (see Figure 2.2) with  $\sigma_{11} = 100$  MPa.



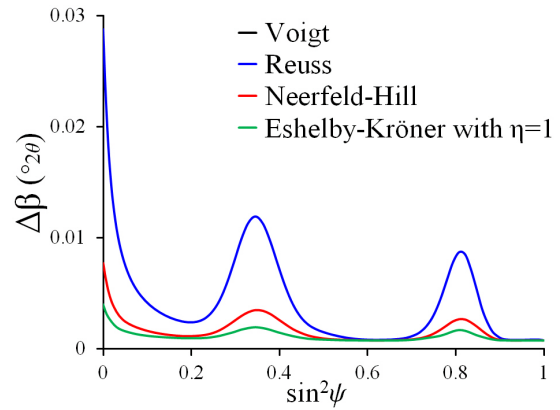
(a) Average lattice strain,  $\epsilon_{\phi,\psi}^{\text{HKL}}$  as a function of  $\sin^2\psi$ : Untextured aggregate



(b) Average lattice strain,  $\epsilon_{\phi,\psi}^{\text{HKL}}$  as a function of  $\sin^2\psi$ : 111-fiber textured aggregate

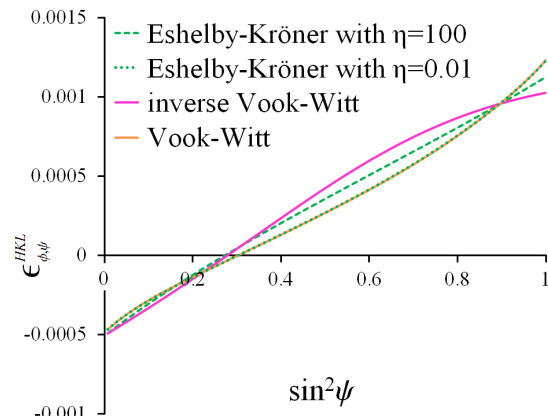


(c) Diffraction-line broadening,  $\Delta\beta$  ( $^\circ 2\theta$ ): Untextured aggregate

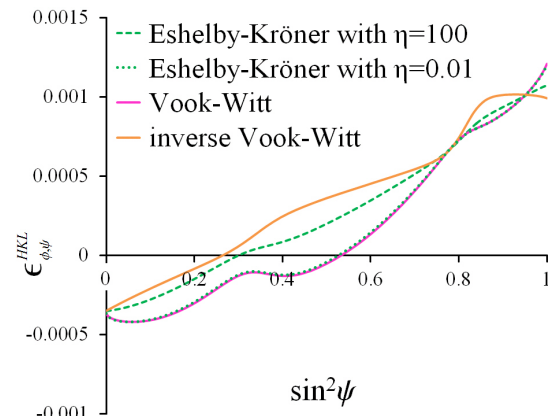


(d) Diffraction-line broadening,  $\Delta\beta$  ( $^\circ 2\theta$ ): 111-fiber textured aggregate

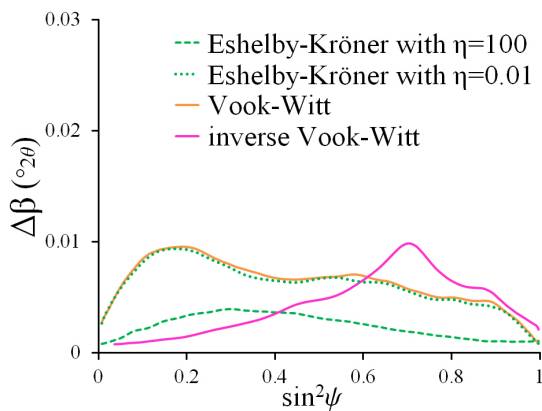
Figure 2.13: Average lattice strain  $\epsilon_{\phi,\psi}^{\text{HKL}}$  and diffraction-line broadening  $\Delta\beta$  for the case of tensile uniaxial loading along the  $\mathcal{S}_1$ -axis ( $\sigma_{11} = 100$  MPa). Results are shown for the 331 reflection, with the diffraction vector orientations pertaining to  $\phi = 0^\circ$  and variable  $\psi$ , and adopting the indicated *isotropic* grain-interaction models (see legend) for both an untextured and a 111-fiber textured Au aggregate. These calculations correspond to  $\epsilon_{\phi,\psi}^{\text{HKL}}(\chi)$  given in Figure 2.10.



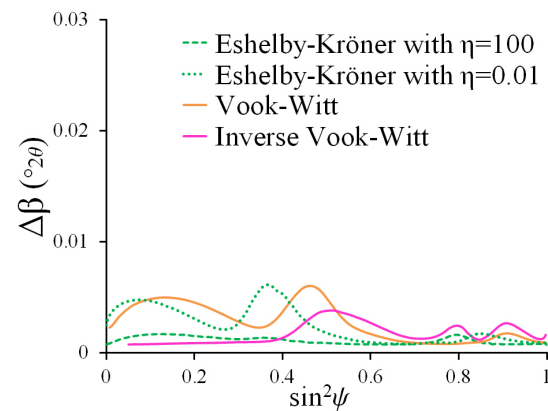
(a) Average lattice strain,  $\epsilon_{\phi,\psi}^{\text{HKL}}$  as a function of  $\sin^2 \psi$ : Untextured aggregate



(b) Average lattice strain,  $\epsilon_{\phi,\psi}^{\text{HKL}}$  as a function of  $\sin^2 \psi$ : 111-fiber textured aggregate



(c) Diffraction-line broadening,  $\Delta\beta$  ( $^\circ 2\theta$ ): Untextured aggregate



(d) Diffraction-line broadening,  $\Delta\beta$  ( $^\circ 2\theta$ ): 111-fiber textured aggregate

Figure 2.14: Average lattice strain  $\epsilon_{\phi,\psi}^{\text{HKL}}$  and diffraction-line broadening  $\Delta\beta$  for the case of tensile uniaxial loading along the  $\mathcal{S}_1$ -axis ( $\sigma_{11} = 100$  MPa). Results are shown for the 331 reflection, with the diffraction vector orientations pertaining to  $\phi = 0^\circ$  and variable  $\psi$ , and adopting the indicated *anisotropic* grain-interaction models (see legend) for both an untextured and a 111-fiber textured Au aggregate. These calculations correspond to  $\epsilon_{\phi,\psi}^{\text{HKL}}(\chi)$  given in Figure 2.11.

### 2.4.7 $H00$ and $HHH$ reflections

It is well known that, in the case of isotropic grain interaction, even in the presence of texture,  $H00$  and  $HHH$  reflections of an aggregate of material of cubic symmetry show still straight lines in plots of  $\epsilon_{\phi,\psi}^{\text{HKL}}$  versus  $\sin^2 \psi$  (see Section 2.3.2), where curvature occurs for HKL reflections in general. In the case of anisotropic grain interaction, it has been shown that in plots of  $\epsilon_{\phi,\psi}^{\text{HKL}}$  versus  $\sin^2 \psi$  curvature does appear also for the  $H00$  and  $HHH$  reflections [37]. Against this background, it appears compulsory to investigate the role of these reflections from cubic materials for the occurring strain-variation induced broadening in the presence of texture.

As was remarked in Section 2.3.2, no lattice-strain variation  $\epsilon_{\phi,\psi}^{\text{HKL}}(\chi)$  is expected at fixed  $\phi$  and  $\psi$  angles for  $H00$  and  $HHH$  reflections according to *isotropic* grain-interaction models for an untextured aggregate of material of cubic crystal symmetry. The line broadening predicted for the 111 and 200 reflections of an elastically loaded Au aggregate, considering *anisotropic* grain interactions is shown in Figures 2.15 and 2.16, respectively, for untextured and 111-fiber textured aggregates.

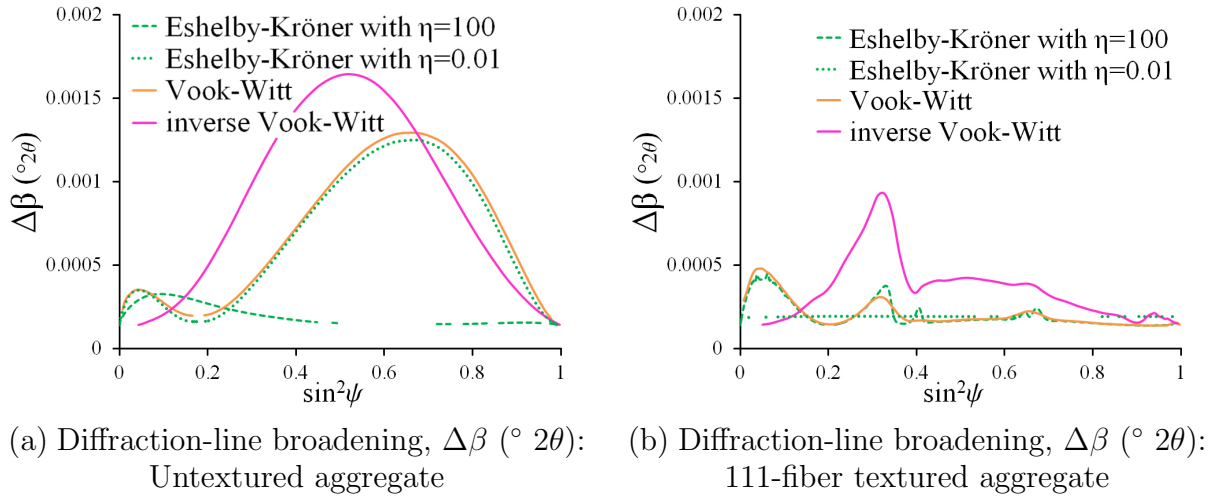


Figure 2.15: Diffraction-line broadening  $\Delta\beta$  for the case of tensile uniaxial loading along the  $\mathcal{S}_1$ -axis ( $\sigma_{11} = 100$  MPa). Results are shown for the 111 reflection, with the diffraction vector orientations pertaining to  $\phi = 0^{\circ}$  and variable  $\psi$ , and adopting the indicated *anisotropic* grain-interaction models (see legend) for both an untextured and a 111-fiber textured Au aggregate.

Evidently, anisotropic grain interactions in cubic materials lead not only to deviation of linearity in  $\sin^2 \psi$  plots (e.g. for a plane state of stress; see also discussion in [37]), but also to distinct diffraction-line broadening which, moreover, is strongly dependent on  $\psi$  (and  $\phi$ ), i.e. dependent on the orientation of the diffraction vector. It should be emphasized that it is not the intrinsic elastic anisotropy of the grains that predominates the extent of these effects, but these outcomes (see Section 2.5) are governed by the type of operating grain interaction. (Note that, as discussed in Section 2.4.6, the extent of

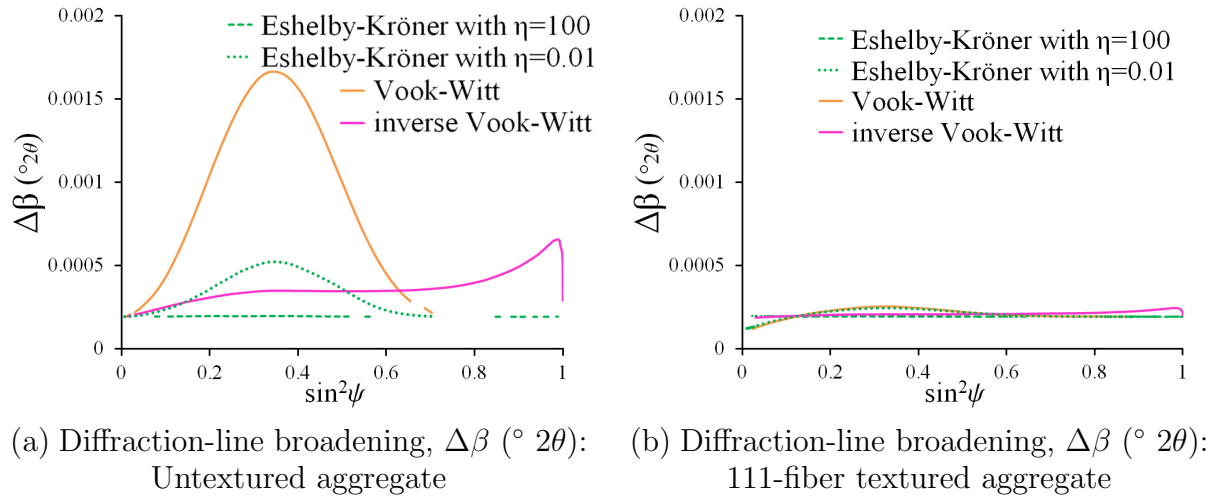


Figure 2.16: Diffraction-line broadening  $\Delta\beta$  for the case of tensile uniaxial loading along the  $\mathcal{S}_1$ -axis ( $\sigma_{11} = 100$  MPa). Results are shown for the 200 reflection, with the diffraction vector orientations pertaining to  $\phi = 0^\circ$  and variable  $\psi$ , and adopting the indicated *anisotropic* grain-interaction models (see legend) for both an untextured and a 111-fiber textured Au aggregate.

diffraction-line broadening is reduced in the presence of texture.)

## 2.5 Strain variation predictions by finite element analysis

Three categories of strain variation may be present in an elastically loaded polycrystalline aggregate: (i) macro-, (ii) meso-, and (iii) microvariation in strain.

- (i) *Macrovariation* in strain is the variation of the average lattice strain, taken for the groups of diffracting grains, that occurs upon changing the orientation of the diffraction vector with respect to the specimen frame of reference. This macrovariation in lattice strain is expressed in this paper by the variation of  $\epsilon_{\phi,\psi}^{\text{HKL}}$  (as a function of  $\sin^2\psi$ ).
- (ii) *Mesovariation* in strain is the variation of the average lattice strain, the average now taken per diffracting grain, for the group of diffracting grains sharing a fixed orientation of the diffraction vector. This mesovariation in lattice strain is expressed in this paper by the variation of  $\epsilon_{\phi,\psi}^{\text{HKL}}(\chi)$ .
- (iii) *Microvariation* in strain is the variation of lattice strain within an individual grain.

It is essential to recognize that all published grain-interaction models do not take into account the above described *microvariation* of strain. It has been shown experimentally that the variation of lattice spacing within a single grain in a polycrystal can be significant (for an example, see Reference [38]).

A second shortcoming of the grain-interaction models is that the (average) lattice strain for a diffracting grain is considered to be only dependent on the angle of rotation around the diffraction vector  $\chi$ , i.e. the role of the immediately surrounding, neighboring grains, in particular their crystallographic orientations and shapes, which can have pronounced influence on the actually experienced grain interaction by the grain concerned, is not considered.

Both of these shortcomings of the grain-interaction models lead to *underestimates* of the strain variation, and thus the loading-induced diffraction-line broadening, occurring in reality. Two types of *mesovariation* of lattice strain are distinguished in the following: (a) mesovariation by variable  $\chi$  (as considered in the grain-interaction models) and (b) mesovariation at constant  $\chi$  due to different local surroundings.

Even if grains of identical orientation and geometry within a completely untextured aggregate are considered, the neighboring crystallites of those grains will statistically differ in orientation. This will result in both mesovariation (type (b); see above) and microvariation of lattice strain (ignored in all grain-interaction models). The actual, local loading of every grain (including each of those grains with identical orientation in the  $\mathcal{S}$  frame) in a polycrystal will depend (additionally) on its nearest neighbors (immediate surroundings), i.e. it does not solely depend on the macroscopically applied loading. The analysis of such additional sources of strain variation can be examined by application of finite element analysis (FEA). In the following, both the microvariation and the second type of mesovariation of lattice strain are exhibited by the FEA calculations discussed here.

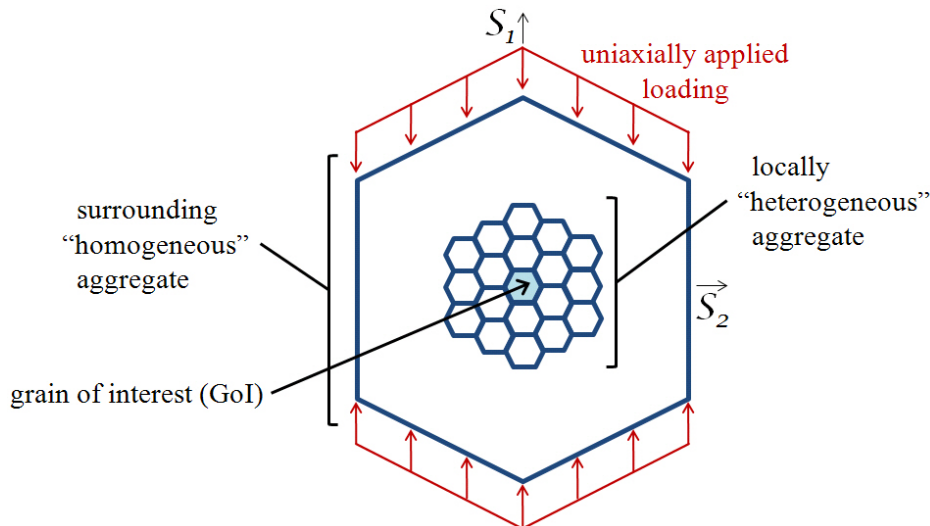


Figure 2.17: Free body diagram for FEA computation consisting of a *locally heterogeneous aggregate* and a *surrounding homogeneous aggregate* with the grain of interest (GoI) at the center where uniaxial compressive loading along the  $S_1$  axis ( $\sigma_{11} = -100$  MPa) is applied.



As the present FEA investigation is concerned with the role of the *local* environment on the strain (distribution) for the diffracting grains, the devised model system consists of two parts: (i) a *locally heterogeneous aggregate* (inclusion) composed of a number of “columnar” grains (of identical shape and size) with different crystal orientations and (ii) a *surrounding homogeneous aggregate* (matrix) characterized by the macroscopic (comparable to the bulk material) elastic properties (Figure 2.17). At the center of the *locally heterogeneous aggregate* lies a grain which will be termed the “grain of interest” (GoI). In the following, the average strain and the strain distribution for the GoI, as a function of variation in the local surroundings, are the focus of the attention.

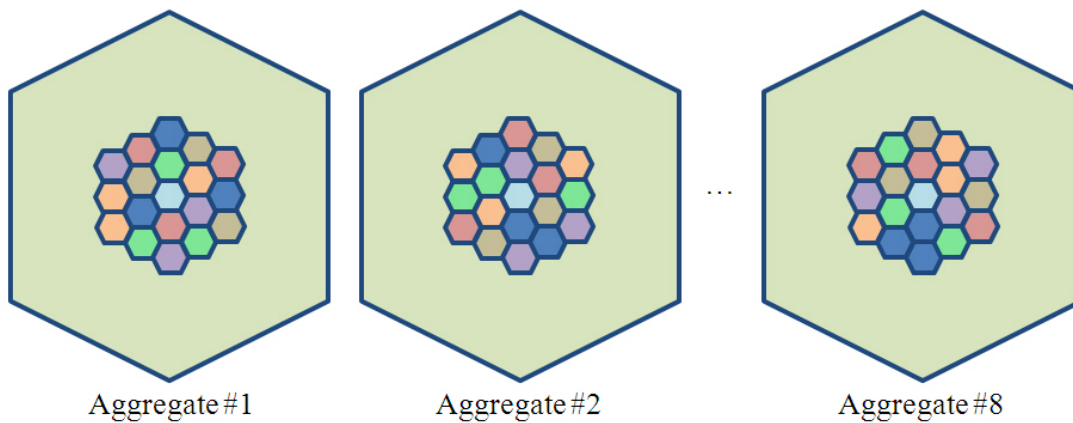


Figure 2.18: Arrangement of “grains” in *locally heterogeneous aggregates* for FEA computation where color is used to identify a specific crystallographic orientation of the compliance tensor (representing a grain orientation); see the Appendix and Table 2.5.

The *surrounding homogeneous aggregate* represents the grains far from the GoI whose individual orientations have little effect on the induced strain field in the GoI and can be averaged together to act as a homogeneous body. (This resembles the “effective medium” used in the Eshelby-Kröner model.) The *locally heterogeneous aggregate* is comprised of individual grains as shown in Figures 2.17 and 2.18. Eight different configurations of the grains in the *locally heterogeneous aggregate* were constructed to properly investigate the effect of the local heterogeneity on the strain in the GoI. The elastic constants used to describe the compliance of the surrounding homogeneous aggregate, the geometry of the “grains” (which make up the locally heterogeneous aggregate), and the crystal orientation of the GoI remained unchanged for all eight aggregates; only the crystal orientations of the individual, GoI-surrounding grains (represented by color in Figure 2.18) in the *locally heterogeneous aggregate* were varied.

The single-crystal elasticity tensor  $\mathbf{C}^C$  for Au can be rotated using the Bunge Euler angles  $\alpha$ ,  $\beta$ , and  $\gamma$  in the reverse transformation tensor to solve for the compliance of a grain in the  $\mathcal{S}$  frame. (See discussion in Section 2.3.1 and Appendix 2.8.) Several different “grain orientations” were computed: one selected for the GoI and six others to populate the rest of the *locally heterogeneous aggregate*. In Figure 2.18, color corresponds

to a unique set of Euler angles  $\alpha$ ,  $\beta$ ,  $\gamma$  to fully define the grain orientation. The values calculated for strain variation, by adopting (only) six different orientations of the GoI-surrounding grains, can be thought of as a lower bound to those which could actually be present in a realistic polycrystalline specimen under loading.

As specific lattice directions yield sooner than others (and therefore are more sensitive to variations of local inhomogeneity), four different orientations of the crystal lattice and thus the compliance tensor with respect to the orientation of the diffraction vector, which is oriented perpendicular to the plane of drawing in Figures 2.17 and 2.18, were used for the GoI, representing four  $HKL$  reflections: 111, 200, 220, and 311.

The hexagonal shape of the “columnar” grains mirrors the energetically favorable two-dimensional grain shape (assuming isotropic grain-boundary stress [39]) and was chosen in order to keep the geometry of the problem simple. The external shape of the surrounding homogeneous aggregate was chosen to resemble the shape of the locally heterogeneous aggregate (inclusion). It is important that the values determined for the stress and strain components along the external boundaries of the *surrounding homogeneous aggregate* are independent of changes within the *locally heterogeneous aggregate* (as shown in Figure 2.18). The size of the *surrounding homogeneous aggregate* was therefore chosen large enough to be compatible with this requirement, as the whole system (the *locally heterogeneous* surroundings of the GoI in the inclusion and the *homogeneous* matrix surrounding the inclusion) must act as a unchanging effective medium for the GoI.

The body was loaded uniaxially (along the  $\mathcal{S}_1$  axis as indicated in Figure 2.17) to induce macroscopic elastic strains comparable to those discussed in Section 2.4. For the discussion of strain variation, it is important to refer back to the three frames of reference defined in Section 2.3.1. The average lattice strain measured using XRD is defined in the laboratory frame of reference:  $\{\epsilon_{33}^{\mathcal{L}}\}_{\phi,\psi}^{\text{HKL}}$  ( $= \epsilon_{\phi,\psi}^{\text{HKL}}$ ; Equation 2.6). The results of FEA for the GoI are given in the specimen frame of reference:  $\epsilon_{11}^{\mathcal{S}}$ ,  $\epsilon_{22}^{\mathcal{S}}$ ,  $\epsilon_{33}^{\mathcal{S}}$  with the  $\mathcal{S}_1$  and  $\mathcal{S}_2$  axes oriented as indicated in Figure 2.17 and the  $\mathcal{S}_3$  axis oriented perpendicularly to the plane of drawing, i.e. parallel to the diffraction vector considered. Therefore, the variation of the value of the calculated strain component  $\epsilon_{33}^{\mathcal{S}}$  for the GoI in the various aggregates should be compared with the variation of  $\epsilon_{33}^{\mathcal{L}} \text{HKL}_{\phi,\psi}(\chi)$  as calculated according to the grain-interaction models.

The FEA was performed using the software COMSOL Multiphysics 4.0a<sup>®</sup>. The grains were treated as continuous, elastically-deformable bodies, each with the same anisotropic compliance tensor in the  $\mathcal{C}$  frame. The calculations were carried out adopting the single-crystal elastic constants for Au, where the compliance of each grain in the specimen frame of reference is a function of the crystallite orientation, represented by Euler angles [24, 40–42]. (See Reference [36] and Section 2.3.1 for more details.)

The results of the FEA simulations are presented in Figure 2.19, by means of contour plots of the  $\epsilon_{33}^{\mathcal{S}}$  component of the strain tensor for the GoI in each of the eight simulated aggregate configurations for four different orientations of the GoI, i.e. pertaining to the

111, 200, 220, and 311 reflections (see Table 2.5). The corresponding minimum, maximum, and average values of  $\epsilon_{33}^S$  for the GoI have been gathered in Table 2.3.

As a first conclusion, it is interesting to note, though, that whether an “isotropic” or an “anisotropic” orientation of the GoI is investigated (i.e. whether an  $H00$  or  $HHH$  reflection or a general HKL reflection is considered), both distinct micro- and mesovariation in strain (see beginning of this section) are observed.

The distribution of strain, within the GoI, clearly depends on the arrangement of the elastically anisotropic grains in the *locally heterogeneous aggregate*: the orientation of the neighbor/adjacent grains noticeably affects the strain distribution within a grain. Also the average strain of the GoI depends on the *locally heterogeneous* surroundings.

These results demonstrate that grains with identical orientations located throughout a homogeneous aggregate subjected to macroscopic loading will not necessarily exhibit the same average strain. This implies the occurrence of mesovariation of strain also for diffraction grains with the same angle of rotation about the diffraction vector. Recall, such strain variation is not considered in all grain-interaction models. Moreover, an appreciable microvariation of strain, i.e. strain distribution within a grain, occurs, which is also ignored in all grain-interaction models. The mesovariation of the strain for grains of identical orientation and the microvariation of the strain within a grain contribute essentially to the loading-induced diffraction-line broadening.

Table 2.3: FEA results for the  $\epsilon_{33}^S$  strain component in the GoI (i.e.  $\epsilon_{33}^L(\text{HKL}, \phi, \psi, \chi)$  at  $\phi = 0^\circ$ ,  $\psi = 0^\circ$  and for  $\chi = 0^\circ$ ) for uniaxial compressive loading with  $\sigma_{11} = -100$  MPa (as indicated in Figure 2.17; see also text) for four orientations of the GoI (A: 111; B: 200; C: 220; D: 311) and for the eight different surroundings of the GoI. The corresponding contour plots are presented in in Figure 2.19.

Aggregate	Average ( $1 \cdot 10^{-3}$ )	Minimum ( $1 \cdot 10^{-3}$ )	Maximum ( $1 \cdot 10^{-3}$ )	Microvariation of strain ( $1 \cdot 10^{-3}$ )
GoI: A (111 reflection)				
#1	0.96	0.86	1.05	0.19
#2	0.94	0.84	1.15	0.31
#3	0.92	0.84	1.01	0.18
#4	0.95	0.84	1.06	0.22
#5	0.97	0.87	1.10	0.23
#6	0.92	0.82	1.01	0.20
#7	0.94	0.83	1.12	0.29
#8	0.94	0.87	1.05	0.18
GoI: B (200 reflection)				
#1	1.28	1.09	1.39	0.30
#2	1.25	1.07	1.57	0.49
#3	1.22	1.07	1.38	0.32
#4	1.26	1.06	1.45	0.39
#5	1.30	1.16	1.51	0.35
#6	1.23	1.08	1.35	0.27
#7	1.26	1.10	1.53	0.43
#8	1.24	1.11	1.38	0.26
GoI: C (220 reflection)				
#1	1.09	0.97	1.20	0.23
#2	1.08	0.91	1.26	0.35
#3	1.04	0.94	1.19	0.25
#4	1.07	0.96	1.23	0.27
#5	1.11	0.95	1.23	0.27
#6	1.04	0.87	1.21	0.34
#7	1.08	0.89	1.25	0.37
#8	1.06	0.93	1.14	0.22
GoI: D (311 reflection)				
#1	1.15	1.03	1.30	0.27
#2	1.12	0.96	1.32	0.36
#3	1.09	0.95	1.20	0.24
#4	1.13	1.00	1.30	0.30
#5	1.16	1.05	1.35	0.29
#6	1.10	0.96	1.21	0.24
#7	1.12	1.04	1.29	0.25
#8	1.11	0.97	1.30	0.33

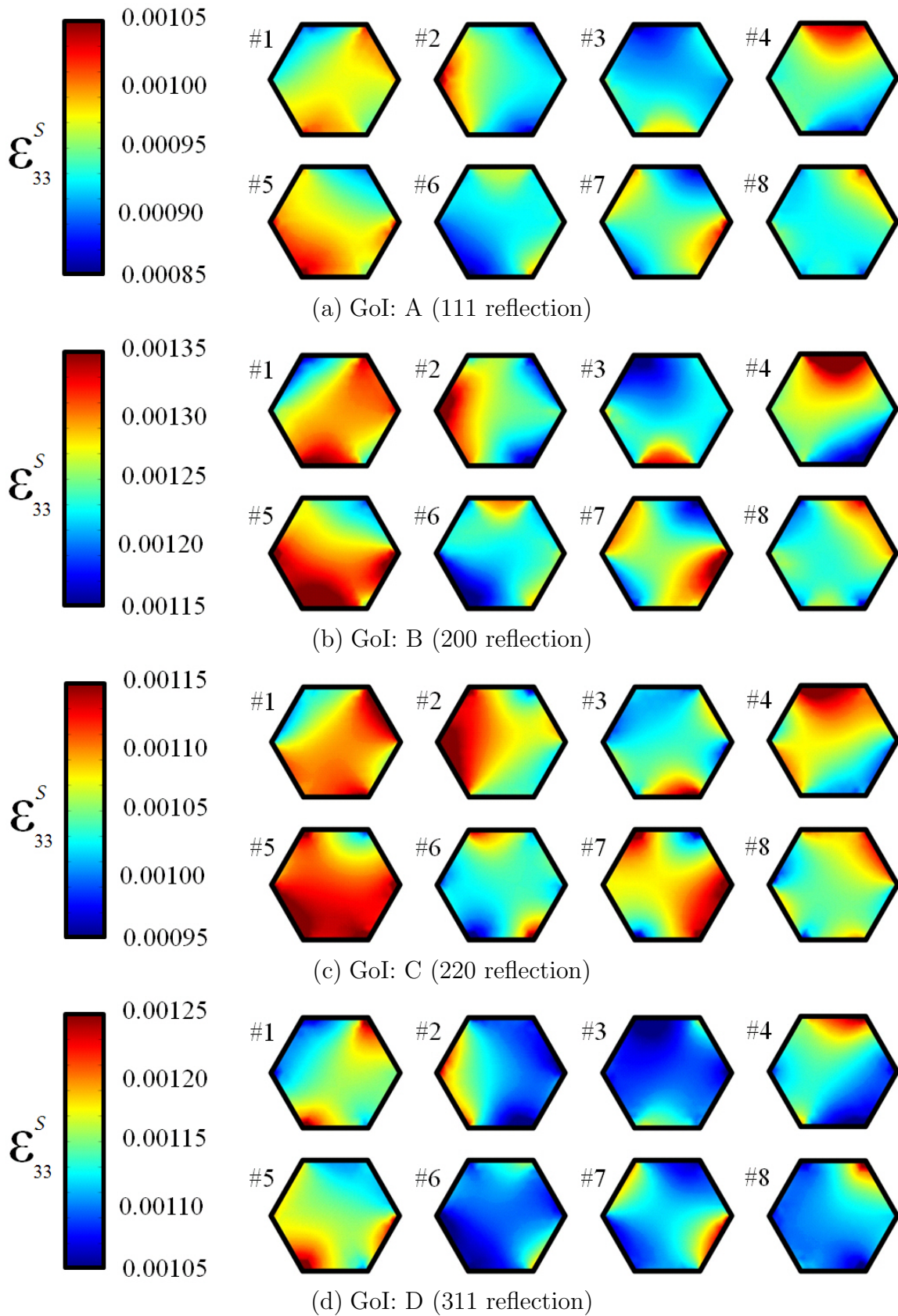


Figure 2.19: Contour plots depicting the variation within the GoI of the  $\epsilon_{33}^S$  (i.e.  $\epsilon_{33}^L(\text{HKL}, \phi, \psi, \chi)$  at  $\phi = 0^\circ$ ,  $\psi = 0^\circ$  and for  $\chi = 0^\circ$ ) strain component for uniaxial (vertical) compressive loading of  $\sigma_{11} = -100$  MPa (as indicated in Figure 2.17; see also text) for four orientations of the GoI (A: 111; B: 200; C: 220; D: 311) and for the eight different surroundings of the GoI. Color scale for each GoI differs in order to best represent the intragranular strain variation. Numerical results have been gathered in Table 2.3.

## 2.6 General discussion

The classical grain-interaction models were conceived to calculate the mechanical, elastic constants for materials. They have also been applied in order to describe the diffraction elastic constants and stress factors for calculating stress from lattice-strain measurements by (x-ray) diffraction analysis. Such models have successfully predicted the dependence of the average lattice strain on the direction of the diffraction vector in polycrystalline aggregates under elastic loading. Therefore, it is only natural to apply such models for predicting the strain variation and thus the diffraction-line broadening. This work has shown that the grain-interaction models can only account for a part of the strain-variation induced broadening of diffraction lines.

Table 2.4: Comparison of strain variation contributions induced by uniaxial elastic loading for an untextured polycrystalline Au aggregate.

Strain variation	Magnitude of variation	Notes
Mesovariation by variable $\chi$	$ \Delta\epsilon_{33}^{\mathcal{L}}{}_{\phi,\psi}{}^{\text{HKL}}(\chi) : \sim 0.0008$ ( <i>grain-interaction models</i> )	Magnitude is dependent on grain-interaction model, texture, and diffraction geometry (HKL, $\psi$ , and $\phi$ )
Mesovariation at constant $\chi$	$ \Delta\epsilon_{33}^{\mathcal{S}} : \sim 0.0001$ ( <i>FEA</i> )	Statistical variation of average strain for GoI at fixed $\chi$ in the various <i>locally heterogeneous aggregate</i> configurations according to FEA
Microvariation	$ \Delta\epsilon_{33}^{\mathcal{S}} : \sim 0.0005$ ( <i>FEA</i> )	Strain variation within GoI according to FEA

On the basis of the present model calculations (i.e. both the grain-interaction models and the FEA), the relative magnitudes of the contributions of (i) mesovariation of lattice strain by variation of  $\chi$  (i.e.  $|\Delta\epsilon_{33}^{\mathcal{L}}{}_{\phi,\psi}{}^{\text{HKL}}(\chi)|$  as predicted by the grain-interaction models), (ii) mesovariation of lattice strain at constant  $\chi$  (i.e.  $\epsilon_{33}^{\mathcal{S}}$  at constant  $\chi$  for the various, different surroundings for the same GoI, as predicted by the FEA calculations) and (iii) microvariation of lattice strain, to the elastic loading-induced diffraction-line broadening, can be assessed and compared. Such results for an untextured Au aggregate under uniaxial compressive loading ( $\sigma_{11} = -100$  MPa; Figure 2.17) are provided by Table 2.4 and Figure 2.19. Evidently, all of these contributions to strain variation are expressed simultaneously in the experimentally observed diffraction-line broadening. Therefore, according to these calculations, the diffraction-line broadening observed in reality can be 50% larger than predicted by the grain-interaction models. In particular, also for the  $H00$  and  $HHH$  reflections of (loaded) cubic materials, the occurrence of a strain variation, and thus diffraction-line broadening, is predicted by the anisotropic grain-interaction models and by FEA, in contrast with the classical isotropic grain-interaction models. Hence, diffraction-line broadening is also expected for these reflections.

## 2.7 Conclusions

In this work, three categories of strain variation present in an elastically loaded polycrystalline aggregate have been recognized:

- (i) *Macrovariation* in strain is the variation of the average lattice strain, taken for the groups of diffracting grains, that occurs upon changing the orientation of the diffraction vector with respect to the specimen frame of reference.
- (ii) *Mesovariation* in strain is the variation of the average lattice strain, the average now taken per diffracting grain, for the group of diffracting grains sharing a fixed orientation of the diffraction vector.
- (iii) *Microvariation* in strain is the variation of lattice strain within an individual grain.

- Both mesovariation and microvariation of strain will contribute to diffraction-line broadening induced by elastic loading. Grain-interaction models, as presented in the literature, are applied to calculate the strain distribution in a polycrystalline aggregate as a function of grain orientation with respect to the body. Such models can lead to reliable estimates for predicting the average lattice strain in polycrystalline aggregates under elastic loading, as determined from the position of diffraction lines. However, these grain-interaction models do not provide realistic estimates for the lattice-strain variation as expressed in the observed diffraction-line broadening: this broadening can be underestimated to the order of 50%.
- Not all sources of strain variation are captured by the grain-interaction models (see above). In particular: (i) the variation of average strain of each diffraction grain due to different surroundings of each of the diffracting grains (at fixed orientation of the diffraction vector) and (ii) the strain variation within each diffracting grain are not considered in the grain-interaction models.
- FEA calculations do provide estimates for all contributions to the lattice-strain variation.
- It has been claimed that  $H00$  and  $HHH$  reflections do not exhibit broadening in the case of loading cubic materials. However, this results only holds if an isotropic grain-interaction model is applied. In general, as shown for the anisotropic grain-interaction models and the FEA calculations, also the  $H00$  and  $HHH$  reflections of cubic materials exhibit broadening.
- Texture within a polycrystalline aggregate reduces (i) the overall diffraction-line broadening induced by elastic loading (because many of the grains are aligned along a preferred direction) and (ii) has a lesser influence on line broadening if anisotropic (as compared to isotropic) grain interaction occurs.

- The strain variation  $\epsilon_{33}^{\mathcal{L}}{}_{\phi,\psi}^{\text{HKL}}(\chi)$  is nil, when the diffraction vector is aligned with the loading axis of symmetry for a given state of stress, if the grain interaction is isotropic.
- Only the magnitude of the stress and the type of stress state influence the strain variation in the polycrystalline body; the character of the loading (tensile versus compressive loading) does not play a role.
- Analysis of lattice-strain induced diffraction-line broadening can provide much more direct and detailed information on the type of operating grain interactions than as obtained from “standard” diffraction stress analysis on the basis of diffraction-line positions, e.g. by the so-called  $\sin^2 \psi$ -method.



## 2.8 Appendix: Definition of grain orientation for FEA calculations

The single-crystal elastic constants used to define the material in the FEA simulation as gold are  $C_{11} = 186$  GPa,  $C_{12} = 157$  GPa,  $C_{44} = 42$  GPa [43]. The color of each grain in Figure 2.18 corresponds to its orientation in the specimen frame of reference. This orientation is defined by the Euler angles  $\alpha$ ,  $\beta$ , and  $\gamma$  (given in Table 2.5) according to the Bunge convention [26,27]. These angles define the three rotations with respect to the specimen ( $\mathcal{S}$ ) frame of reference to transform it into the crystallite ( $\mathcal{C}$ ) frame of reference, as shown in steps in Figure 2.20, where the  $e_i$  system of coordinates is the  $\mathcal{S}$  frame of reference and the  $e_i'''$  system of coordinates is the  $\mathcal{C}$  frame of reference.

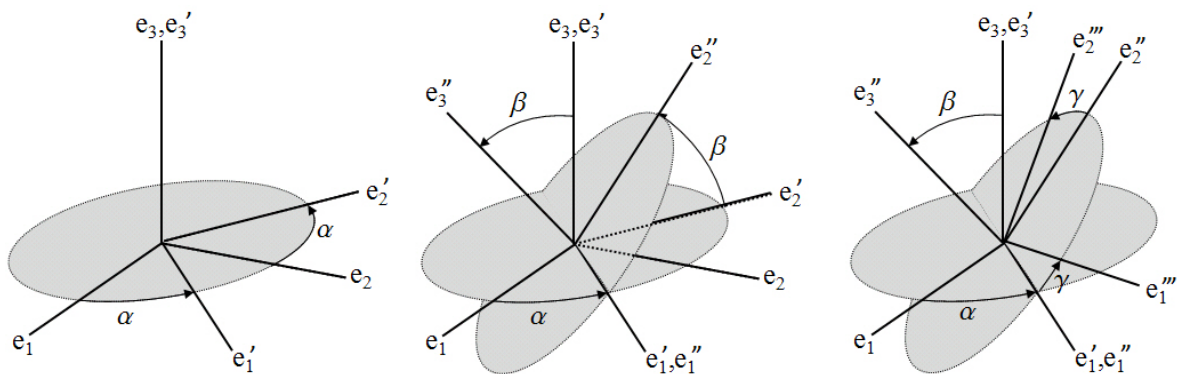


Figure 2.20: Transformation from the specimen frame of reference ( $\mathcal{S}$ ) to the crystal frame of reference ( $\mathcal{C}$ ) defined with respect to the specimen frame ( $\mathcal{S}$ ) by the Bunge Euler angles  $\alpha$ ,  $\beta$ , and  $\gamma$ ; refer to [26,27].

Table 2.5: Bunge convention Euler angles to define grain orientation in FEA calculations; see section 2.3.1 and refer to [26,27]; see Figure 2.18.

Grain Color	$\alpha$	$\beta$	$\gamma$
Dark blue	$42^\circ$	$-31^\circ$	$45^\circ$
Light brown	$-48^\circ$	$58^\circ$	$-55^\circ$
Pink	$51^\circ$	$-44^\circ$	$68^\circ$
Light purple	$21^\circ$	$74^\circ$	$6^\circ$
Dark green	$-61^\circ$	$12^\circ$	$-62^\circ$
Light orange	$16^\circ$	$-75^\circ$	$-16^\circ$
GoI			
A : 111	$18^\circ$	$54.74^\circ$	$45^\circ$
B : 200	$-84^\circ$	$0^\circ$	$0^\circ$
C : 220	$54^\circ$	$45^\circ$	$0^\circ$
D : 311	$-14^\circ$	$25.24^\circ$	$45^\circ$

# Bibliography

- [1] U. Welzel and E. J. Mittemeijer, “Diffraction stress analysis of macroscopically elastically anisotropic specimens: On the concepts of diffraction elastic constants and stress factors,” *Journal of Applied Physics*, vol. 93, no. 11, pp. 9001–9011, 2003.
- [2] U. Welzel, J. Ligot, P. Lamparter, A. C. Vermeulen, and E. J. Mittemeijer, “Stress analysis of polycrystalline thin films and surface regions by X-ray diffraction,” *Journal of Applied Crystallography*, vol. 38, pp. 1–29, 2005.
- [3] U. F. Kocks, C. N. Tomé, and H.-R. Wenk, *Texture and Anisotropy*. New York, NY: Cambridge University Press, 4th ed., 1998.
- [4] C. M. Brakman, T. H. de Keijser, N. M. van der Pers, P. Penning, and S. Radelaar, “Diffraction elastic constants for the determination of stresses in texture cubic materials: an experimental test,” *Philosophical Magazine A*, vol. 53, no. 4, pp. 635–650, 1988.
- [5] W. Voigt, *Lehrbuch der Kristallphysik*. Teuber, Leipzig-Berlin, 1910.
- [6] A. Reuss, “Account of the liquid limit of mixed crystals on the basis of the plasticity condition for single crystal,” *Zeitschrift für Angewandte Mathematik und Mechanik*, vol. 9, pp. 49–58, 1929.
- [7] H. Neerfeld, “Zur Spannungsberechnung aus röntgenographischen Dehnungsmessungen,” *Mitteilung Kaiser-Wilhelm-Institut-Eisenforschung*, vol. 24, pp. 61–70, 1942.
- [8] R. Hill, “The elastic behaviour of a crystalline aggregate,” *Proceedings of the Physical Society A*, vol. 65, no. 389, pp. 349–355, 1952.
- [9] J. D. Eshelby, “The determination of the elastic field of an ellipsoidal inclusion, and related problems,” *Proceedings of the Royal Society A*, vol. 241, no. 1226, pp. 379–396, 1957.
- [10] E. Kröner, “Berechnung der elastischen konstanten des vielkristalls aus den konstanten des einkristalls,” *Zeitschrift für Physik*, vol. 151, no. 4, pp. 504–518, 1958.
- [11] N. Koch, U. Welzel, H. Wern, and E. J. Mittemeijer, “Mechanical elastic constants and diffraction stress factors of macroscopically elastically anisotropic polycrystals:

- the effect of grain-shape (morphological) texture,” *Philosophical Magazine*, vol. 84, no. 33, pp. 3547–3570, 2004.
- [12] R. W. Vook and F. Witt, “Thermally induced strains in evaporated films,” *Journal of Applied Physics*, vol. 36, no. 7, pp. 2169–2171, 1965.
- [13] F. Witt and R. W. Vook, “Thermally induced strains in cubic metal films,” *Journal of Applied Physics*, vol. 39, no. 6, pp. 2773–2776, 1968.
- [14] U. Welzel, M. Leoni, and E. J. Mittemeijer, “The determination of stresses in thin films; modelling elastic grain interaction,” *Philosophical Magazine*, vol. 83, no. 5, pp. 603–630, 2003.
- [15] V. Hauk, *Structural and Residual Stress Analysis by Nondestructive Methods*. Elsevier, 1997.
- [16] C. M. Sayers, “The strain distribution in anisotropic polycrystalline aggregates subjected to an external stress field,” *Philosophical Magazine A*, vol. 49, no. 2, pp. 243–262, 1984.
- [17] E. J. Mittemeijer and U. Welzel, “The state of the art of the diffraction analysis of crystallite size and lattice strain,” *Zeitschrift für Kristallographie*, vol. 223, no. 9, pp. 552–560, 2008.
- [18] E. J. Mittemeijer and P. Scardi, eds., *Diffraction Analysis of the Microstructure of Materials*. Springer, 2004.
- [19] T. Uchida, N. Funamori, and T. Yagi, “Lattice strains in crystals under uniaxial stress field,” *Journal of Applied Physics*, vol. 80, no. 2, pp. 739–746, 1996.
- [20] J. F. Nye, *Physical Properties of Crystals*. Oxford University Press, 1957.
- [21] N. Funamori, M. Funamori, R. Jeanloz, and N. Hamaya, “Broadening of X-ray powder diffraction lines under nonhydrostatic stress,” *Journal of Applied Physics*, vol. 82, no. 1, pp. 142–146, 1997.
- [22] A. K. Singh and C. Balasingh, “X-ray diffraction line broadening under elastic deformation of polycrystalline sample: An elastic-anisotropy effect,” *Journal of Applied Physics*, vol. 90, no. 5, pp. 2296–2302, 2001.
- [23] M. van Leeuwen, J.-D. Kamminga, and E. J. Mittemeijer, “Diffraction stress analysis of thin films: Modeling and experimental evaluation of elastic constants and grain interaction,” *Journal of Applied Physics*, vol. 86, no. 1904, pp. 1904–1914, 1999.
- [24] C. Giacovazzo, H. L. Monaco, G. Artioli, D. Viterbo, G. Ferraris, G. Gilli, G. Zanotti, and M. Catti, *Fundamentals of Crystallography*. Oxford University Press, 2nd edition, ed., 2002.

- [25] R.-J. Roe and W. R. Krigbaum, "Description of crystallite ordination in polycrystalline materials having fiber texture," *Journal of Chemical Physics*, vol. 40, no. 9, pp. 2608–2615, 1964.
- [26] H. J. Bunge, "Zur Darstellung allgemeiner Texturen," *Zeitschrift für Metallkunde*, vol. 56, no. 12, p. 872, 1965.
- [27] H. J. Bunge and W. T. Roberts, "Orientation Distribution, Elastic and Plastic Anisotropy in Stabilized Steel Sheet," *Journal of Applied Crystallography*, vol. 2, pp. 116–128, 1969.
- [28] H.-J. Bunge, *Texture Analysis in Material Science*. Butterworth, 1982.
- [29] H. E. Swanson, *United States National Bureau of Standards*. Washington, D.C.: U.S. Department of Commerce., 1953.
- [30] B. E. Warren, *X-ray Diffraction*. Dover Publications, 1969.
- [31] E. J. Sonneveld, R. Delhez, T. H. de Keijser, and E. J. Mittemeijer, "Quality of unravelling of experimental diffraction patterns with artificially varied overlap," *Materials Science Forum*, vol. 79–82, pp. 85–90, 1991.
- [32] A. R. Stokes and A. J. C. Wilson, "The diffraction of x-rays by distorted crystal aggregates," *Proceedings of the Physical Society A*, vol. 56, pp. 174–181, 1944.
- [33] A. J. C. Wilson, "On variance as a measure of line broadening in diffractometry general theory and small particle size," *Proceedings of the Physical Society A*, vol. 80, no. 513, pp. 286–294, 1962.
- [34] A. J. C. Wilson, "On variance as a measure of line broadening in diffractometry .2. mistakes and strain," *Proceedings of the Physical Society A*, vol. 81, no. 519, pp. 41–46, 1963.
- [35] A. Leineweber and E. J. Mittemeijer, "Notes on the order-of-reflection dependence of microstrain broadening," *Journal of Applied Crystallography*, vol. 43, pp. 981–989, 2010.
- [36] U. Welzel, S. Fréour, and E. J. Mittemeijer, "Direction-dependent elastic grain-interaction models - a comparative study," *Philosophical Magazine*, vol. 85, no. 21, pp. 2391–2414, 2005.
- [37] U. Welzel, A. Kumar, and E. J. Mittemeijer, "Extremely anisotropic, direction-dependent elastic grain interaction: The case of ultrathin films," *Applied Physics Letters*, vol. 95, no. 11, p. 111907, 2009.
- [38] N. Tamura, A. A. MacDowell, R. Spolenak, B. C. Valek, J. C. Bravman, W. L. Brown, R. S. Celestre, H. A. Padmore, B. W. Batterman, and J. R. Patel, "Scanning X-ray microdiffraction with submicrometer white beam for strain/stress and orientation

- mapping in thin films,” *Journal of Synchrotron Radiation*, vol. 10, no. 2, pp. 137–143, 2003.
- [39] E. J. Mittemeijer, *Fundamentals of Materials Science*. Springer, 2011.
- [40] P. C. Chou and N. J. Pagano, *Elasticity: Tensor, Dyadic, and Engineering Approaches*. Dover Publications, 1992.
- [41] P. L. Gould, *Introduction to Linear Elasticity*. Springer-Verlag, 1983.
- [42] S. P. Timoshenko and J. N. Goodier, *Theory of Elasticity*. McGraw-Hill, 3rd ed., 1982.
- [43] C. J. Smithells and E. A. Brandes, *Metals Reference Book*. Butterworths, 5th edition ed., 1976.



## Chapter 3

# Measurement of x-ray diffraction-line broadening induced by elastic mechanical grain interaction

M. K. A. Koker, U. Welzel, and E. J. Mittemeijer

### Abstract

Various grain-interaction models have been proposed in the literature to describe the stress and strain behavior of individual grains within a massive aggregate. Diffraction lines exhibit a response to the occurrence of a strain distribution in the diffracting crystallites, selected by the direction of the diffraction vector with respect to the specimen frame of reference, by correspondingly induced diffraction-line broadening. This work provides a report of synchrotron diffraction investigations dedicated to the measurement of the experimentally observable diffraction-line broadening induced by external elastic loading of various polycrystalline specimens. The experimentally obtained broadening data have been compared with those calculated adopting various grain-interaction models. Although such grain-interaction models have been proven to accurately predict the average (x-ray) diffraction measured lattice strain, as derived from the diffraction-peak position, the present results have demonstrated that the extent of the diffraction-line broadening due to grain interactions, as calculated by employing these grain-interaction models, is much smaller than the experimentally determined broadening. The obtained results have vast implication for diffraction-line broadening analysis and the understanding of the elastic behavior of massive polycrystals.

## 3.1 Introduction

The use of diffraction techniques to study lattice strain is not a new strategy (e.g. see [1] and references therein). Elastic loading of a polycrystal results in a strain distribution within the material. The elastically intrinsically anisotropic grains in a massive body cannot deform freely to comply with an imposed state of mechanical stress; instead they must adapt their mechanical response to their surroundings. A wide range of elastic grain-interaction models have been developed to understand the strain within the individual crystals of a massive polycrystalline specimen subjected to an external load [2–12]. These models differ not only in their complexity (Reuss and Voigt models can often be solved analytically, whereas already the Eshelby-Kröner model can be solved only numerically), but also in their boundary conditions (anisotropic models, such as the Vook-Witt and inverse Vook-Witt models [11], have been found to be valid in predicting the measured strain in thin films under loading, whereas the classical, isotropic Neerfeld-Hill model appears appropriate especially for bulk material with spherical, or equiaxed, grains in the specimen). The more complex the model, the more versatily applicable it may be. The Eshelby-Kröner model [6, 7], for example, can incorporate morphological (grain shape [13]) texture and crystallographic (orientation-distribution function) texture.

The elastic grain-interaction models, as listed above, have been applied to calculate the macroscopic elastic constants of a material or to predict the average lattice strain as measured along the diffraction vector  $\{\epsilon_{33}^{\mathcal{L}}\}_{\phi, \psi}^{\text{HKL}}$  (see Section 3.2) in an x-ray diffraction (XRD) experiment. Although not generally recognized, these models can also be used to calculate the strain variation within an aggregate under loading, for the *diffracting* crystallites, which strain variation results in diffraction-line broadening [14–17].

Diffraction-line broadening is induced when grains with  $hkl$  planes sharing the same normal (parallel to the diffraction vector, as indicated in Figure 3.1) experience different (average) strains in the direction of the diffraction vector due to their intrinsically anisotropic elastic behavior. The average strain of a crystallite as a function of its orientation with respect to the specimen frame of reference can be determined according to elastic grain-interaction models [14, 17]. On this basis, the variation of this (average) strain as a function of the angle of rotation,  $\chi$ , about the diffraction vector  $\epsilon_{\phi, \psi}^{\text{HKL}}(\chi)$  (see Section 3.2), can be calculated for a fixed diffraction geometry (i.e. fixed HKL,  $\psi$ ,  $\phi$ ).

Broadening contributions, such as instrumental and finite grain size, remain unchanged during elastic loading and unloading experiments. Such sources of broadening are not considered in this work. Here the focus of the attention is on the measurement of elastic loading-induced (reversible) diffraction-line broadening. This is a rather unexplored area (exceptions are the experimental observations reported in [15] and [16]) which is at least partly due to the high resolution necessary to measure such a phenomenon. (First, theoretical calculations of elastic loading-induced diffraction-line broadening have been performed by [14] and [17].)



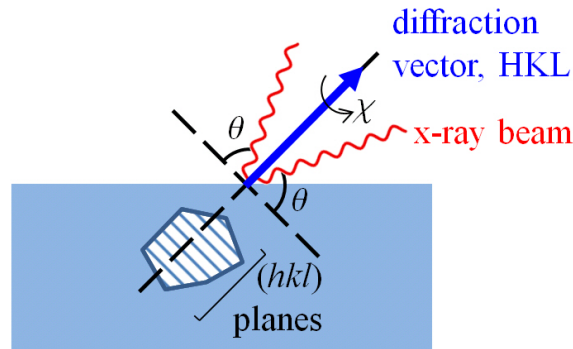


Figure 3.1: Schematic to demonstrate the degree of grain rotational freedom, in a diffraction experiment, given as the angle  $\chi$ , defining the rotation about the  $HKL$  diffraction vector, which is perpendicular to a set of  $(hkl)$  planes.

The work presented here consists of diffraction-line broadening measurements, on polycrystalline specimens of four different metals (Cu, Ni, Nb, W) under two different imposed states of stress (uniaxial and biaxially rotationally symmetric), made using synchrotron radiation. It will be shown that sources of strain variation by elastic grain interactions *not* captured by the known elastic grain-interaction models bring about a substantial part of the observed diffraction-line broadening.

## 3.2 Theoretical background

### 3.2.1 Reference frames and calculations of diffraction averages

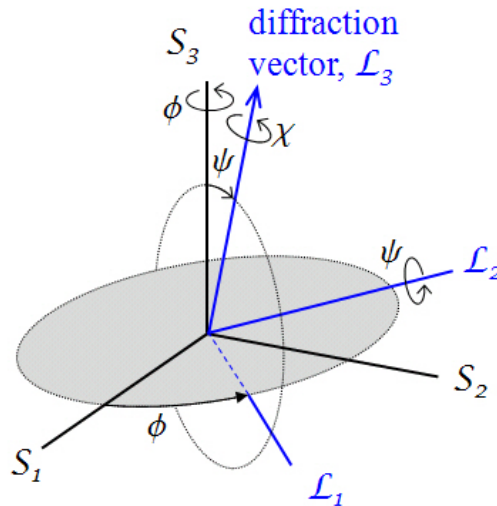
Three Cartesian frames of reference, as shown in Figure 3.2, are defined:

- The *crystal frame of reference* ( $\mathcal{C}$ ): The conventional definition of an orthonormal crystal system, such as the one given in [18] is adopted. A detailed treatment can be found in [19]. For cubic crystal symmetry, the axes chosen coincide with the  $a$ ,  $b$ , and  $c$  axes of the crystal lattice.
- The *specimen frame of reference* ( $\mathcal{S}$ ): The  $\mathcal{S}_3$  axis is orientated perpendicular to the specimen surface, and the  $\mathcal{S}_1$  and  $\mathcal{S}_2$  axes are in the surface plane.
- The *laboratory frame of reference* ( $\mathcal{L}$ ): This frame is chosen in such a way that the  $\mathcal{L}_3$  axis coincides with the diffraction vector in the (x-ray) diffraction (XRD) experiment.

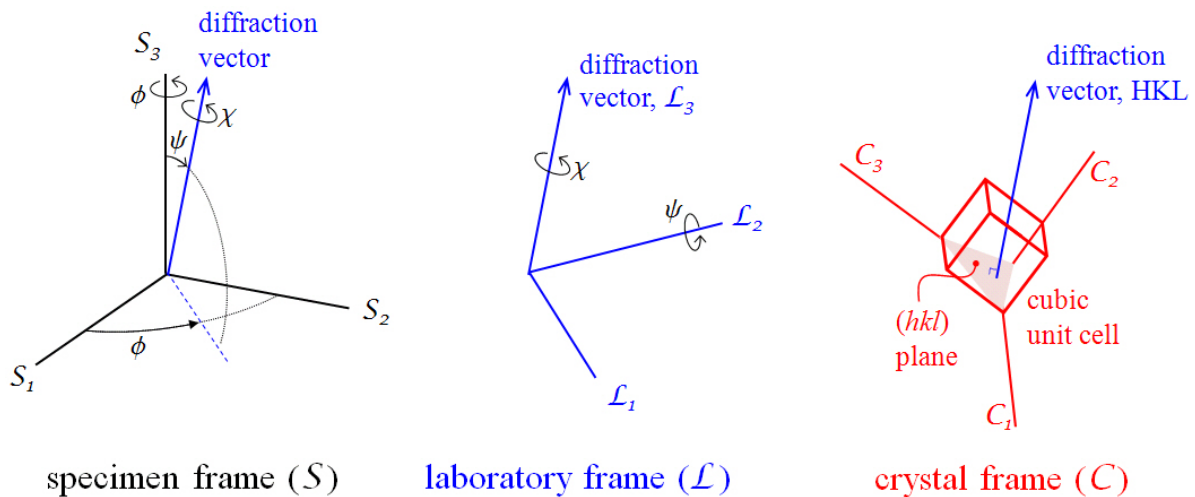
The relative orientation of the laboratory frame of reference with respect to the specimen frame of reference is specified by the angles  $\phi$  and  $\psi$ , where  $\psi$  is the inclination angle of the sample surface normal (i.e. the  $\mathcal{S}_3$  axis) with respect to the diffraction vector (i.e. the  $\mathcal{L}_3$  axis) and  $\phi$  denotes the rotation of the sample around the sample surface normal. The angle  $\chi$  is defined as a rotation of the laboratory frame of reference about the  $\mathcal{L}_3$  axis (the diffraction vector), where, for  $\phi = \psi = \chi = 0^\circ$ , the  $\mathcal{L}$  frame of reference coin-

cides with the  $\mathcal{S}$  frame of reference. The direction of the diffraction vector is especially important in XRD experiments as this is the direction along which lattice spacing (and thus average lattice strain) is measured.

In the following, a superscript ( $\mathcal{C}$ ,  $\mathcal{S}$ , or  $\mathcal{L}$ ) is used for indicating the reference frame adopted for the representation of quantities which are orientation specific.



(a) Laboratory frame ( $\mathcal{L}$ ) defined with respect to the specimen frame ( $\mathcal{S}$ ) by the diffraction angles  $\phi$ ,  $\psi$ , and  $\chi$



specimen frame ( $\mathcal{S}$ )      laboratory frame ( $\mathcal{L}$ )      crystal frame ( $\mathcal{C}$ )  
 (b) Orientation of reference frames defined by the orientation of the diffraction vector (for a fixed HKL,  $\phi$ ,  $\psi$ , and  $\chi$ )

Figure 3.2: Introduction of the three standard coordinate systems and the corresponding orientation angles necessary for the discussion of diffraction experiments.

The orientation of each crystallite in the  $\mathcal{S}$  system can be identified by three Euler angles, according to Bunge convention [20, 21]. These angles will be called  $\alpha$ ,  $\beta$ , and  $\gamma$  [22]. See, for example, [17] for a more in-depth discussion. It is usual to associate a set

of Euler angles with a vector  $\mathbf{g} = (\alpha, \beta, \gamma)$  in the three-dimensional orientation (Euler) space  $G$  [23]. In this way, each point in the orientation space  $G$  represents a possible orientation of the  $\mathcal{C}$  frame of reference with respect to the  $\mathcal{S}$  frame of reference. Texture can be quantified by introducing the orientation distribution function (ODF),  $\mathcal{F}(\alpha, \beta, \gamma)$ , which is a function of the Euler angles, specifying the volume fraction of crystallites having an orientation in the infinitesimal orientation range  $d^3\mathbf{g} = \sin(\beta)d\alpha d\beta d\gamma$  around  $\mathbf{g}$ .

In the context of diffraction analysis, the analyzed volume is generally only a fraction of the volume of the polycrystalline specimen: braces  $\{\dots\}$  denote volume-weighted averages for diffracting crystallites only (i.e. diffraction averages). A diffraction line contains data on only a subset of the crystallites for which the diffraction planes are perpendicular to the chosen measurement direction. Because only the measurement direction (i.e. the direction of the diffraction vector) is defined, a degree of freedom occurs for the diffracting crystallites: the rotation about the diffraction vector (denoted by the angle  $\chi$ ). For a single HKL diffraction line, the group of diffracting crystallites is selected by specifying the HKL of the reflection and the orientation of the diffraction vector with respect to the specimen reference frame  $\mathcal{S}$ , which can be identified by the angles  $(\phi, \psi)$ . Therefore the sub-  $(\phi, \psi)$  and superscripts (HKL) are attached to the corresponding average of a strain tensor (element).

For a fixed diffraction vector (i.e. HKL,  $\phi$ , and  $\psi$  have been specified), the average lattice strain  $\epsilon_{\phi, \psi}^{\text{HKL}} = \{\epsilon_{33}^{\mathcal{L}}\}_{\phi, \psi}^{\text{HKL}}$  and the lattice strain distribution  $\epsilon_{\phi, \psi}^{\text{HKL}}(\chi)$  (where the strain varies as a function of rotation  $\chi$  about the diffraction vector) are related according to:

$$\epsilon_{\phi, \psi}^{\text{HKL}} = \{\epsilon_{33}^{\mathcal{L}}\}_{\phi, \psi}^{\text{HKL}} = \frac{\int_0^{2\pi} \epsilon_{33}^{\mathcal{L}}(\text{HKL}, \chi, \phi, \psi) \mathcal{F}^*(\text{HKL}, \chi, \phi, \psi) d\chi}{\int_0^{2\pi} \mathcal{F}^*(\text{HKL}, \chi, \phi, \psi) d\chi}. \quad (3.1)$$

$\mathcal{F}^*(\text{HKL}, \chi, \phi, \psi) d\chi$  is the representation of the ODF in terms of the measurement parameters and the rotation angle  $\chi$ . The ODF is now expressed as  $\mathcal{F}^*(\text{HKL}, \chi, \phi, \psi) d\chi$ ;  $\mathcal{F}(\alpha, \beta, \gamma)$  cannot be directly used in Equation 3.1, since the angles  $\chi$ ,  $\phi$ , and  $\psi$  are *not* Euler angles representing a rotation of the  $\mathcal{C}$  system with respect to the  $\mathcal{S}$  system. (They actually provide the rotation of the system  $\mathcal{L}$  with respect to the system  $\mathcal{S}$ .) However, the values of  $\alpha$ ,  $\beta$ , and  $\gamma$ , and thus the  $\mathcal{F}(\alpha, \beta, \gamma)$  and thereby  $\mathcal{F}^*(\text{HKL}, \chi, \phi, \psi)$  at every  $\chi$  can be calculated from HKL,  $\chi$ ,  $\phi$ , and  $\psi$ . For a more detailed treatment, see Reference [24].

In order to compute the strain-broadened diffraction line, both the average lattice strain  $\epsilon_{\phi, \psi}^{\text{HKL}}$  (directly related to peak position upon loading) and the strain distribution  $\epsilon_{\phi, \psi}^{\text{HKL}}(\chi)$  ( $\epsilon_{33}^{\mathcal{L}}(\chi)$  at fixed HKL,  $\phi$ , and  $\psi$ ) are required. The strain distribution  $\epsilon_{\phi, \psi}^{\text{HKL}}(\chi)$  can be converted into a frequency function  $f(\epsilon)$  which describes the fraction of grains in the considered diffraction volume sharing the same diffraction vector and which experience the same (average) strain. Using Bragg's law (for a specified radiation wavelength and the material's strain-free lattice spacing  $d_o$  for the transition from  $\epsilon$  to  $d$ ), the frequency function  $f(\epsilon)$  can be converted to the  $2\theta$  scale. This transformation results in the *strain-induced broadening contribution function*  $f(2\theta)$ . The function  $f(2\theta)$ , when

convoluted with the diffraction profile corresponding to unloaded state  $g(2\theta)$ , yields the “measured” diffraction peak  $h(2\theta)$  for an elastically-loaded polycrystalline aggregate. It is important here to note that  $g(2\theta)$  incorporates all broadening contributions (such as grain size and instrumental broadening) other than that induced by the external mechanical loading. Upon unloading, the diffraction line  $h(2\theta)$  relaxes to  $g(2\theta)$ , as all broadening induced by elastic loading is fully reversible. For a more detailed discussion of such calculations, see Reference [17].

### 3.2.2 Lattice strain vs. mechanical stress relationships

Two states of stress in the specimen frame of reference are induced in this study by externally applied loading: biaxially rotationally symmetric and uniaxial. The general expression for the measurable average lattice strain along the diffraction vector obeys:

$$\epsilon_{\phi,\psi}^{\text{HKL}} = \{\epsilon_{33}^{\mathcal{L}}\}_{\phi,\psi}^{\text{HKL}} = F_{ij}^{\text{HKL}}(\phi, \psi) \cdot \langle \sigma_{ij}^{\mathcal{S}} \rangle. \quad (3.2)$$

where  $F_{ij}^{\text{HKL}}(\phi, \psi)$  are the diffraction (x-ray) stress factors and  $\langle \sigma_{ij}^{\mathcal{S}} \rangle$  describes the loading-induced state of mechanical stress in the specimen frame of reference. For proof, see [11]. The diffraction stress factors for a quasi-isotropic aggregate can be replaced by the diffraction elastic constants [11, 25]. Then, for the case of uniaxial (i.e.  $\langle \sigma_{ij}^{\mathcal{S}} \rangle = 0$  for all  $i, j$  except  $ij = 11$ ) and biaxially and rotationally symmetric ( $\langle \sigma_{11}^{\mathcal{S}} \rangle = \langle \sigma_{22}^{\mathcal{S}} \rangle \neq 0$ ;  $\langle \sigma_{ij}^{\mathcal{S}} \rangle = 0$ ,  $ij \neq 11 \neq 22$ ) stress states, and considering cubic crystal symmetry, Equation 3.2 simplifies to a linear relationship between the XRD measured average lattice strain  $\epsilon_{\phi,\psi}^{\text{HKL}}$  and  $\sin^2 \psi$ .

(i) Biaxially rotationally symmetric loading:

$$\epsilon_{\phi,\psi}^{\text{HKL}} = \frac{1}{2} \cdot S_2^{\text{HKL}} \sin^2 \psi \cdot \sigma_{\parallel} + 2 \cdot S_1^{\text{HKL}} \cdot \sigma_{\parallel}, \quad (3.3)$$

where  $S_1^{\text{HKL}}$  and  $\frac{1}{2}S_2^{\text{HKL}}$  are the (x-ray) diffraction elastic constants,  $\sigma_{\parallel}$  is the biaxially applied (and/or residual) stress ( $\sigma_{\parallel} = \langle \sigma_{11}^{\mathcal{S}} \rangle = \langle \sigma_{22}^{\mathcal{S}} \rangle$ ), and  $\psi$  is the specimen inclination or tilt angle. As this state of stress is rotationally symmetric,  $\epsilon_{\phi,\psi}^{\text{HKL}}$  is independent of rotation  $\phi$  about the specimen surface normal.

(ii) Uniaxial loading:

$$\epsilon_{\phi,\psi}^{\text{HKL}} = \frac{1}{2} \cdot S_2^{\text{HKL}} \cos^2 \phi \sin^2 \psi \cdot \sigma_{11} + S_1^{\text{HKL}} \cdot \sigma_{11}, \quad (3.4)$$

where  $\sigma_{11} = \langle \sigma_{11}^{\mathcal{S}} \rangle$  is the applied uniaxial load along the  $\mathcal{S}_1$  axis. This state of stress is not symmetric about the surface normal ( $\mathcal{S}_3$ ), and thus  $\epsilon_{\phi,\psi}^{\text{HKL}}$  depends on the angle of rotation  $\phi$  about the specimen normal.

### 3.2.3 Grain interaction and diffraction-line broadening

Grain-interaction models can be used to predict the elastic loading-induced average lattice strain of and the lattice-strain variation in polycrystalline aggregates [17]. The Reference [3] model (isotropic grain interaction), involving that all grains are in the same state of stress in the specimen frame of reference, overestimates the strain variation in the aggregate, and therefore supposedly provides a maximum value for the predicted diffraction-line broadening. The Reference [2] model (isotropic grain interaction), involving that all grains are in the same state of strain in the specimen frame of reference, implies the absence of strain variation in the aggregate and therefore would predict the absence of diffraction-line broadening. The (other) isotropic grain-interaction models Neerfeld-Hill [4, 5] and Eshelby-Kröner [6, 7] provide results which are more or less “averages” of the Voigt and Reuss extremes.

Grain interactions within an aggregate can also be anisotropic, implying different types and extents of grain interaction for directions parallel and perpendicular to the specimen surface. For example, the Vook-Witt grain-interaction model [8, 9] assumes that all grains are under the same stress perpendicular to the surface and experience identical strains parallel to the surface. The Eshelby-Kröner model has been shown to converge with the Vook-Witt model for needle-shaped grains ( $\eta \rightarrow \infty$ ) [26].

While none of these models showed an ideal match with the data presented in this work, the Reuss (isotropic) and Vook-Witt (anisotropic) models were used here, also recognizing their computational simplicity, for discussion of the observed diffraction-line broadenings. (For a comparison between the various grain-interaction models for predicting diffraction-line broadening, see Reference [17].)

Texture decreases the effect of lattice-strain variation by anisotropic grain interaction on the diffraction-line broadening [17]. Therefore, calculations for the effect of grain interactions on diffraction-line broadening for a statistically untextured aggregate result in an overestimate of the *expected* (grain-interaction induced) diffraction-line broadening.

In the presence of texture, the isotropic grain-interaction models (Voigt, Reuss, Neerfeld-Hill, and Eshelby-Kröner with  $\eta = 1$ ) for all  $H00$  and  $HHH$  reflections of cubic materials still lead to straight lines in plots of lattice strain versus  $\sin^2 \psi$ , and predict zero diffraction-line broadening. The anisotropic grain-interaction models do imply for (also textured), cubic materials that distinct broadening also occurs for the  $H00$  and  $HHH$  reflections [17]. This is an important result having direct relevance for the diffraction-line broadening observed in this work (Section 3.4).

## 3.3 Experimental procedures

Synchrotron X-ray diffraction stress measurements were conducted at the Max Planck Institute for Intelligent Systems (formerly Metals Research) “surface diffraction beam line” at ANKA, located at the Karlsruhe Institute of Technology (KIT), Germany. All of

the measurements discussed in this work were made using radiation with photon energy of 8.1 keV and a corresponding wavelength of  $\lambda = 1.52933 \text{ \AA}$ , with the exception of the measurements for the uniaxially loaded W dog-bone specimens, which were performed using an energy of 10 keV,  $\lambda = 1.2398 \text{ \AA}$ . Data were collected using a sodium iodine point detector preceded by a set of soller slits. The counting statistics were kept constant by monitoring the incoming beam current (as opposed to fixed time increments), since the electron-beam current decays as a function of time after each injection.

An overview of the performed experiments is provided by Table 3.1: materials, loading state, magnitude of loading, measured reflections. The measurable reflections and accessible tilt angles were dictated by the texture and/or the geometry of the loading device mounted on the Eulerian cradle. All diffraction lines discussed in this work were measured in reflection diffraction geometry.

Table 3.1: Materials used, applied states of stress, values of the applied principal stress components, and the diffraction lines recorded in the discussed experiments.

<b>Metal</b>	<b>Stress state</b>	<b>Applied stress</b>	<b>Measured diffraction lines</b>
Cu	biaxial	$\sigma_{\parallel} = 280 \text{ MPa}$	111, 200, 220, 311
Nb	biaxial	$-350 \text{ MPa}$	110, 200, 211, 220, 310
W	biaxial	$-1450 \text{ MPa}$	110, 200, 211, 220, 310, 321
Ni	uniaxial	$\sigma_{11} = 100 \text{ MPa}$	111, 200, 220, 311, 331
W	uniaxial	$145 \text{ MPa}$	200, 211, 220, 310

### 3.3.1 Loading set-up

#### 3.3.1.1 Biaxially rotationally symmetric loading

A heating/cooling chamber (MRI Physikalische Geräte GmbH, Karlsruhe, Germany) was used for *in situ* XRD measurements. Heating and cooling rates were regulated by the internal PID controller; measurements were made only at fixed temperatures, accurate within  $\pm 1^\circ\text{C}$ . Temperature variation within the chamber was found to be negligible by determining from measurements, at different locations at the surface of the film, the strain-free lattice parameter  $a_o$  [25], which depends strongly on temperature for the metals concerned.

Thin films of various metals were sputter-deposited on single-crystal substrates (see Section 3.3.2). Single crystals were chosen for the substrates so that elastic grain interactions in the substrate do not occur. The selected substrates have thermal expansion coefficients significantly different from those of the deposited metals. Heating or cooling of the layer/substrate system led to the development of a biaxial symmetric state of stress in the film and the substrate. As the (thick) substrate can be considered as rigid, the thermal misfit is fully accommodated by the metal films. Then the thermal misfit strain

in the film is given by:

$$\epsilon_{\parallel}(T) = [\alpha^{sub.}(T) - \alpha^{film}(T)] \cdot (T - T_{room}), \quad (3.5)$$

where  $\alpha(T)$  is the linear coefficient of thermal expansion which depends on temperature. Using the biaxial elastic modulus of the film  $M$ , the corresponding induced stress  $\sigma_{\parallel}(T)$  in the film can be calculated according to:

$$\sigma_{\parallel}(T) = M \cdot \epsilon_{\parallel}(T). \quad (3.6)$$

### 3.3.1.2 Uniaxial loading

So-called “dog-bone” specimens were uniaxially loaded through the use of a tensile machine (Kammrath & Weiss GmbH, Dortmund, Germany) mounted on an Eulerian cradle for *in situ* XRD measurements.

The applied load  $F$  and the cross-sectional area  $A$  in the middle of the dog-bone specimen can be used to calculate the applied stress  $\sigma_{11}(F)$  to the specimen,

$$\sigma_{11}(F) = \frac{F}{A}. \quad (3.7)$$

The corresponding strain can be found using Hooke’s Law and the elastic (Young’s) modulus  $E$  of the material. The strain rate was kept constant during loading and unloading of the specimens. During XRD measurements, the distance between the cross-heads was kept fixed, i.e. the material was not allowed to creep, and thereby, the strain was kept constant.

## 3.3.2 Materials

The intrinsic elastic anisotropy parameter  $\mathcal{A}$  (also known as the Zener’s anisotropy ratio) for a cubic material, follows from [18]:

$$\mathcal{A} = \frac{2(s_{11} - s_{12})}{s_{44}} = \frac{2 \cdot c_{44}}{c_{11} - c_{12}}, \quad (3.8)$$

where  $c_{ij}$  are the components of the single crystal elastic stiffness tensor and  $s_{ij}$  are the components of the single crystal elastic compliance tensor for the polycrystal.  $\mathcal{A} = 1$  represents isotropy, as practically holds for tungsten. The anisotropy parameters for the materials investigated in this work are presented in Table 3.2. (Gold has been included in this table, even though it is not experimentally investigated here, to facilitate comparison

Table 3.2: The elastic anisotropy parameter  $\mathcal{A}$  for cubic materials, as calculated using the components of the single crystal elastic stiffness tensor  $c_{ij}$ , according to Equation 3.8; elastic constants have been given in units of GPa [27]

Metal	Structure	$c_{11}$	$c_{12}$	$c_{44}$	$\mathcal{A}$
Copper, Cu	FCC	171.0	124.0	75.6	3.22
Gold, Au	FCC	186.0	157.0	42.0	2.90
Nickel, Ni	FCC	251.2	157.1	121.3	2.58
Niobium, Nb	BCC	192.0	134.0	56.8	1.96
Tungsten, W	BCC	501.0	198.0	151.0	1.00

with previous line-broadening studies [15, 17].)

### 3.3.2.1 Biaxially rotationally symmetric loaded specimens

#### Copper

Copper was sputter-deposited to a thickness of  $2 \mu\text{m}$  on a single-crystal silicon (100-orientation) wafer (deposition conditions:  $p_{\text{Ar}} = 3 \cdot 10^{-3}$  mbar,  $P_{\text{Cu}} = 200$  W). The conditions of deposition were tuned to produce little to no residual stress in the film at room temperature. The microstructure of the Cu (imaged with a focused ion beam, FIB) consists of many equiaxed grains, ranging in size from  $0.1$  to  $2.0 \mu\text{m}$ . The films possessed a 111-fiber texture (See the 111-pole figure section in Figure 3.3.)

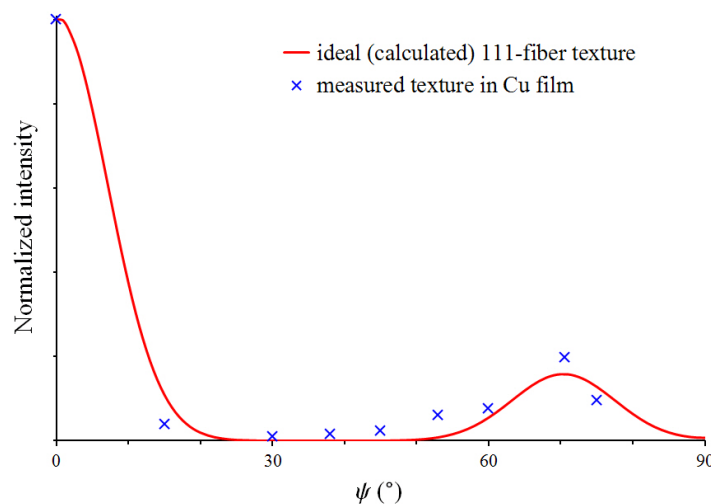


Figure 3.3: Experimentally measured and ideal rotationally symmetric (calculated) pole-figure sections for the 111 reflection for Cu (FCC) (111-fiber texture)

The film was loaded tensilely by cooling from room temperature ( $25^\circ\text{C}$ ) to a minimum temperature of  $-120^\circ\text{C}$ . This led to a biaxially rotationally symmetric state of stress with  $\sigma_{\parallel} \equiv \sigma_{11} = \sigma_{22}$  of approximately 280 MPa, as experimentally determined in this work. (Note the occurrence of material stiffening at low temperatures).



## Niobium

Niobium was sputter-deposited on an aluminum single-crystal substrate (100-orientation) to a thickness of  $2\ \mu\text{m}$  ( $p_{\text{Ar}} = 5.8 \cdot 10^{-3}$  mbar;  $P_{\text{Nb}} = 200$  W). After deposition, a tensile residual stress of  $\sigma_{\parallel} \equiv \sigma_{11} = \sigma_{22} = 350$  MPa was measured at room temperature. The film possessed a strong 110-fiber texture. The film was loaded compressively to achieve a state of zero stress by cooling to  $-120^{\circ}\text{C}$ . Therefore, the “unloaded” measurements were made in this cooled state; the “loaded” measurements were made at room temperature.

## Tungsten

The tungsten film was also sputter-deposited to a thickness of  $2\ \mu\text{m}$  onto an Al single-crystal (100-orientation) substrate ( $p_{\text{Ar}} = 5.8 \cdot 10^{-3}$  mbar;  $P_{\text{W}} = 200$  W). As with the Nb (also BCC), a 110-fiber texture was present in the film. The residual stress in the film at room temperature was  $\sigma_{\parallel} \equiv \sigma_{11} = \sigma_{22} = -1450$  MPa. Cooling to  $-120^{\circ}\text{C}$  led to a measured stress of  $\sigma_{\parallel} = -1260$  MPa, i.e. approximately 200 MPa of tensile stress was induced upon cooling.

### 3.3.2.2 Uniaxially loaded specimens

#### Nickel

Dog-bone specimens were made from 3.2 mm thick cold-rolled nickel sheet (purchased from *GoodFellow*, 99.99 at.% purity). The texture which had developed during rolling was neither sharp nor strong. The macroscopic (uniaxial) elastic limit of the Ni was measured to be approximately 125 MPa; therefore, the maximum *in situ* applied uniaxial elastic loading was  $\sigma_{11} = 100$  MPa.

#### Tungsten

Dog-bone specimens were made from 3 mm thick cold-rolled tungsten sheet (purchased from *GoodFellow*, 99.95 at.% purity). A weak rolling texture was prevalent in the material. The macroscopic (uniaxial) elastic limit was measured to be approximately 300 MPa. This loading limit was measured for the material which had a significant residual stress of -600 MPa (determined using XRD). The applied *in situ* uniaxial loading stress was limited to a maximum of  $\sigma_{11} = 150$  MPa.

### 3.3.3 Evaluation of diffraction data

Diffraction lines at multiple inclinations  $\psi$  at selected values of  $\phi$ , for a uniaxial state of applied stress and at  $\phi = 0^{\circ}$  for a biaxially rotationally symmetric state of stress, were

measured in the loaded and unloaded states for each of the discussed materials. (See Table 3.1.) A Pearson VII profile-shape function [28] was used to fit the peaks and thus to extract values for the parameters (i) diffraction-line position ( $2\theta$  position of the peak maximum) and (ii) integral breadth  $\beta$ , which is the ratio of the maximum peak intensity to the area under the peak. The integral breadth depends less on the precise shape of the peak than the full width at half maximum FWHM. Therefore, the integral breadth was adopted as the width parameter reflecting the magnitude of the lattice-strain variation in the specimen.

The loading-induced broadening of the diffraction line was defined as the difference in its integral breadth,  $\Delta\beta$ , of the loaded and unloaded states (see Figure 3.4):

$$\Delta\beta = \beta^{\text{loaded}} - \beta^{\text{unloaded}}. \quad (3.9)$$

In the following, the average lattice strain  $\{\epsilon_{33}^{\mathcal{L}}\}_{\phi,\psi}^{\text{HKL}}$ , the integral breadth  $\beta$ , and the loading-induced broadening  $\Delta\beta$  have all been plotted as a function of  $\sin^2\psi$ . If no error bars have been indicated on a plot, then they are of the order of the symbol size.

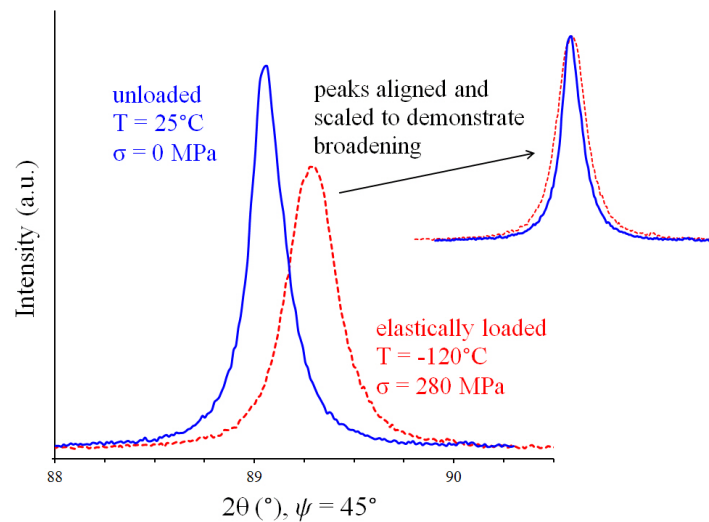


Figure 3.4: The loading induced (peak shift and) broadening of the 311 reflection recorded for a Cu thin film (at tilt angle of  $\psi = 45^\circ$ ; radiation  $\lambda = 1.52933 \text{ \AA}$ ). The state of biaxially rotationally symmetric tensile stress (280 MPa) was imposed by cooling to  $-120^\circ\text{C}$ . The inset reveals the difference in broadening for loaded and unloaded states by scaling and shifting the peak maximum positions, such that the peak maxima coincide.

## 3.4 Results and discussion

XRD measurements were made of multiple HKL diffraction lines for the pure metal specimens (films and dog-bone specimens, as introduced in Section 3.3.2) in the loaded and unloaded states. Each specimen was measured before application of the load and after removal of the load to ensure that the applied deformation by loading of the specimen

was purely elastic: it was verified that peak position and peak width returned to their original state upon unloading. As an example, the average lattice strain  $\epsilon_{\phi,\psi}^{\text{HKL}}$  and the integral breadth  $\beta$ , as derived from the diffraction lines measured for a 111-fiber textured Cu thin film, are shown in Figures 3.5 and 3.6, respectively. Similar measured diffraction-line broadening results (for  $\Delta\beta$ , Equation 3.9) have been obtained for all five specimens (Table 3.1) and have been plotted in Figures 3.7-3.9.

Previously, it was thought that  $H00$  and  $HHH$  reflections would not broaden upon elastic loading as the the diffraction lattice planes are structurally (and therefore elastically) symmetric with respect to the diffraction vector [14–16]. Thus, the *isotropic* grain-interaction models predict that no strain distribution will be induced for  $H00$  and  $HHH$  reflections. However, the *local inhomogeneity* of the matrix (i.e. the different surroundings for each diffracting grain) will induce a different loading for each of the diffracting grains (also for the  $H00$  and  $HHH$  reflections). Already, the *anisotropic* grain-interaction models (while still neglecting the effect of the different surroundings for the diffraction grains) do predict a loading-induced diffraction-line broadening for also the  $H00$  and  $HHH$  reflections from cubic materials. For example, see results for the Vook-Witt grain-interaction model (open diamonds) in Figure 3.7.

As the Ni bulk material is significantly less textured than the Cu and Nb films, it is therefore prone to additional diffraction-line broadening as a consequence of the local heterogeneity within the aggregate, i.e. the different surrounding for each diffracting grain (much more so than the Cu and Nb films, as was discussed in Section 3.2.3).

For the same loading axes and the same magnitude of load, a tensile or a compressive nature of the load has no effect on the lattice-strain variation  $\epsilon_{\phi,\psi}^{\text{HKL}}(\chi)$ , independent of the type of state of stress [17].

Generally, the integral breadth of the only strain broadened profile is proportional with the square root of the strain variance [29–32]. If the strain broadening is small as compared to the instrumental broadening, then, if a Gaussian-shape function is adopted for the instrumental and the only strain-broadened profiles, upon convolution, it follows that the additional broadening in the “loaded”  $h$  profile, as compared to the “unloaded”  $g$  profile (where  $h = g \otimes f$ ), roughly scales with the strain variance, which, in turn, scales with  $\sigma^2$ , with  $\sigma$  as the magnitude of the applied stress (see further below), for isotropic grain interaction [16]. However, if a Lorentzian (Cauchy) shape function is adopted for the instrumental and the only strain-broadened profiles, then the additional line broadening in the  $h$  profile, as compared to the  $g$  profile, would scale with the square root of the strain variance, and thus with  $\sigma$ . Indeed, it has often been suggested that a microstrain broadened line profile has a Gaussian shape (e.g. see Reference [32]), but this is not generally true and Lorentzian (Cauchy) shaped strain broadened line profiles have also been observed (e.g. see Reference [33]); for a rigorous discussion on (also line-profile shape of) micro-(lattice-)strain broadening, see Reference [34].

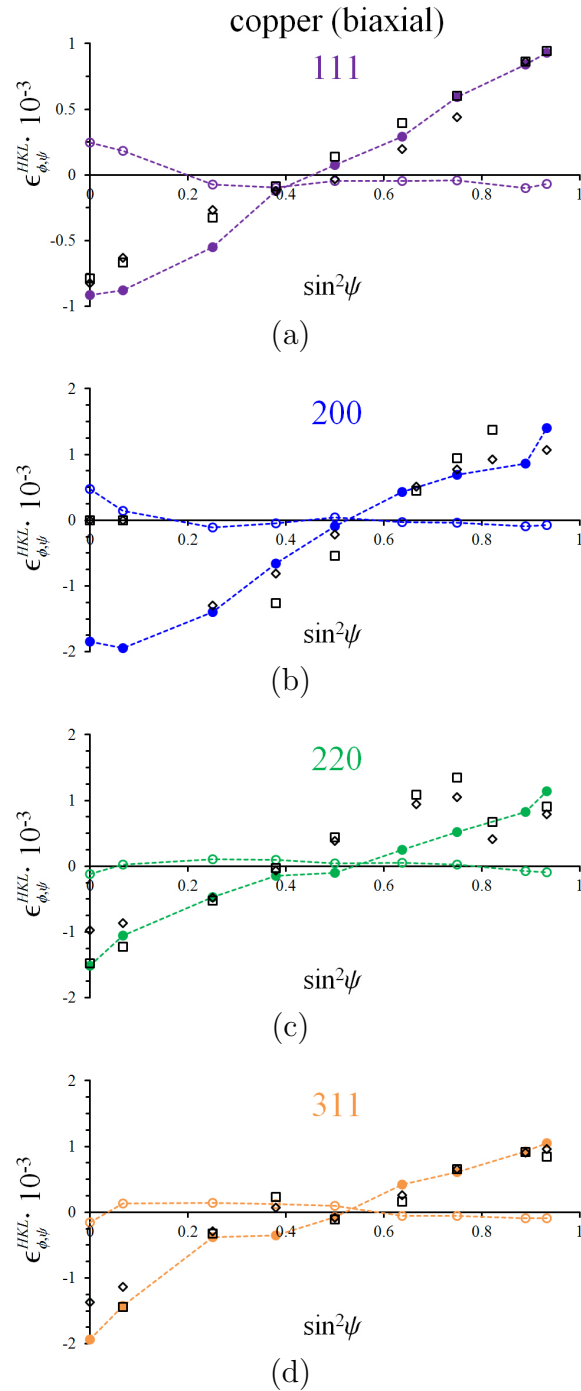


Figure 3.5: Measured lattice strain  $\epsilon$  as a function of  $\sin^2\psi$  for various reflections recorded from a Cu thin film on a Si-wafer before the application of load (open circles) and in the loaded state (filled circles). The loading was achieved by cooling from room temperature to  $-120^\circ\text{C}$ , resulting in a biaxially rotationally symmetric stress state with  $\sigma_{\parallel} \equiv \sigma_{11} = \sigma_{22} = 280$  MPa. Error bars for the data are of the same order as the size of the symbols. The dashed lines through these data points have been drawn to guide the eye. Further, lattice-strain data as predicted according to the Reuss (open boxes) and Vook-Witt (open diamonds) grain-interaction models, for the case of a 111-fiber texture resembling the 111-fiber texture in the specimen (see Figure 3.3), have been plotted as well.

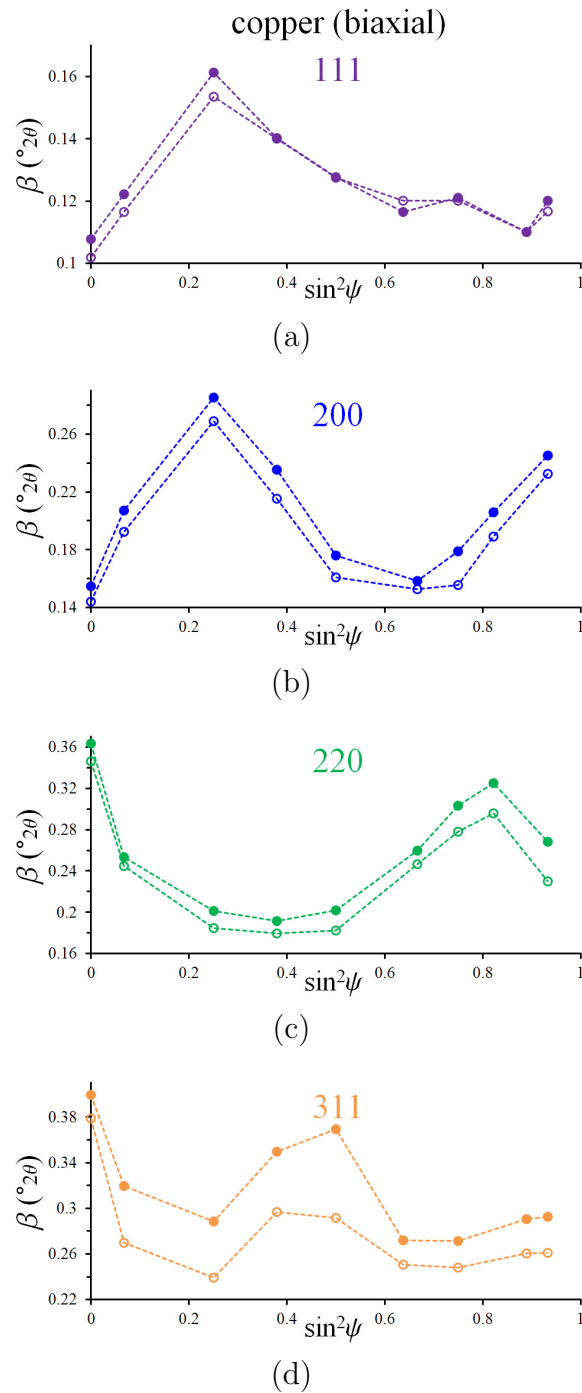


Figure 3.6: Measured integral breadth  $\beta$  as a function of  $\sin^2 \psi$  for a Cu thin film on a Si-wafer before the application of load (open circles) and in the loaded state (filled circles). The loading was achieved by cooling from room temperature to  $-120^\circ\text{C}$ , resulting in a biaxially rotationally symmetric stress state  $\sigma_{\parallel} \equiv \sigma_{11} = \sigma_{22} = 280 \text{ MPa}$ . Error bars for the data are of the same order as the size of the symbols. The dashed lines through these data points has been drawn to guide the eye.

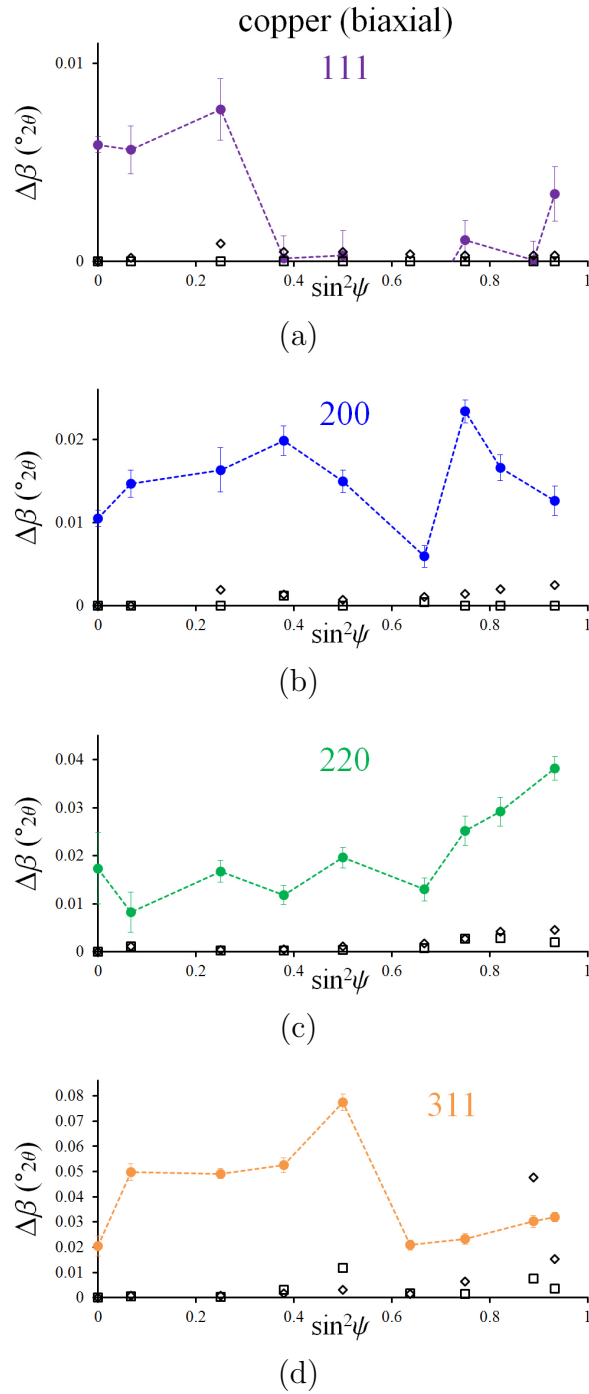


Figure 3.7: Measured diffraction-line broadening induced by loading (given as the integral breadth broadening contribution  $\Delta\beta$ , Equation 3.9) as a function of  $\sin^2\psi$  for a Cu thin film on a Si-wafer in the loaded state (filled circles), for reflections 111, 200, 220, and 311. The loading was achieved by cooling from room temperature to  $-120^\circ\text{C}$ , resulting in a biaxially rotationally symmetric stress state  $\sigma_{\parallel} \equiv \sigma_{11} = \sigma_{22} = 280 \text{ MPa}$ . The broadening contribution as predicted according to the isotropic Reuss (open boxes) and the anisotropic Vook-Witt (open diamonds) grain-interaction models, for the case of a 111-fiber texture resembling the 111-fiber texture in the specimen (see Figure 3.3), have been indicated as well.

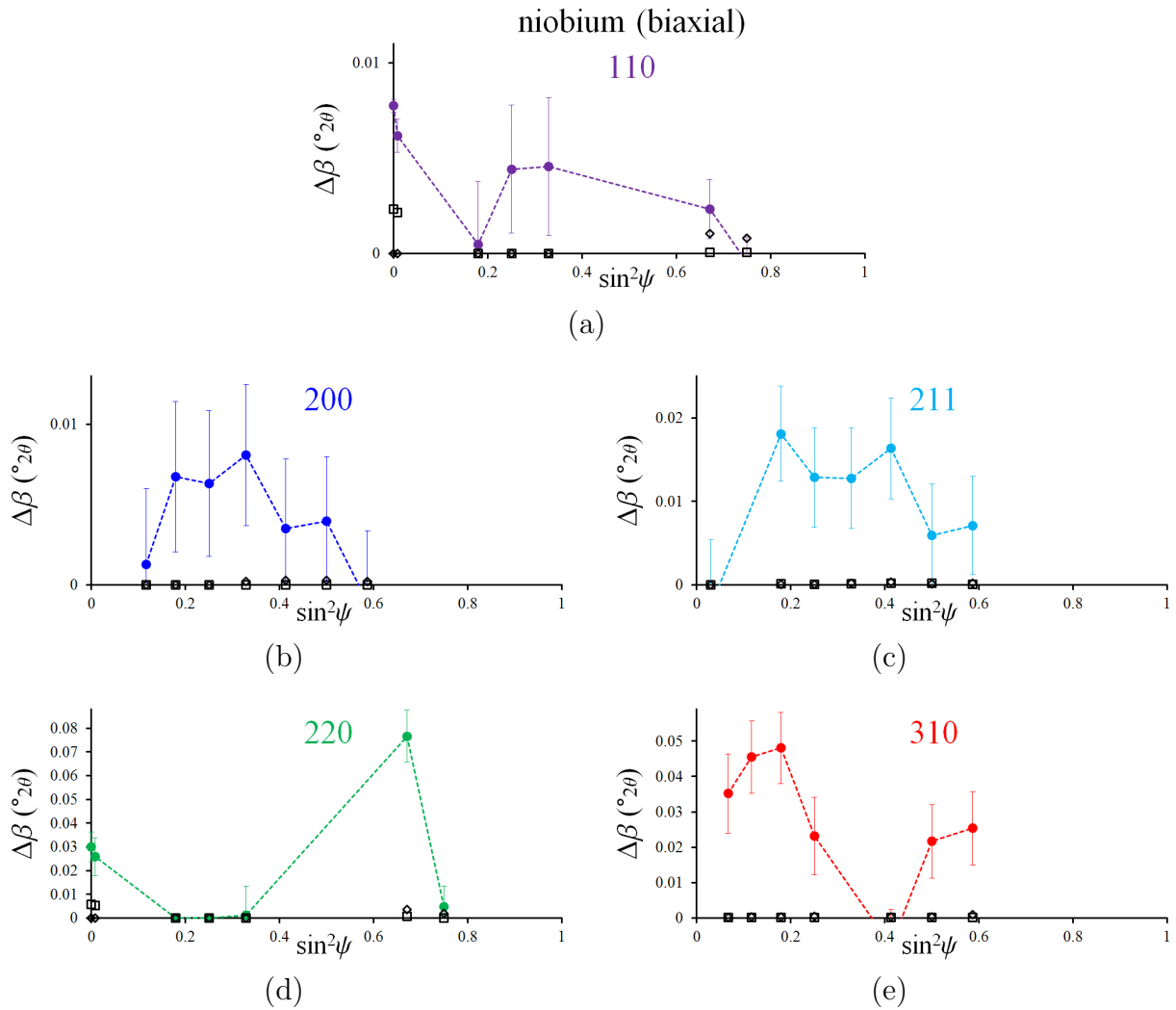


Figure 3.8: Measured diffraction-line broadening induced by loading (given as the integral breadth broadening contribution  $\Delta\beta$ , Equation 3.9) as a function of  $\sin^2\psi$  for a Nb thin film on an Al-wafer in the loaded state (filled circles), for reflections 110, 200, 211, 220, and 310. The loading was achieved by cooling from room temperature ( $\sigma_{\parallel}^{res.} \equiv \sigma_{11}^{res.} = \sigma_{22}^{res.} = 350$  MPa) to  $-120^\circ\text{C}$ , resulting in an applied compressive rotationally symmetric biaxial stress state of approximately  $\sigma_{\parallel} \equiv \sigma_{11} = \sigma_{22} = -350$  MPa (i.e.  $\sigma_{\parallel} = 0$  MPa at  $-120^\circ\text{C}$ ). Further, the broadening contribution as predicted according to the isotropic Reuss (open boxes) and the anisotropic Vook-Witt (open diamonds) grain-interaction models, for the case of a 110-fiber texture resembling the 110-fiber texture in the specimen, have been indicated as well.

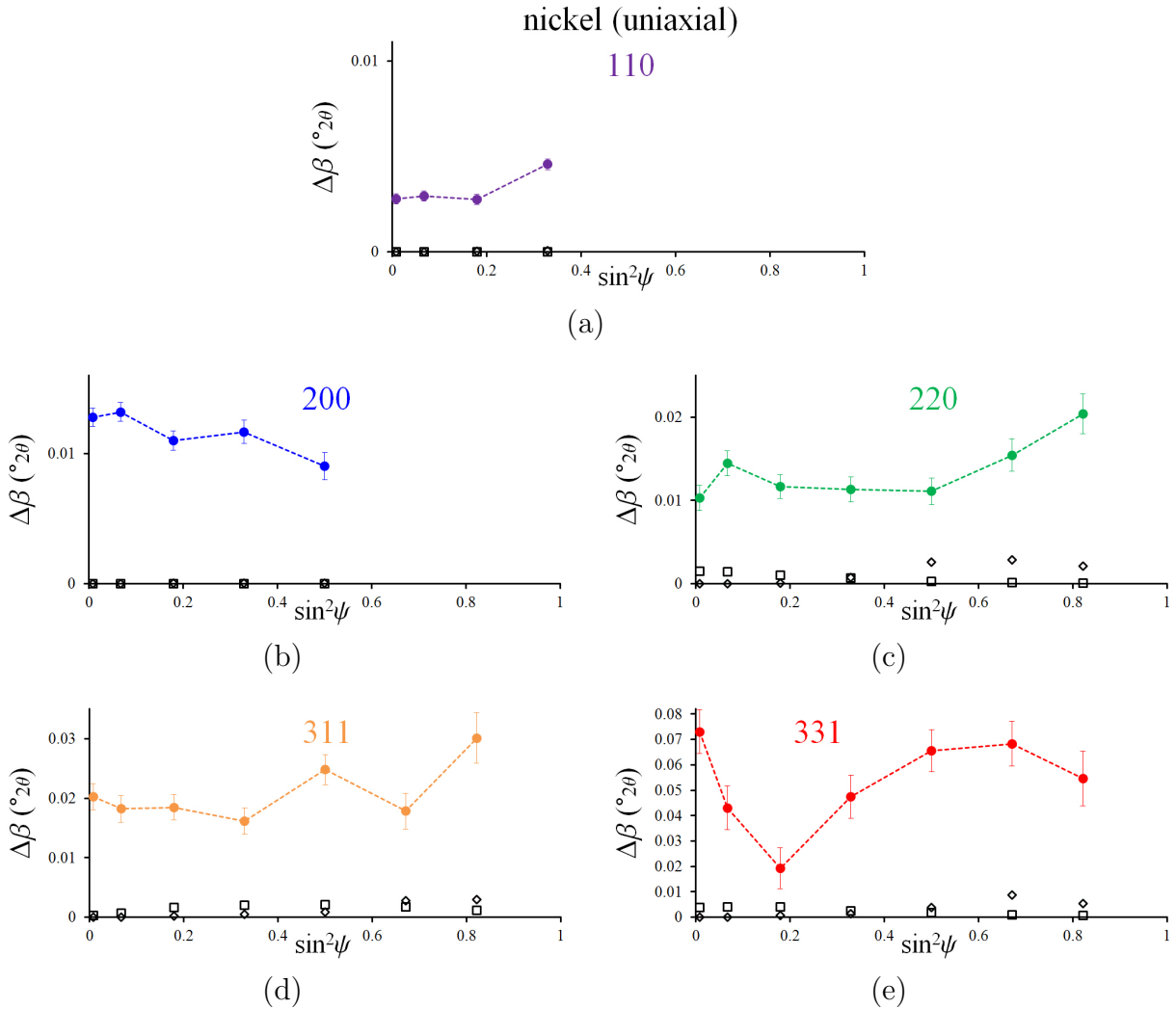


Figure 3.9: Measured diffraction-line broadening induced by loading (given as the integral breadth broadening contribution  $\Delta\beta$ , Equation 3.9) as a function of  $\sin^2\psi$  for a Ni dog-bone specimen in the loaded state (filled circles), for reflections 111, 200, 220, 311, and 331. The loading was achieved by applying a uniaxial load of 100 MPa to the specimen ( $\sigma_{11}^{res.} = 125$  MPa), resulting in an overall uniaxial stress state of approximately  $\sigma_{11} = 225$  MPa. The broadening contribution as predicted according to the isotropic Reuss (open boxes) and the anisotropic Vook-Witt (open diamonds) grain-interaction models, for the case of an untextured polycrystalline aggregate, have been indicated as well.



Within the restrictions indicated by the above discussion, to facilitate the comparison of experiments with different magnitudes of loading, the parameter  $\Delta\beta/\sigma^2$  is introduced to normalize the loading-induced broadening with respect to the magnitude of the applied stress (for the same type of state of stress), where the quantity  $\sigma$  is a scalar representing the magnitude of applied principal stress component(s). (Thus, for the biaxially rotationally symmetric stress states,  $\sigma = \sigma_{\parallel}$ , and for the uniaxial stress states  $\sigma = \sigma_{11}$ ). Such results for  $\Delta\beta/\sigma^2$  are shown in Figure 3.10 for the biaxially rotationally symmetric applied states of stress and in Figure 3.11 for the uniaxially applied states of stress.

The results for  $\Delta\beta/\sigma_{\parallel}^2$  (Figure 3.10) and for  $\Delta\beta/\sigma_{11}^2$  (Figure 3.11) clearly exhibit the role of the degree of the intrinsic elastic anisotropy (see Table 3.2): the degree of loading-induced broadening, in the case of biaxial loading, increases in the order  $W \rightarrow Nb \rightarrow Cu$  and, in the case of uniaxial loading, is larger for Ni than for W. Obviously, the practically intrinsically elastically isotropic W does not exhibit (resolvable) loading-induced broadening.

Calculations according to the isotropic Reuss and the anisotropic Vook-Witt grain-interaction models, for each of the specimens investigated, were performed. The results can be compared with the experimental data; see Figure 3.5 for the average lattice strain (for Cu) and see Figures 3.7-3.9 for the diffraction-line broadening data of the Cu and Nb thin film specimens and the Ni dog-bone specimen, respectively. (To calculate a theoretical value for diffraction-line broadening, the *strain-induced broadening contribution function*  $f(2\theta)$ , as calculated for the experimental conditions according to a given grain-interaction model, was convoluted with the measured diffraction peak for the specimen in the “unloaded” state. The breadth of this convoluted, or “loaded,” function was then compared to that of the “unloaded” peak to determine the predicted diffraction-line broadening  $\Delta\beta$ . See Reference [17] for description of such calculations.)

The predicted amounts of diffraction-line broadening according to the isotropic Reuss model and the anisotropic Vook-Witt model are much less than the experimentally observed diffraction-line broadening (Figures 3.7-3.9).

The variation in strain throughout the aggregate does not only depend on the orientation of an individual grain, as implied by all grain-interaction models, but also on the (shape, number/size, and) crystallographic orientation, with respect to the specimen frame of reference, of its nearest neighbors, which effects are not considered at all in the grain-interaction models. Grains of identical orientation at different locations in the aggregate will *not* have the same average lattice strain, and the same lattice-strain distribution within the grains, due to these local variations in the microstructure. As a consequence the strain variation predicted by the grain-interaction models is distinctly smaller than the experimentally determined one (see Figures 3.7-3.9). Yet, the average lattice strain (calculated as a function of peak position for various  $\psi$  tilts) is predicted quite well: for example, see Figure 3.5.

The above discussed observations lead to the conclusion that the current grain-interaction

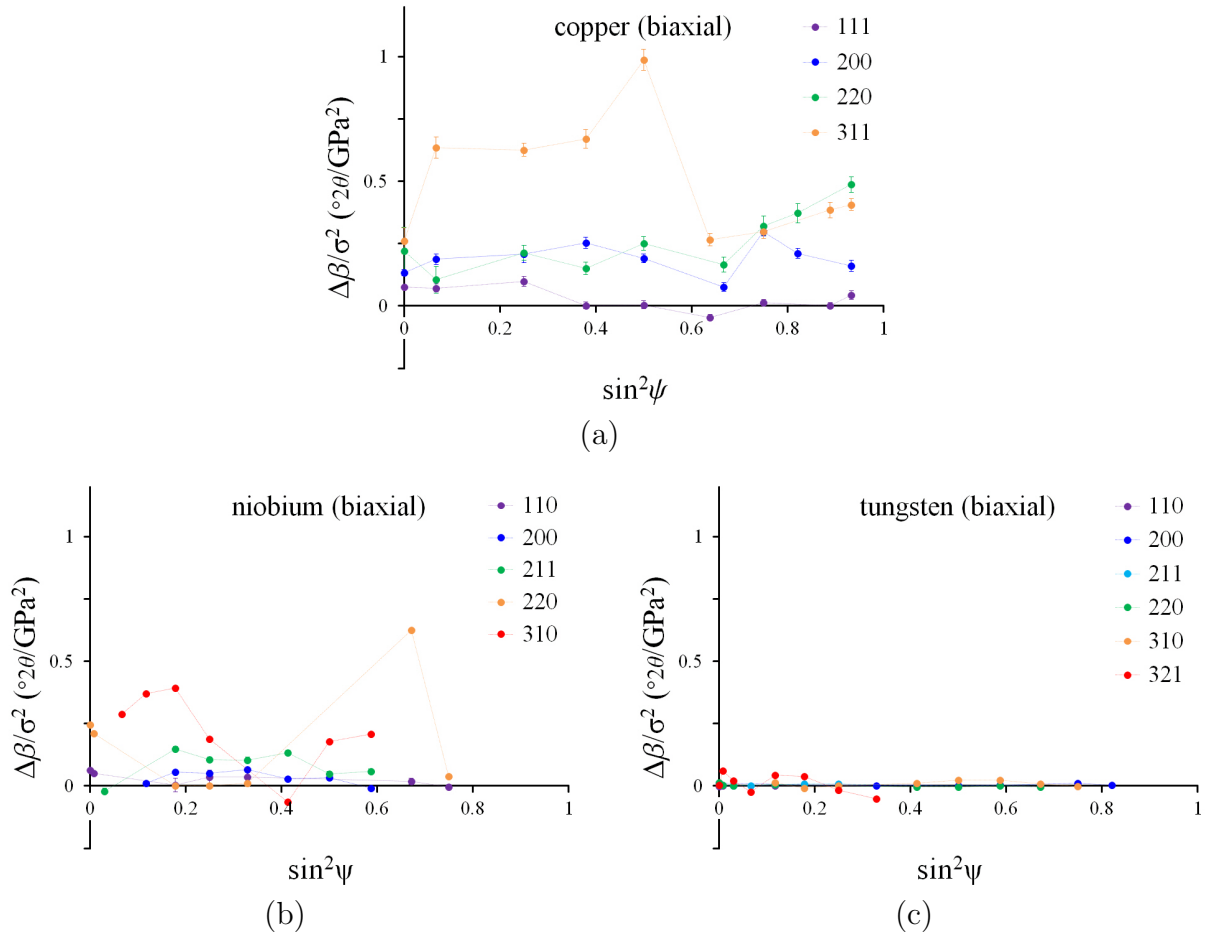


Figure 3.10: Integral breadth broadening data scaled by the square of the applied load magnitude  $\Delta\beta/\sigma_{\parallel}^2$  for various reflections ( $HKL$  and corresponding color indicated in legend) for (a) a Cu thin film on a Si-wafer cooled from room temperature to  $-120^{\circ}\text{C}$ , resulting in biaxially rotationally symmetric stress state of  $\sigma_{\parallel} \equiv \sigma_{11} = \sigma_{22} = 280$  MPa, (b) a Nb thin film on an Al-wafer cooled from room temperature ( $\sigma_{\parallel}^{res.} = 350$  MPa) to  $-120^{\circ}\text{C}$ , resulting in an applied compressive rotationally symmetric biaxial stress state of approximately  $\sigma_{\parallel} \equiv \sigma_{11} = \sigma_{22} = -350$  MPa, and (c) a W thin film on an Al-wafer cooled from room temperature ( $\sigma_{\parallel}^{res.} = 1460$  MPa) to  $-120^{\circ}\text{C}$ , resulting in an additionally applied compressive rotationally symmetric biaxial stress state of approximately  $\sigma_{\parallel} \equiv \sigma_{11} = \sigma_{22} = -1260$  MPa (i.e.  $\sigma_{\parallel} \equiv \sigma_{11} = \sigma_{22} = -2720$  MPa)

models are unable to describe the complete strain distribution within an elastically loading polycrystalline aggregate. Such models are over-simplifications of the grain interactions occurring in reality; however, these simplifications do allow for fairly accurate predictions of the average lattice strain to be made.

The discrepancies between the experimental data and the grain-interaction model predictions for the diffraction-line broadening can thus be explained by recognizing that several types of strain variation occur within an elastically loaded polycrystalline aggregate: (i) macro-, (ii) meso-, and (iii) microvariations in strain:

- (i) *Macrovariation* in strain is the variation of the average lattice strain, the average

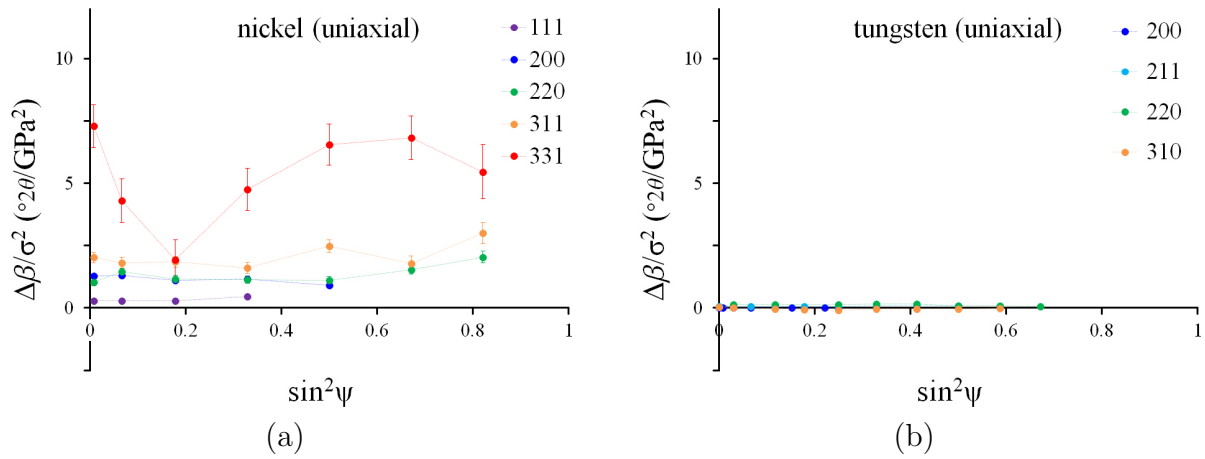


Figure 3.11: Integral breadth broadening data scaled by the square of the applied load magnitude  $\Delta\beta/\sigma_{11}^2$  for various reflections ( $hkl$  and corresponding color indicated in legend) recorded from (a) a Ni dog-bone ( $\sigma_{11}^{res.} = 125$  MPa) loaded by 100 MPa, resulting in a uniaxial stress state of  $\sigma_{11} = 225$  MPa and (b) a W dog-bone ( $\sigma_{11}^{res.} = -600$  MPa) loaded by 150 MPa, resulting in a uniaxial stress state of  $\sigma_{11} = -450$  MPa

taken for the groups of diffracting grains, that occurs upon changing the orientation of the diffraction vector with respect to the specimen frame of reference. This macrovariation in lattice strain is expressed in this paper by the variation of  $\epsilon_{\phi,\psi}^{HKL}$  (as a function of  $\sin^2\psi$ ).

- (ii) *Mesovariation* in strain is the variation of the average lattice strain, the average now taken per diffracting grain, for the group of diffracting grains sharing a fixed orientation of the diffraction vector. This mesovariation in lattice strain is expressed in this paper by the variation of  $\epsilon_{\phi,\psi}^{HKL}(\chi)$ . Two types of *mesovariation* of lattice strain are distinguished: (a) mesovariation by variable  $\chi$  (as considered in the grain-interaction models) and (b) mesovariation at constant  $\chi$  due to different local surroundings.
- (iii) *Microvariation* in strain is the variation of lattice strain within an individual grain.

It is essential to recognize that *all* published grain-interaction models, i.e. including those considered in this paper, do not take into account the above described *microvariation* nor the entire magnitude of *mesovariation* (type (b) is ignored) in lattice strain. Therefore, broadening of the  $H00$  and  $HHH$  peaks was observed, although no broadening is predicted by the isotropic grain-interaction models and the predicted broadening by the anisotropic grain-interaction models is much too small.

## 3.5 Conclusions

- The measured diffraction-line broadening induced by elastic loading is much larger than that predicted by elastic grain-interaction models as proposed in the literature.
- Three sources of lattice-strain variation can be identified:
  - (i) macrovariation in lattice strain: the variation of the average lattice strain for the groups of diffracting crystallites;
  - (ii) mesovariation in lattice strain: the variation of the average lattice strain per grain for the group of diffracting crystallites;
  - (iii) microvariation in lattice strain: the variation of strain within a diffracting crystallite.
- The grain-interaction models presented so far only consider the macrovariation and a part of the mesovariation in lattice strain and ignore the microvariation in lattice strain. In other words: the grain-interaction models do not take into account the effects of the different surroundings in the specimen for each of the diffracting grains (of even possibly identical crystallographic orientations with respect to the specimen frame of reference). Hence, the current grain-interaction models severely underestimate the diffraction-line broadening for general HKL reflections.
- Elastic grain interaction induces diffraction-line broadening for also the  $H00$  and  $HHH$  reflections recorded from cubic materials, in contrast with predictions from the isotropic grain-interaction models and much larger than predicted by the anisotropic grain-interaction models.
- The larger the degree of intrinsic elastic anisotropy of a material, the larger the magnitude of strain variation, and thus diffraction-line broadening.
- Texture reduces the overall strain variation in, and thus the diffraction-line broadening for, a polycrystalline aggregate due to the intrinsic elastic anisotropy of the material, as the “range” of orientation variation of the grains within the material is reduced in the presence of texture.

This work has demonstrated that distinct broadening of diffraction lines, observable in XRD measurements made using synchrotron radiation, is induced by elastic loading of a polycrystalline aggregate. An analysis as provided in this work, of diffraction-line broadening induced by elastic loading of a polycrystalline aggregate, is a sensitive means to reveal the essentials of the real grain interactions occurring in a specimen.

## Acknowledgements

We are grateful for the permission for measurements at the Synchrotron Light Source ANKA at the MPI-IS beamline for Surface Diffraction. We thank Mr. R. Weigel, Dr. M. Mantilla, Dipl.-Ing. S. Kurz, and Dipl.-Ing. J. Stein for assistance during the measurements. The authors also thank Dr. F. Theile for assistance with the sputter-deposition of the thin film specimens and Mrs. M. Dudek for assistance with preparation of specimens for X-ray diffraction analysis.

# Bibliography

- [1] G. B. Greenough, “Quantitative X-ray diffraction observations in strained metal aggregates,” *Progress in Metal Physics*, vol. 3, pp. 176–219, 1952.
- [2] W. Voigt, *Lehrbuch der Kristallphysik*. Teuber, Leipzig-Berlin, 1910.
- [3] A. Reuss, “Account of the liquid limit of mixed crystals on the basis of the plasticity condition for single crystal,” *Zeitschrift für Angewandte Mathematik und Mechanik*, vol. 9, pp. 49–58, 1929.
- [4] H. Neerfeld, “Zur Spannungsberechnung aus röntgenographischen Dehnungsmessungen,” *Mitteilung Kaiser-Wilhelm-Institut-Eisenforschung*, vol. 24, pp. 61–70, 1942.
- [5] R. Hill, “The elastic behaviour of a crystalline aggregate,” *Proceedings of the Physical Society A*, vol. 65, no. 389, pp. 349–355, 1952.
- [6] J. D. Eshelby, “The determination of the elastic field of an ellipsoidal inclusion, and related problems,” *Proceedings of the Royal Society A*, vol. 241, no. 1226, pp. 379–396, 1957.
- [7] E. Kröner, “Berechnung der elastischen konstanten des vielkristalls aus den konstanten des einkristalls,” *Zeitschrift für Physik*, vol. 151, no. 4, pp. 504–518, 1958.
- [8] R. W. Vook and F. Witt, “Thermally induced strains in evaporated films,” *Journal of Applied Physics*, vol. 36, no. 7, pp. 2169–2171, 1965.
- [9] F. Witt and R. W. Vook, “Thermally induced strains in cubic metal films,” *Journal of Applied Physics*, vol. 39, no. 6, pp. 2773–2776, 1968.
- [10] M. van Leeuwen, J.-D. Kamminga, and E. J. Mittemeijer, “Diffraction stress analysis of thin films: Modeling and experimental evaluation of elastic constants and grain interaction,” *Journal of Applied Physics*, vol. 86, no. 1904, pp. 1904–1914, 1999.
- [11] U. Welzel and E. J. Mittemeijer, “Diffraction stress analysis of macroscopically elastically anisotropic specimens: On the concepts of diffraction elastic constants and stress factors,” *Journal of Applied Physics*, vol. 93, no. 11, pp. 9001–9011, 2003.
- [12] U. Welzel and S. Fréour, “Extension of the Vook-Witt and the inverse Vook-Witt elastic grain-interaction models to general loading states,” *Philosophical Magazine*, vol. 87, no. 26, pp. 3921–3943, 2007.

- [13] N. Koch, U. Welzel, H. Wern, and E. J. Mittemeijer, "Mechanical elastic constants and diffraction stress factors of macroscopically elastically anisotropic polycrystals: the effect of grain-shape (morphological) texture," *Philosophical Magazine*, vol. 84, no. 33, pp. 3547–3570, 2004.
- [14] C. M. Sayers, "The strain distribution in anisotropic polycrystalline aggregates subjected to an external stress field," *Philosophical Magazine A*, vol. 49, no. 2, pp. 243–262, 1984.
- [15] N. Funamori, M. Funamori, R. Jeanloz, and N. Hamaya, "Broadening of X-ray powder diffraction lines under nonhydrostatic stress," *Journal of Applied Physics*, vol. 82, no. 1, pp. 142–146, 1997.
- [16] A. K. Singh and C. Balasingh, "X-ray diffraction line broadening under elastic deformation of polycrystalline sample: An elastic-anisotropy effect," *Journal of Applied Physics*, vol. 90, no. 5, pp. 2296–2302, 2001.
- [17] M. K. A. Koker, U. Welzel, and E. J. Mittemeijer, "Elastic mechanical grain interactions in polycrystalline materials; analysis by diffraction-line broadening," *Philosophical Magazine*, vol. 000, no. 0, pp. 000–000, 201X.
- [18] J. F. Nye, *Physical Properties of Crystals*. Oxford University Press, 1957.
- [19] C. Giacovazzo, H. L. Monaco, G. Artioli, D. Viterbo, G. Ferraris, G. Gilli, G. Zanotti, and M. Catti, *Fundamentals of Crystallography*. Oxford University Press, 2nd edition, ed., 2002.
- [20] H. J. Bunge, "Zur Darstellung allgemeiner Texturen," *Zeitschrift für Metallkunde*, vol. 56, no. 12, p. 872, 1965.
- [21] H. J. Bunge and W. T. Roberts, "Orientation Distribution, Elastic and Plastic Anisotropy in Stabilized Steel Sheet," *Journal of Applied Crystallography*, vol. 2, pp. 116–128, 1969.
- [22] R.-J. Roe and W. R. Krigbaum, "Description of crystallite ordination in polycrystalline materials having fiber texture," *Journal of Chemical Physics*, vol. 40, no. 9, pp. 2608–2615, 1964.
- [23] H.-J. Bunge, *Texture Analysis in Material Science*. Butterworth, 1982.
- [24] U. Welzel, M. Leoni, and E. J. Mittemeijer, "The determination of stresses in thin films; modelling elastic grain interaction," *Philosophical Magazine*, vol. 83, no. 5, pp. 603–630, 2003.
- [25] U. Welzel, J. Ligot, P. Lamparter, A. C. Vermeulen, and E. J. Mittemeijer, "Stress analysis of polycrystalline thin films and surface regions by X-ray diffraction," *Journal of Applied Crystallography*, vol. 38, pp. 1–29, 2005.

- [26] U. Welzel, S. Fréour, and E. J. Mittemeijer, “Direction-dependent elastic grain-interaction models - a comparative study,” *Philosophical Magazine*, vol. 85, no. 21, pp. 2391–2414, 2005.
- [27] C. J. Smithells and E. A. Brandes, *Metals Reference Book*. Butterworths, 5th edition ed., 1976.
- [28] M. M. Hall, “The approximation of symmetric x-ray peaks by Pearson type VII distributions,” *Journal of Applied Crystallography*, vol. 10, pp. 66–68, 1977.
- [29] A. R. Stokes and A. J. C. Wilson, “The diffraction of x-rays by distorted crystal aggregates,” *Proceedings of the Physical Society A*, vol. 56, pp. 174–181, 1944.
- [30] A. J. C. Wilson, “On variance as a measure of line broadening in diffractometry general theory and small particle size,” *Proceedings of the Physical Society A*, vol. 80, no. 513, pp. 286–294, 1962.
- [31] A. J. C. Wilson, “On variance as a measure of line broadening in diffractometry .2. mistakes and strain,” *Proceedings of the Physical Society A*, vol. 81, no. 519, pp. 41–46, 1963.
- [32] E. J. Mittemeijer and U. Welzel, “The state of the art of the diffraction analysis of crystallite size and lattice strain,” *Zeitschrift für Kristallographie*, vol. 223, no. 9, pp. 552–560, 2008.
- [33] A. C. Vermeulen, R. Delhez, T. H. de Keijser, and E. J. Mittemeijer, “Changes in the densities of dislocations on distinct slip systems during stress relaxation in thin aluminum layers: the interpretation of x-ray diffraction line broadening and line shift,” *Journal of Applied Physics*, vol. 77, no. 10, pp. 5026–5049, 1995.
- [34] A. Leineweber and E. J. Mittemeijer, “Notes on the order-of-reflection dependence of microstrain broadening,” *Journal of Applied Crystallography*, vol. 43, pp. 981–989, 2010.



## Chapter 4

# X-ray diffraction study of the temperature-induced reverse martensitic transformation in near-equiatomic NiTi shape memory thin films

M. K. A. Koker, J. Schaab, N. Zotov, and E. J. Mittemeijer

### Abstract

The development of stresses, phase fraction, and the microstructure of thin equiatomic NiTi substrate-bound films was investigated during the heating-induced transformation from martensite to austenite. Synchrotron x-ray diffraction (XRD) experiments were performed during (the heating portion of) thermal cycling applied to the thin films to capture, in particular, the reverse martensitic phase transformation (monoclinic martensite  $\rightarrow$  cubic austenite). The phase fraction and microstructure, as a function of temperature and thermal cycling, were analyzed through the application of Rietveld refinement to the diffraction data. Further, using the XRD data, the overall macroscopic stress in the film (derived from the curvature of the film/substrate system determined by XRD rocking curve measurements) and the stress in the austenite phase (derived from the lattice strain) during the transformation were tracked as a function of the degree of the transformation. The state of the stress in the austenite was found to remain biaxially, rotationally symmetric, even in the two-phase (martensite and austenite) film. The developments of the total stress in the film and the stresses in each of the two phases were discussed in terms of the transformation-induced volume misfit and its accommodation by elastic deformation.

## 4.1 Introduction; thermal cycling and stress development

Shape-memory materials, in particular near-equiatomic NiTi alloys, are of high interest for application in the field of microelectromechanical systems (MEMS) [1–3] due to their unique pseudoelastic and shape-memory thermoelastic properties. These effects can be utilized to construct sensors and actuators, which are highly effective due to the high work output per unit volume [4]. Such materials exhibit a reversible martensitic phase transformation between the austenite (A) and martensite (M) phases. The forward and reverse transformation can be realized by applying stress or by changing the temperature. Shape memory properties have been observed in films as thin as 100 nm [5].

Small variations in the chemical composition of about equiatomic NiTi [6], the thermo-mechanical history [4], and the sputtering parameters during deposition [7–9] have a significant effect on the shape-memory properties (e.g. transformation temperatures) and the formation of precipitates in NiTi thin film systems.

The state of stress of the NiTi film also plays a crucial role for its effective application in MEMS. Crystallization of sputter-deposited NiTi films must be performed at high temperatures (either during deposition or as a post-processing step), forming a single-phase austenite film. Upon initial cooling of the substrate-bound film, a residual, extrinsic stress develops in the austenite phase due to the thermal misfit between the substrate and the NiTi film. A high degree of residual stress in the film can, depending on the nature of the stress, partially or completely suppress the shape-memory properties of the material. Therefore, being able to “tune” the stress state of the substrate-bound film is important. The development of residual stresses depends on the Ni-Ti composition (e.g. by the formation of precipitates) and the deposition parameters [7]. Annealing of substrate-bound NiTi films above 600°C has been observed to reduce the residual stress in NiTi thin films [7, 10].

The magnitude of stress in the film changes due to the forward and reverse martensitic phase transformation induced by cooling and heating. The (absolute value of the) difference in the magnitude of stress prior to and after the (forward or reverse) transformation is defined as the *recovery stress* (usually the stress contribution of the thermal misfit, as a consequence of the temperature change during the transformation, is included) [10]. The *recovery stress* can be used to characterize the magnitude of work which can be exerted by the material upon transformation.

A thermal cycle is defined as heating from below the martensite finish temperature  $M_f$  to above the austenite finish temperature  $A_f$ , and then cooling again to below  $M_f$ . Upon continued thermal cycling of *bulk* NiTi shape-memory materials, the phase transformation shifts to lower temperatures [11, 12]. Similar observations have been made for near-equiatomic substrate-bound NiTi *thin films* [13]. After a number of thermal cycles, the material reaches a reproducible state, implying that the transformation temperatures

(practically) no longer change upon further cycling. The transient behavior upon thermal cycling has been attributed to the increase of the density of defects and dislocations, resulting in a higher degree of undercooling necessary for the forward transformation ( $A \rightarrow M$ ) to proceed [11–14]. (See, for a similar phenomenon, results for the hcp-fcc transformation in cobalt [15].)

Thermal cycling may influence the magnitude of the stresses in the film. Quantitative data for the changes in the stress state, especially for substrate-bound NiTi thin films during thermal cycling, are very scarce. This provided the motivation in this project for determination of the stress in thin NiTi films after different numbers of cycles.

A common method for measuring the macroscopic stress in substrate-bound thin films involves measuring the curvature of the substrate-bound film [16], where stress can be directly related to curvature by the Stoney equation [17]. (See Section 4.3.2.2.) For NiTi thin films, an abrupt change in curvature indicates the occurrence of the phase transformation [4] and allows for determination of the *recovery stress* [10, 18].

The use of *in situ* high temperature x-ray diffraction (XRD) methods gives access to the acquisition of detailed information on the state of stress and the microstructure in general: the overall *macroscopic film stress* can be determined from curvature measurements (employing XRD rocking curve measurements at different locations on the surface of the specimen), *stresses in the austenite and martensite phases* can be determined separately (from the average lattice strains), and also the phase fraction, the crystallographic texture, and the average crystallite size (and microstrain) (by so-called full XRD pattern analysis) can be determined. Thus, the versatility of the (*in situ*) XRD method provides a rather complete characterization of the material during a single thermal cycle, thereby avoiding the involvement of measurements by a range of different methods. The present project focuses on the evolution of stresses, phase fraction, and microstructure in substrate-bound NiTi films, during the heating-induced reverse martensitic transformation ( $M \rightarrow A$ ), as measured by *in situ* XRD methods at a synchrotron source.

The (forward and reverse) martensitic transformation in NiTi is supposed to be athermal [19]. This means that for a fixed temperature, the phase transformation instantaneously reaches a certain transformed fraction, which is thus dependent on temperature and not on time at a constant temperature. This facilitates XRD studies of the phase transformation that require, even in the case of synchrotron sources, measurement times of minutes at a given temperature.

## 4.2 Experimental procedures

### 4.2.1 Film preparation and characterization

An ATC 1500-F machine (AJA International Inc., Scituate, MA, U.S.A.) was used to deposit NiTi films by co-sputtering from pure Ni (99.995 at.%) and pure Ti (99.995 at.%) targets on pieces (14 mm by 14 mm, 0.5 mm thick) of 100-orientated Si single-crystal

wafers [13]. The chamber was evacuated by mechanical and turbomolecular pumps to obtain an ultra high vacuum ( $\sim 10^{-8}$  mbar). A bake-out process at  $150^\circ\text{C}$  for 12 hours was performed. The Ar (99.9999 at.%) pressure was regulated to be  $1.3 \cdot 10^{-3}$  mbar. Sputter cleaning of both the single-crystal Si substrates (at 45 W for 3 min) and targets (also for Ni at 45 W and for Ti at 140 W, both for 5 min) was conducted before the deposition. After cleaning, the deposition was performed for 4.5 hours at room temperature with the direct current (DC) powers of 45 W for Ni and 140 W for Ti. The NiTi films deposited at room temperature were amorphous, as is generally found to be the case [20]. Therefore, following deposition, the specimens were annealed in the vacuum chamber for 30 minutes at  $650^\circ\text{C}$  to crystallize the amorphous material into the austenite phase.

The thickness of the deposited thin films, as measured using a DekTak 8 profilometer (Bruker AXS, Karlsruhe, Germany), is found to be  $1.950(7) \mu\text{m}$ . The composition, as determined by inductively coupled plasma optical emission spectroscopy (ICP-OES), is given by 49.2(5) at.%Ni and 50.8(5) at.%Ti. The compositional homogeneity was verified at multiple locations by energy-dispersive X-ray spectroscopy (EDX). Two different specimens (NiTi09-02 and NiTi09-03) from the same batch were investigated. The first sample (NiTi09-02) was measured during the second thermal cycle, then thermally cycled seventeen times within the heating and cooling chamber (see Section 4.2.2.2) and then measured again during the twentieth cycle. The NiTi09-03 specimen was measured during its first thermal cycle.

The austenite start temperature,  $A_s = 60^\circ\text{C}$ , and the austenite finish temperature,  $A_f = 85^\circ\text{C}$ , were determined with differential scanning calorimetry (using a PerkinElmer DSC 8500 apparatus) prior to XRD measurements using pieces of film which were removed from the substrate (by first breaking the substrate and then peeling portions of the film off of the surface).

The NiTi films exhibit a columnar grain structure, typical for sputter-deposited material [21], as revealed by scanning electron microscope (SEM; using a ULTRA 55, Zeiss

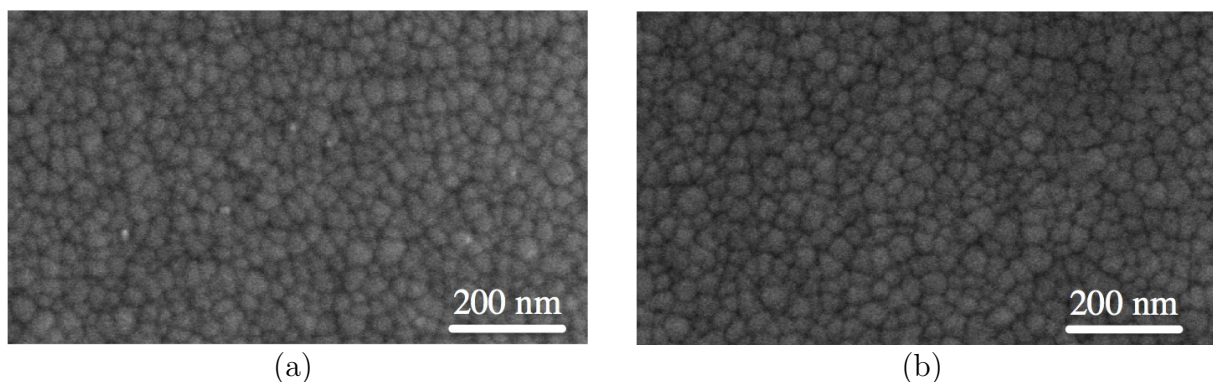


Figure 4.1: SEM images of the surface of the NiTi films (taken at 50k magnification) after completion of XRD experiments of (a) NiTi09-03 film, after the 1st cycle and (b) NiTi09-02 film, after the 20th cycle

SMT instrument) images recorded from a fractured cross-sectional surface at room temperature after the completion of the XRD synchrotron measurements. SEM images taken from the surface of the films showed that the columnar grains have an equiaxed morphology (Figure 4.1) parallel to the surface, ranging between 10 and 50 nm in diameter. No microstructural differences due to thermal cycling (by comparing the NiTi09-02 film after 20 cycles and the NiTi09-03 film after 1 cycle) were observed using SEM.

## 4.2.2 Diffraction experiments

### 4.2.2.1 Reference frames

Three Cartesian frames of reference, as shown in Figure 4.2, are necessary for the discussion of the diffraction experiments performed [22, 23]: (i) the *crystal frame of reference* ( $\mathcal{C}$ ): The conventional definition of an orthonormal crystal system, such as the one given in References [23] and [24] is adopted; (ii) the *specimen frame of reference* ( $\mathcal{S}$ ): The  $\mathcal{S}_3$  axis is orientated perpendicular to the specimen surface, and the  $\mathcal{S}_1$  and  $\mathcal{S}_2$  axes are in the surface plane; and (iii) the *laboratory frame of reference* ( $\mathcal{L}$ ): This frame is chosen in such a way that the  $\mathcal{L}_3$  axis coincides with the diffraction vector.

The relative orientation of the laboratory frame of reference with respect to the specimen frame of reference is specified by the angles  $\phi$  and  $\psi$ , where  $\psi$  is the inclination angle of the sample surface normal (i.e. the  $\mathcal{S}_3$  axis) with respect to the diffraction vector (i.e. the  $\mathcal{L}_3$  axis) and  $\phi$  denotes the rotation of the sample around the sample surface normal. The angle  $\chi$  is defined as a rotation of the laboratory frame of reference about the  $\mathcal{L}_3$  axis (the diffraction vector), where, for  $\phi = \psi = \chi = 0^\circ$ , the  $\mathcal{L}$  frame of reference coincides with the  $\mathcal{S}$  frame of reference.

In the following, angular brackets  $\langle \dots \rangle$  denote volume-weighted averages for all crystallites in the volume considered (i.e. mechanical averages). In the context of diffraction analysis, the analyzed volume is generally only a fraction of the volume of the polycrystalline specimen.

### 4.2.2.2 XRD measurements

Synchrotron XRD measurements were conducted on two NiTi thin films NiTi09-02 and NiTi09-03 at the Max Planck Institute for Intelligent Systems (formerly Metals Research) “surface diffraction beam line” at ANKA, located at the Karlsruhe Institute of Technology (KIT), Germany. All of the measurements were made using a photon energy of 8.1 keV (corresponding wavelength of  $\lambda = 1.5307 \text{ \AA}$ ). At this energy, the penetration depth of the measurement is approximately equal to the thickness of the film [25]. The beam

---

<sup>1</sup> An  $\text{LaB}_6$  calibration powder (NIST Standard Reference Material SRM-660) was measured on a spinning specimens holder to accurately determine the measurement wavelength and the instrumental broadening.

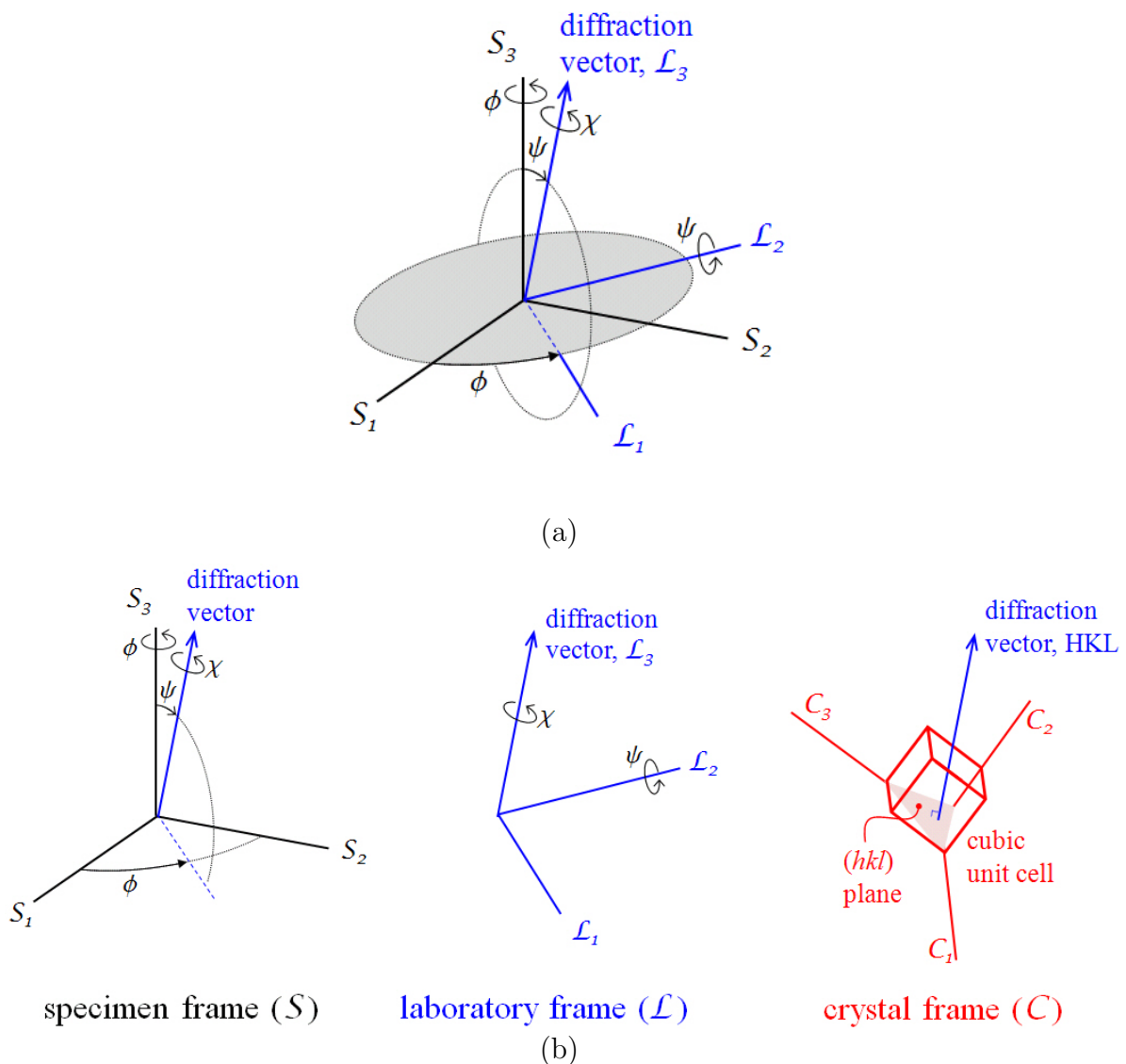


Figure 4.2: Introduction of the three Cartesian coordinate systems and the corresponding orientation angles necessary for the discussion of the diffraction experiments. (a) Laboratory frame ( $\mathcal{L}$ ) orientation with respect to the specimen frame ( $\mathcal{S}$ ) given by the angles  $\phi$ ,  $\psi$ , and  $\chi$ . (b) Orientation of reference frames with respect to the orientation of the diffraction vector (for a fixed HKL,  $\phi$ ,  $\psi$ , and  $\chi$ ).

size was measured to be approximately 1 mm by 1 mm. A set of two slits, i.e. one at both ends of a 30 cm long evacuated tube, were placed in front of a sodium iodine point detector to reduce the axial and vertical divergence of the scattered beam. The slit openings were adjustable in the horizontal and vertical directions. The horizontal slit opening was fixed at 5 mm throughout the entire experiments. The counting statistical error was kept constant by monitoring the incoming beam current and correspondingly adjusting the measurement time, recognizing that the incident beam current decays as a function of time after each injection of electrons into the storage ring.

Table 4.1: Temperatures at the measurement steps for each experiment. The specimen was held at each temperature for 3 minutes before measurements were started.

NiTi09-03	NiTi09-02	
1st cycle	2nd cycle	20th cycle
20°C	20°C	20°C
30°C	40°C	30°C
40°C	60°C	40°C
50°C	70°C	45°C
56°C	75°C	50°C
62°C	80°C	55°C
70°C	85°C	60°C
74°C	90°C	63°C
77°C	100°C	66°C
80°C	120°C	69°C
83°C		72°C
86°C		75°C
90°C		78°C
93°C		81°C
96°C		84°C
100°C		87°C
110°C		90°C
120°C		95°C
		100°C
		110°C
		120°C

Three separate experiments were performed at different stages of thermal cycling: the film NiTi09-02 was measured during the second thermal cycle and the twentieth thermal cycle (i.e. beyond the transient state of thermal cycling; see Section 4.3) and the film NiTi09-03 was measured during the first thermal cycle.

Each XRD experiment consisted of multiple measurements for each specimen during step-wise heating, i.e. the specimen was held at a constant temperature while XRD measurements were made, before being heated to the next temperature. The measurement temperatures for each of the experiments are given in Table 4.1. The heating rate was  $5^\circ\text{C}/\text{min}$ . A delay of 3 minutes was used at each new temperature before starting the XRD measurements to avoid possible temperature over-shooting effects. First, the specimens, after preparation, were cooled down to  $-20^\circ\text{C}$ , well below the martensitic finish temperature  $M_f$ , and then heated step-wise to, finally, above the austenitic finish temperature  $A_f$ . Scans of  $\theta-2\theta$  were recorded in the  $2\theta$ -range from  $18^\circ$  to  $55^\circ$  at a fixed specimen orientation defined by  $\psi = 0^\circ$  and  $\phi = 0^\circ$ .

The *in situ* heating was performed using a heating and cooling chamber (MRI Physikalische Geräte GmbH, Karlsruhe, Germany) equipped with a Be-dome, transparent to x-rays, and mounted on a six-circle Eulerian cradle. The specimens, with dimensions 14 mm by

14 mm, were fixed with metal clamps on the surface of the heating stage (see Figure 4.3). During heating and cooling, a vacuum of approximately  $10^{-3}$  Pa was maintained in the chamber. The temperature was controlled by a K-type thermocouple with an accuracy of  $\pm 1^\circ\text{C}$ . The specimen was first adjusted to lie in the center of the Eulerian cradle and then the proper height was determined by moving the specimen upward and downward in the primary beam.

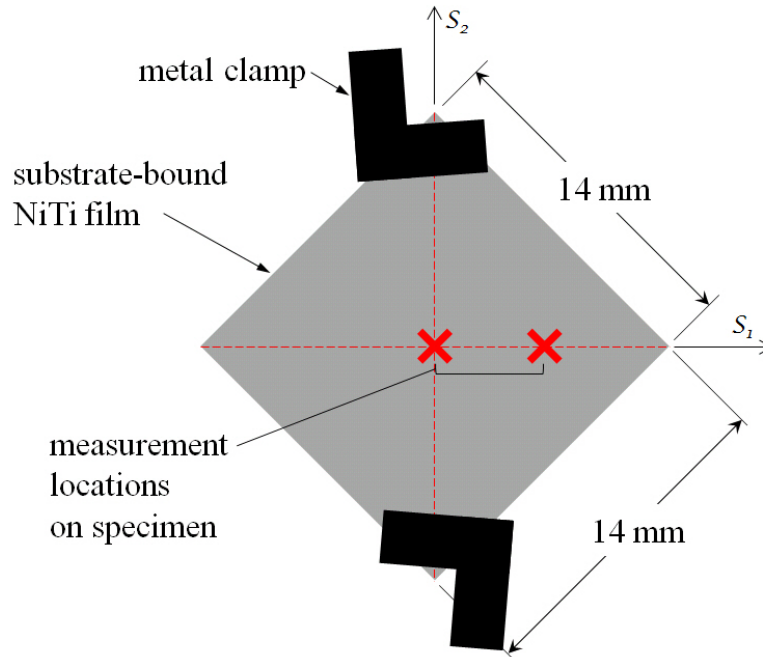


Figure 4.3: Depiction of thin film specimen mounting, including approximate location of measurement positions on the specimen and orientation of specimen frame of reference

At a few selected temperatures above  $A_s$ , the stress in the austenite phase was determined using the  $\sin^2 \psi$ -method [25] for the 110 (and in some cases also the 310) austenite reflection(s). At low austenite-phase fractions, the intensity of the 110 (and 310) austenite reflection(s) is very low. Therefore, the stress analysis using the  $\sin^2 \psi$ -method was only performed at temperatures where a significant phase fraction of austenite was present in the film. For the first experiment (i.e. on the NiTi09-02 film, 2nd heating cycle), the full planar stress state (with  $\sigma_{11}$ ,  $\sigma_{12}$ ,  $\sigma_{22}$  as non-zero stress components) using this method was measured using different  $\phi$  angles. It follows that the planar state of stress is practically rotationally symmetric (see Section 4.3.2.1). Therefore, for the following two experiments (i.e. on the NiTi09-02 film, 20th cycle and the NiTi09-03 film, 1st cycle), a biaxially rotationally symmetric planar state of stress was assumed, implying that only measurements at  $\phi = 0^\circ$  were performed, thereby significantly reducing the total measurement time.

The overall, macroscopic stress in the substrate-bound film was calculated from the curvature of the specimen. To this end, rocking curves of the Si 400 reflection at different locations on the specimen's surface were performed to obtain the substrate curvature along



the  $\mathcal{S}_1$  direction. (See Section 4.3.2.2 and Figure 4.3.) The clamps holding the specimen (see Figure 4.3) are thought to have a negligible effect because: (i) the stress state in the austenite phase is found to be biaxially, rotationally symmetric (see Section 4.3.2.1) and (ii) any influence on the bending by the clamps (along  $\mathcal{S}_2$ ) would not significantly affect the measured curvature (along  $\mathcal{S}_1$ ). Other methods for measurement of the film curvature, e.g. laser beam scattering, can be very precise for calculating the average macroscopic stress in thin films, but require that the specimen size be relatively large (usually a standard 4 inch wafer specimen is necessary). Another drawback is that such a measurement must be performed *ex situ* from phase analysis, whereas the XRD curvature experiments are made *in situ*.

### 4.3 Results and discussion

Thermal cycling revealed a fully reversible austenite-martensite phase transformation. Upon cooling from the austenite-phase region, a two-stage transition occurred: (i) from austenite to the so-called R-phase<sup>2</sup> (A→R) and (ii) subsequently, the transition from R-phase to martensite (R→M). Upon heating, no intermediate R-phase was observed during the reverse transformation from martensite to austenite (M→A). In order to be able to correlate directly the austenite-phase fraction with the stress in the thin film as a function of temperature, only the reverse transformation (M→A) is considered in this paper.

The XRD patterns collected at each temperature step during heating of the NiTi substrate-bound thin films are shown for the first and twentieth cycle in Figure 4.4. At high temperatures ( $T > A_f$ ), additional peaks of cubic  $\text{Ti}_2\text{Ni}$  precipitates become visible, in addition to the cubic austenite reflections. These precipitates, which developed during crystallization of the initially amorphous films (see Section 4.2.1), are present at all temperatures during the M→A transformation, but they are masked by the monoclinic martensite reflections at lower temperatures and in any case represent only a very small volume fraction of the film (as confirmed by Rietveld analysis discussed in Section 4.3.1). No retained (non-transformed) martensite above the austenite finish temperature ( $T > A_f$ ) and no retained austenite below the martensite finish temperature ( $T < M_f$ ) were observed. In total, there are 39 reflections belonging to the three identified phases (M, A, and  $\text{Ti}_2\text{Ni}$ ) in the  $2\theta$  range measured ( $18^\circ$ – $55^\circ$ ).

The reverse transformation does not begin to occur until approximately  $40^\circ\text{C}$  and most of the martensite has transformed to austenite at about  $100^\circ\text{C}$ . Stress has a significant effect on the NiTi martensitic transformation temperature range [26]. Thus, it is expected that the transformation temperatures in the *substrate-bound* film, as indicated above, differ from those measured for the *free-standing* film sections investigated by DSC.

---

<sup>2</sup> The R-phase, whose name is derived from its crystallographic rhombohedral structure, forms during the cooling-induced transformation if the martensite start temperature is relatively low [4].

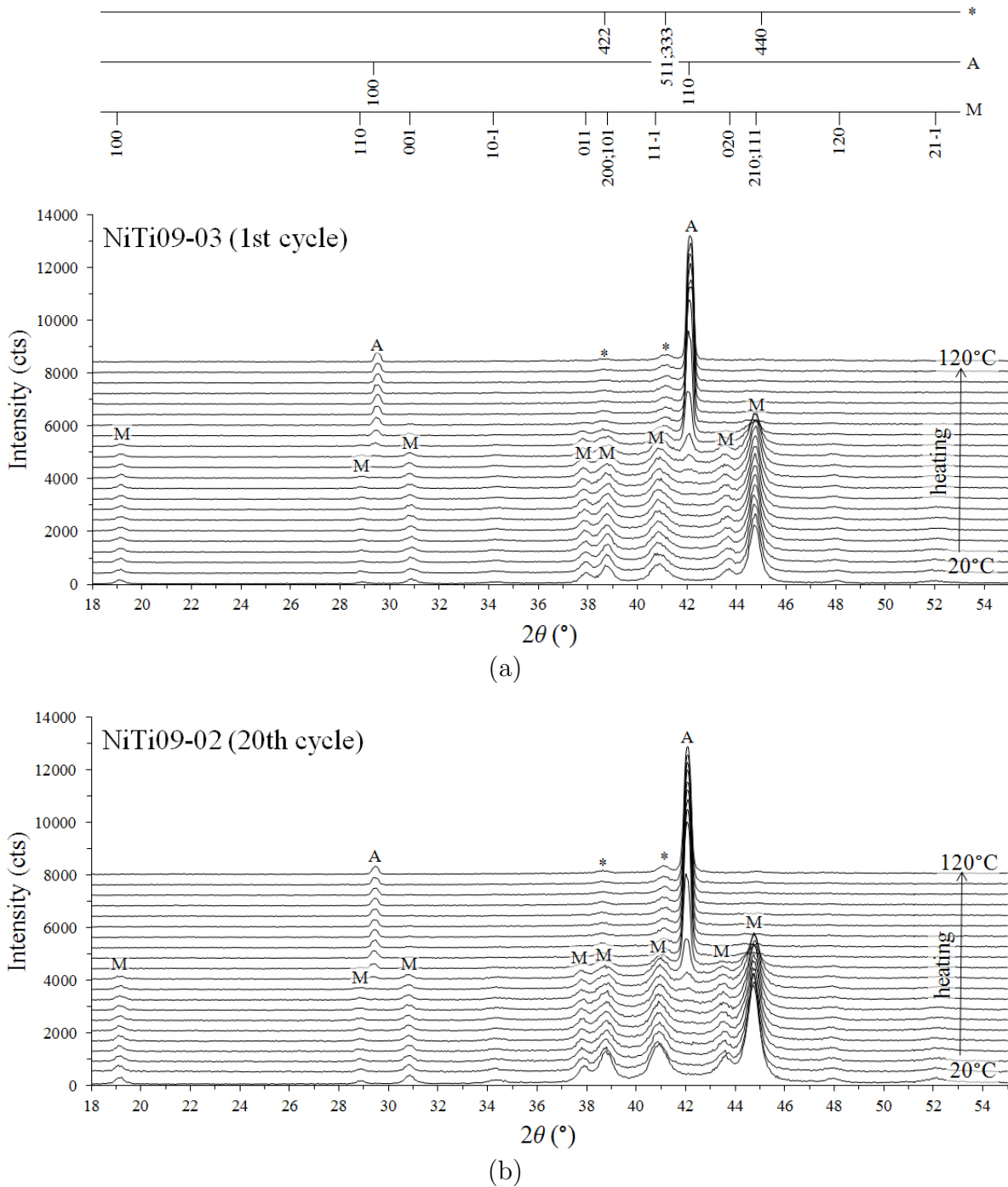


Figure 4.4:  $\theta$ - $2\theta$  scans of the films at different temperatures ranging from 20°C to 120°C throughout the heating portion of the thermal cycle. (a) NiTi09-03 (1st cycle) and (b) NiTi09-02 (20th cycle) (see Table 4.1). The reflections belonging to the austenite (A) and martensite (M) phase have been indicated, as well as those of the Ti<sub>2</sub>Ni precipitates (\*) which can be observed only at high temperatures (see text in the first part of Section 4.3). Note that smaller increments in temperature were taken in the temperature range where the transformation occurs; all measurement temperatures can be found in Table 4.1.

### 4.3.1 Phase fraction, lattice parameters, crystallite size, and microstrain; Rietveld refinements

The  $\theta-2\theta$  scans were analyzed using the GSAS suite of programs [27, 28]. GSAS was applied for this Rietveld refinement because a generalized spherical harmonic description of the orientation distribution function [29] is implemented in it. This is especially important for the analysis of XRD (and neutron) diffraction patterns of textured polycrystalline materials, as is the case here. (See References [30–34].) A Thompson-Cox pseudo-Voigt profile [35] function was used for fitting each of the diffraction lines. The breadths of all peaks were fitted in reciprocal space, for description of the structural broadening, with a constant isotropic (i.e. independent of HKL) Lorentzian size broadening term; for the analysis of the martensite reflections only, an anisotropic (i.e. HKL dependent) Lorentzian strain broadening term [36] was included. The structural broadening contained in the two austenite reflections could be fully conceived due to smallness of the crystallite size. The crystallographic texture in the martensite phase was described subject to cylindrical specimen symmetry (i.e. fiber texture) using 4th order spherical harmonics. The weak (see Section 4.3.2.1) texture in the austenite phase was modeled using the March-Dollase preferential orientation function [37, 38].

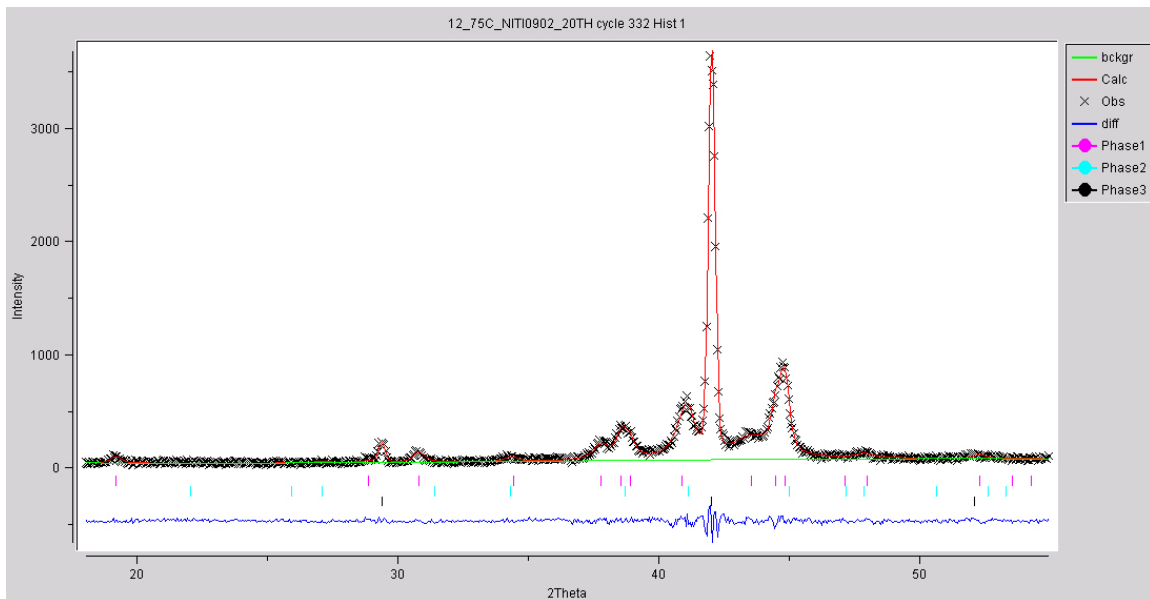


Figure 4.5: Measured XRD pattern and the result of its Rietveld refinement using the GSAS software package; NiTi09-02 specimen, 20th heating cycle,  $T = 75^\circ\text{C}$ ,  $R_{wp} = 9.8\%$

The phase-volume fractions, the background coefficients (the background was described as a Chebyshev polynomial), the profile parameters, the texture parameters, and the lattice parameters were refined simultaneously. The fractional coordinates of the Ni and Ti atoms in the unit cell of the austenite phase (space group  $Pm\bar{3}m$ ) are known and were taken as fixed. The fractional coordinates of the  $B19'$  martensite phase (space group  $P121/m1$ ) were taken from Reference [39], refined in the initial least-square cycles and

then fixed. The fractional coordinates of the  $\text{Ti}_2\text{Ni}$  phase in space group  $Fd\bar{3}m$  were taken from Reference [40] and not refined. The isotropic thermal displacement parameters  $U_{\text{iso}}$  for Ni and Ti were refined but constrained during the least-square refinements to be equal in the martensite and the austenite phases. The isotropic thermal displacement parameters for Ni and Ti in the  $\text{Ti}_2\text{Ni}$  phase were taken equal and fixed at  $U_{\text{iso}} = 0.07 \text{ \AA}^2$ .

The final residuals of the Rietveld refinement,  $R_{wp}$ , are between 6% and 15%. A typical result of Rietveld refinement of an XRD pattern is shown in Figure 4.5. It can be seen that the agreement between the measured and fitted patterns is good.

During heating, martensite and austenite coexist in the temperature range between  $A_s$  and  $A_f$ . The phase-volume fraction of martensite,  $\xi_M$ , and the complementary volume fraction of austenite,  $\xi_A$ , follow from the Rietveld refinements. At temperatures just above  $A_f$ , the austenite fraction is very low, but the Rietveld refinements slightly overestimate it due to a strong correlation of the austenite phase-volume fraction with other profile parameters. The volume fraction of the  $\text{Ti}_2\text{Ni}$  precipitates is very low ( $0.31 \pm 0.15 \text{ vol.}\%$ ), and constant as a function of temperature, so that it can be written:  $\xi_A = 1 - \xi_M$ .

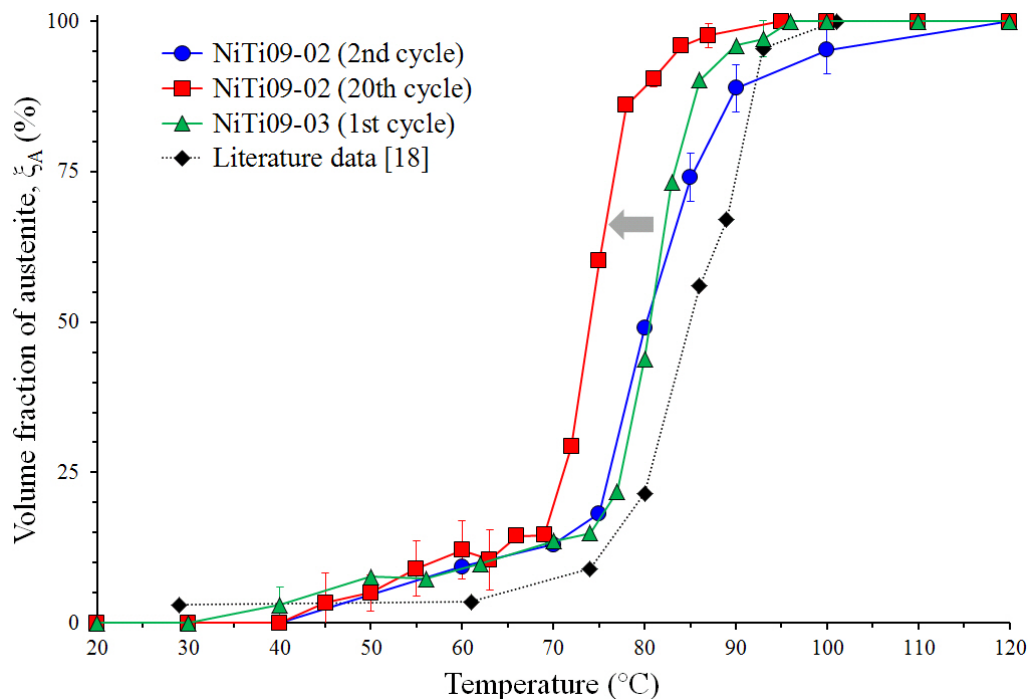


Figure 4.6: Volume fraction of austenite as a function of temperature during the heating portion of the thermal cycle, as determined by Rietveld refinement. For comparison, literature results from Reference [18] for a film with 50.1 at.%Ti are shown as well.

The austenite-volume fraction as a function of temperature is shown in Figure 4.6. At temperatures just above  $A_s$ , the error in the austenite-phase fraction is about  $\pm 5 \text{ vol.}\%$  (see above); at higher temperatures the error is  $\pm 2 \text{ vol.}\%$ . The transformation curves of the NiTi09-02, 1st cycle and of the NiTi09-02, 2nd cycle are very similar, demonstrating (i) the homogeneity of the samples from the same batch and (ii) the reproducibility of the high-temperature XRD measurements. While the transformation curve for the NiTi09-02,

20th cycle is similar in shape to those of the other two experiments (1st and 2nd cycles), it is shifted to lower temperatures. This shift to lower transformation temperatures has been observed before for bulk NiTi shape memory alloys [11] and substrate-bound NiTi thin film [13]. See also Figure 4.7.

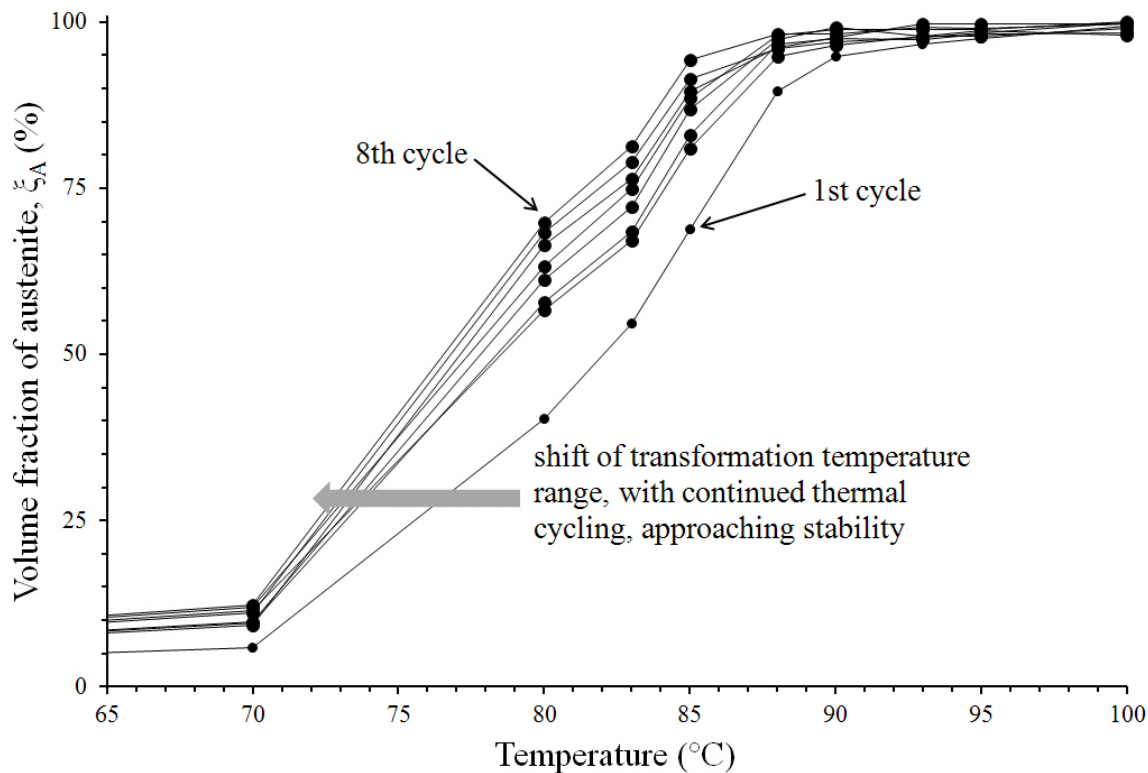


Figure 4.7: Volume fraction of austenite as a function of temperature upon repetitive thermal cycling for film NiTi09-01 (same deposition batch as NiTi09-02 and NiTi09-03).

For the presentation in this figure with the purpose of illustrating the shift of the temperature range for the transformation upon continued cycling, the volume fraction of austenite has been assessed by the integrated intensity of the measured 110 austenite diffraction line (after subtracting the background contribution).

A comparison of the results on austenite-phase fraction obtained in the present project for the NiTi09 film containing 50.8(5) at.%Ti with those obtained for a film containing 50.1 at.%Ti (Reference [18]) can also be made by using Figure 4.6. While the transformation temperatures in the film from Reference [18] are slightly higher, a similar shape is observed for the transformation curve. Note that it is not clear to which thermal cycle the results presented in Reference [18] pertain.

Comparison of the lattice parameters, especially of the martensite phase, with previously published data for NiTi (for example, see [33]) is difficult because the lattice parameters (as taken at  $\psi = \phi = 0^\circ$ ; i.e. Bragg-Brentano geometry) of NiTi depend strongly on composition, thermomechanical history, and the state of stress. (It must be noted here that the above described Rietveld refinements do not account for macroscopic stress/strain in the specimen, which will result in an error in/shift of the calculated lattice parameters.)

The values obtained for the lattice parameters demonstrate that the volume of the unit cells of the martensite phase and the austenite phase increase only slightly with temperature. That said, knowledge of the (strain-free) lattice parameters allows for the calculation of the volume misfit, and thus the transformation strains induced by the phase transformation. (It is recognized that the deviatoric components of the transformation strain tensor are the most important ones [41].) The volume of the monoclinic unit cell is  $V_M = a_M b_M c_M \sin \beta$  (with the lattice parameters of the  $B19'$  unit cell defined as  $a_M$ ,  $b_M$ ,  $c_M$ , and  $\beta$ ); for the cubic unit cell, the volume is simply  $V_A = a_A^3$  (with  $a_A$  as the lattice parameter of the  $B2$  unit cell). The martensite unit cell transforms into the equivalent of two austenite unit cells ( $V_A^* = 2V_A$ ). Thus, the volume misfit strain corresponding with the reverse transformation is given by:

$$\epsilon^{\text{vol.}} = \frac{V_A^* - V_M}{V_M} = \frac{2a_A^3}{a_M b_M c_M \sin \beta} - 1. \quad (4.1)$$

The volumetric strain  $\epsilon^{\text{vol.}}$  describes the unconstrained volume change upon the martensite to austenite transformation. It follows  $\epsilon^{\text{vol.}}$  is about -1%. Due to this volume misfit of the two phases in the film, the austenite (product) phase will experience a tensile stress, while the martensite (parent) phase will be compressively stressed. (Further, see Sections 4.3.2.1 and 4.3.2.2.)

Crystallite sizes can be derived from the isotropic Lorentzian broadening contribution to the structurally broadened line profiles. The corresponding results derived from the Rietveld refinements (adopting isotropic size broadening; see above) demonstrate that the average crystallite size of the martensite phase practically remains constant as a function of temperature (i.e. upon transformation) and equals  $24 \pm 2$  nm for all specimens investigated, unaffected by thermal cycling. Also unaffected by thermal cycling, the average crystallite size of the austenite phase increases from about  $8 \pm 2$  nm at  $60^\circ\text{C}$  up to about  $500 \pm 200$  nm as the temperature approaches the austenite finish temperature ( $A_f$ ), and then, upon further increase of temperature (max:  $120^\circ\text{C}$ ), it remains constant. Since the total thickness of the NiTi thin film is  $2 \mu\text{m}$ , the crystallite-grain growth is *not* constrained by the total thin film thickness. The occurrence of increasing austenite-volume fraction in association with increasing austenite-grain size is compatible with a heterogeneous transformation from martensite to austenite by nucleation and growth of austenite grains [42].

The anisotropic Lorentzian broadening contribution to the structurally broadened line profiles (of the martensite phase) can be used to extract information about the (anisotropic) microstrain (in the martensite phase). The magnitude of the microstrain parallel to the long axis of the microstrain ellipsoid ( $\langle 010 \rangle$  direction) remains approximately constant at 1% until about 20% of the martensite has transformed to austenite, at which point this microstrain component steadily increases and at  $\xi_M = \xi_A = 0.5$ , its value has become approximately 2%. The microstrain in the  $\langle 110 \rangle$  direction is an order

of of magnitude smaller.

The full orientation distribution function cannot be extracted from the XRD data, since measurements were only performed at  $\phi = \psi = 0^\circ$ . However, the strength of the texture of the martensite phase can be indicated by the so-called texture index  $I$ , which represents the sum of the refined spherical harmonic coefficients (see above):  $I = 1$  for an untextured, polycrystalline phase and  $I \rightarrow \infty$  for a strongly textured, polycrystalline phase [29]. The value obtained for  $I$  by Rietveld refinements remains more or less constant for the martensite phase over the entire transformation range ( $I = 1.6 \pm 0.2$ ). Just below the austenite finish temperature  $A_f$ , the texture index for the martensite phase appears to increase: the presence of a state of stress in the film implies that certain variants of the austenite/martensite orientation relationship can be preferred, which results in a reduction of the “randomness” of the orientation distribution, i.e. an increase of the texture index. The texture in the austenite phase is represented by the March-Dollase preferential orientation function (see above); Rietveld refinement of this function demonstrated little effect on the austenite texture as a function of the transformed fraction.

### 4.3.2 Macrostress

The internal stresses induced in substrate-bound thin films during a heating/cooling-induced phase transformation in the film are the result of a superposition of several strain contributions: (i) the thermal strain caused by the difference in thermal expansion coefficients of the phases in the film and the substrate, (ii) the transformation strain due to the volume difference of the product and parent phases in the film, and (iii) a possible plastic strain due to plastic deformation, if the above described thermal and transformation strains cannot be accommodated fully elastically. The transformation induced change of the average, total stress in the film (an average over all phases in the film) is the *recovery stress* as defined in Section 4.1.

The thermal stress resulting from the thermal strain in the substrate-bound NiTi thin film is small: for a temperature change from 20°C to 120°C, the stress due to thermal expansion differences of the film and substrate is of the order of only 50 MPa, whereas stress changes of the order of 300 MPa occur due to the transformation. (See results shown in Section 4.3.2.2.)

#### 4.3.2.1 Stress in austenite; diffraction analysis

The average lattice strain and the corresponding stress in each phase of the film can be determined using the  $\sin^2 \psi$ -method [25]. The lattice strain along the HKL diffraction vector derived from XRD experiments for a given phase is:

$$\epsilon_{\phi, \psi}^{\text{HKL}} = F_{ij}^{\text{HKL}}(\phi, \psi) \cdot \langle \sigma_{ij}^S \rangle, \quad (4.2)$$

where  $F_{ij}^{\text{HKL}}(\phi, \psi)$  are the so-called x-ray stress factors and  $\langle \sigma_{ij}^{\mathcal{S}} \rangle$  describes the total average stress acting on a given phase in the specimen frame of reference [22].

The position of the diffraction lines is used to determine the average lattice strain  $\epsilon_{\phi, \psi}^{\text{HKL}}$ . The x-ray stress factors for a quasi-isotropic aggregate (i.e. macroscopically isotropic despite anisotropic elastic behavior or texture on the microscale) can be replaced by the x-ray diffraction elastic constants [22, 25].

For the thin films investigated in this work, a planar state of stress in the  $(\mathcal{S}_1, \mathcal{S}_2)$  plane of the specimen frame of reference holds:  $\langle \sigma_{13}^{\mathcal{S}} \rangle = \langle \sigma_{23}^{\mathcal{S}} \rangle = \langle \sigma_{33}^{\mathcal{S}} \rangle = 0$  (see further below). For a planar state of stress ( $\langle \sigma_{ij}^{\mathcal{S}} \rangle = 0$  for  $i$  or  $j = 3$ ), and considering cubic crystal symmetry (for austenite), Equation 4.2 simplifies to a linear relationship between the XRD measured average lattice strain  $\epsilon_{\phi, \psi}^{\text{HKL}}$  and  $\sin^2 \psi$ :

$$\begin{aligned} \epsilon_{\phi, \psi}^{\text{HKL}} &= \frac{1}{2} S_2^{\text{HKL}} \cdot [\cos^2 \phi \cdot \langle \sigma_{11}^{\mathcal{S}} \rangle + \sin(2\phi) \cdot \langle \sigma_{12}^{\mathcal{S}} \rangle + \sin^2 \phi \cdot \langle \sigma_{22}^{\mathcal{S}} \rangle] \sin^2 \psi \\ &+ S_1^{\text{HKL}} \cdot [\langle \sigma_{11}^{\mathcal{S}} \rangle + \langle \sigma_{22}^{\mathcal{S}} \rangle]. \end{aligned} \quad (4.3)$$

In order to experimentally calculate each of the components of the stress tensor, measurements at different specimen orientations, i.e. the diffraction angles  $\phi$  and  $\psi$ , are necessary. If the planar state of stress in the material is known (or can be assumed) to be biaxially, rotationally symmetric ( $\langle \sigma_{11}^{\mathcal{S}} \rangle = \langle \sigma_{22}^{\mathcal{S}} \rangle = \langle \sigma_{\parallel} \rangle$  and  $\langle \sigma_{12}^{\mathcal{S}} \rangle = 0$ ), then the relationship between the stress  $\langle \sigma_{\parallel} \rangle$  (defined in the specimen frame of reference) and the average lattice strain along the diffraction vector  $\epsilon_{\phi, \psi}^{\text{HKL}}$  simplifies to:

$$\epsilon_{\phi, \psi}^{\text{HKL}} = \frac{1}{2} S_2^{\text{HKL}} \langle \sigma_{\parallel} \rangle \cdot \sin^2 \psi + 2S_1^{\text{HKL}} \langle \sigma_{\parallel} \rangle. \quad (4.4)$$

For thin films, it is often assumed or validated that the stress state is not only planar, but also biaxially, rotationally symmetric (i.e.  $\langle \sigma_{11}^{\mathcal{S}} \rangle = \langle \sigma_{22}^{\mathcal{S}} \rangle \neq 0$ ; all other stress components zero). In this work, no assumptions about the symmetry of the stress tensor in the  $\mathcal{S}_1, \mathcal{S}_2$  plane will be made *initially*.

In the present study, the lattice strain data were plotted as a function of  $\sin^2 \psi$  (for fixed values of  $\phi$ ). Linear fits (Equation 4.3) were performed to extract a value for the slope, which was in turn used to calculate a value for the average stress in the austenite phase. The XRD elastic constants ( $S_1^{\text{HKL}}$  and  $\frac{1}{2} S_2^{\text{HKL}}$ ) were calculated according to the Eshelby-Kröner grain interaction model [43] using the single-crystal elastic constants for austenite [44]. (The Eshelby-Kröner model was used because it has been demonstrated to accurately match with experimental data for the overall mechanical elastic constants of polycrystalline specimens [45].) The elastic constants were assumed to be independent of thermal cycling. (It has been shown in Reference [46] that, in bulk NiTi specimens, the austenite phase softens only slightly upon cycling.) The crystallographic texture (which in any case is weak as the plots of strain versus  $\sin^2 \psi$  did not show strong curvature, characteristic of highly textured material) was not considered in the calculation of the



Table 4.2: Stress tensor components for the planar stress state for the austenite phase in the NiTi09-02 film (2nd cycle) as determined using the  $\sin^2 \psi$ -method (employing the 110 austenite reflection) as a function of temperature.

$T$ (°C)	$\langle \sigma_{11}^S \rangle^A$ (MPa)	$\langle \sigma_{12}^S \rangle^A$ (MPa)	$\langle \sigma_{22}^S \rangle^A$ (MPa)
80	146±13	11±11	156±12
85	215±12	2±10	223±17
120	256±16	2±4	247±23

diffraction elastic constants.

The individual diffraction lines for the austenite 110 and 310 reflections were fitted with symmetric pseudo-Voigt shape functions, where the peak positions were identified with the fitted peak maxima. The mixing factors of the Gaussian and Lorentzian components, as well as the full width at half maximum (FWHM), of the peaks were not constrained during fitting.

For the first experiment, on the NiTi09-02 film, 2nd cycle, the 110 diffraction line of austenite was measured for a range of  $\psi$  angles between  $0^\circ$  and  $65^\circ$  at  $\phi = 0^\circ, 45^\circ$ , and  $90^\circ$  in order to determine the full planar state of stress ( $\langle \sigma_{11}^S \rangle^A, \langle \sigma_{12}^S \rangle^A, \langle \sigma_{22}^S \rangle^A$ ). The calculated values for the stress tensor components have been gathered in Table 4.2 as a function of temperature. Since  $\langle \sigma_{11}^S \rangle^A \approx \langle \sigma_{22}^S \rangle^A$  and  $\langle \sigma_{12}^S \rangle^A \approx 0$ , it follows that the stress state is biaxially, rotationally symmetric, also in the temperature range (between  $70^\circ$  and  $90^\circ$ ) where the thin film is a mixture of two phases. Therefore, for the (other) experiments (NiTi09-02 film, 20th cycle and NiTi09-03 film, 1st cycle), the 110 and 310 austenite reflections were measured for a range of  $\psi$  angles (between  $0^\circ$  and  $65^\circ$ ) only at  $\phi = 0^\circ$ .

The calculated total stresses in the austenite phase, together with the austenite-phase fraction, are shown in Figure 4.8 for all three experiments as a function of temperature during heating. The stress in austenite increases with increasing temperature up to  $A_f$ , above which the magnitude of the stress remains effectively constant (in the temperature range investigated, i.e. up to  $120^\circ\text{C}$ ). The agreement between the value of stress  $\langle \sigma_{\parallel} \rangle^A$  determined using the 110 and 310 reflections provides support for the validity of the calculated XRD elastic constants ( $S_1^{\text{HKL}}$  and  $\frac{1}{2}S_2^{\text{HKL}}$ ).

Evidently, the stress in the austenite phase is of tensile nature, which can be conceived as a direct consequence of the specific volume difference of austenite and martensite: (i) austenite has a smaller specific volume (see above), (ii) the film is attached to a rigid substrate: a tensile residual state of stress depends upon the martensite to austenite transformation (see also the discussion in Section 4.3.2.3).

The evolution of stress in the austenite phase appears to be related with the development of austenite-phase fraction. This can be interpreted as a consequence of the transformation strain: upon proceeding transformation more and more volume misfit (austenite

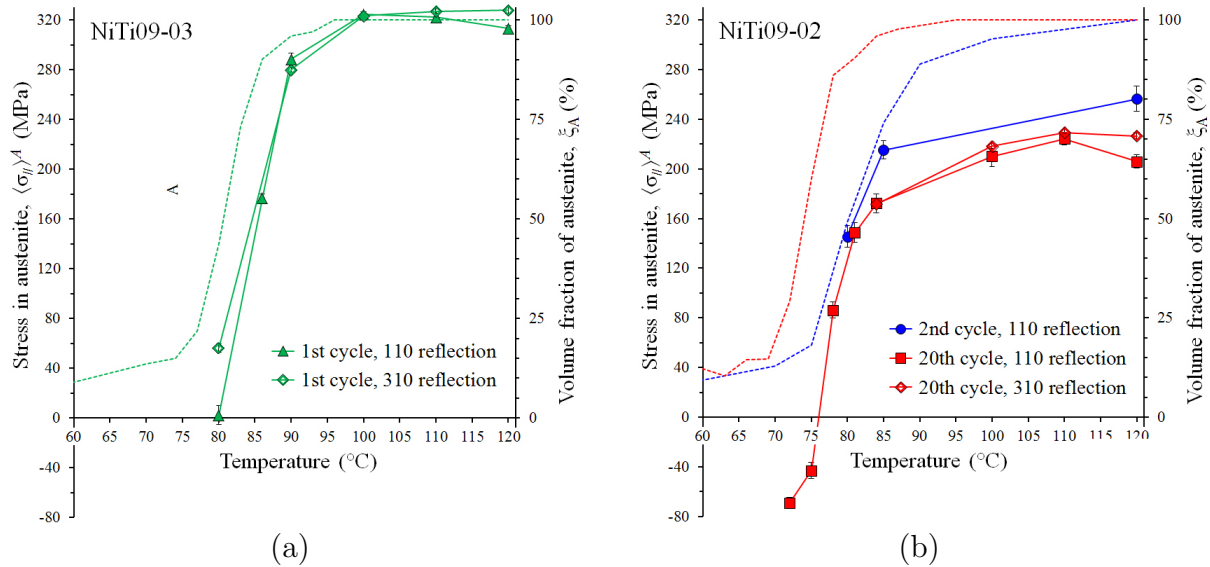


Figure 4.8: Total average stress in the austenite phase  $\langle \sigma_{\parallel} \rangle^A$  (of Equation 4.4) as a function of temperature for the (a) NiTi09-03, 1st cycle (green triangles (110 reflection) and diamonds (310 reflection)) and (b) NiTi09-02, 2nd cycle (blue circles (110 reflection)) and NiTi09-02, 20th cycle (red squares (110 reflection) and diamonds (310 reflection)) experiments. The solid lines are meant as a guide to the eye. The corresponding volume fractions of austenite have been given as dashed lines (see Figure 4.6).

vs. martensite) has to be accommodated. During the forward martensitic phase transformation ( $A \rightarrow M$ ), the accumulation of transformation strains can be accommodated by twinning processes in the martensite (product) phase (see discussion in Section 4.3.2.2). Such a mechanism does not operate during the here considered reverse transformation ( $M \rightarrow A$ ).

#### 4.3.2.2 Overall macroscopic stress in the thin film; curvature measurements

The overall, average macroscopic stress in the NiTi films can be determined from the curvature of the film/substrate system. XRD rocking curves can be utilized to determine the curvature of the thin film/Si single-crystal substrate system during thermal cycling, as follows.

The curvature can be determined from the difference of the peak maximum positions of the Si (substrate) 400 reflection as recorded in rocking curves performed at different locations across the film (Figure 4.3) [47]. A major advantage of this method is that the measurements can be made in parallel with other XRD techniques (such as those discussed in Sections 4.3.1 and 4.3.2.1). The shift in the peak position,  $\Delta\omega$ , and the displacement between two corresponding measurement locations on the film,  $\Delta x$ , are related to the

radius of curvature  $R$  by the following expression [47]:

$$R = \frac{\Delta x}{2 \sin(\frac{\Delta\omega}{2})}. \quad (4.5)$$

The radii of curvature, before and after a certain treatment,  $R_1$  and  $R_2$  (both along the direction of  $\Delta x$ ), respectively, are related to the corresponding difference of film stress  $\langle \Delta\sigma_{\parallel} \rangle^{\text{film}} = \langle \sigma_{\parallel} \rangle_2^{\text{film}} - \langle \sigma_{\parallel} \rangle_1^{\text{film}}$ , along the direction of  $\Delta x$ , in the film by [17]:

$$\langle \Delta\sigma_{\parallel} \rangle^{\text{film}} = M \cdot \frac{H^2}{6h} \cdot \left( \frac{1}{R_2} - \frac{1}{R_1} \right), \quad (4.6)$$

where  $M$  is the biaxial modulus of the Si substrate,  $h$  is the thickness of the film, and  $H$  is the thickness of the substrate. In the present study,  $R_1$  is taken as the curvature of the film/substrate system at high temperature  $T > A_f$ . The absolute value of the stress at  $T < A_f$  follows by taking the stress value in the austenite at  $T > A_f$  (when the film is fully austenitic) as determined by application of the  $\sin^2 \psi$ -method (see Section 4.3.2.1).

The macroscopic film stress, as a function of temperature, determined in this way, is shown in Figure 4.9 for all three experiments, along with the corresponding austenite-phase fraction (see Figure 4.6). Sigmoidal fits for each data set have been provided to demonstrate the trend of the stress as a function of temperature.

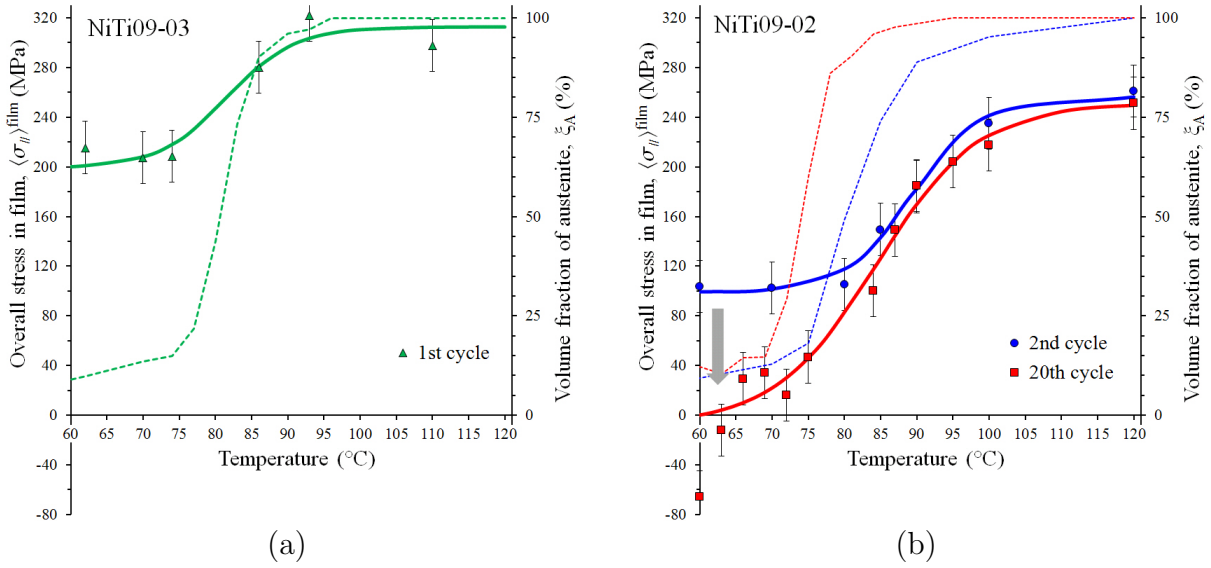


Figure 4.9: Overall, macroscopic stress in the thin NiTi films,  $\langle \sigma_{\parallel} \rangle^{\text{film}}$ , as derived from the curvature of the film/substrate system as a function of temperature (see Equation 4.6 and its discussion) for the: (a) NiTi09-03, 1st cycle (green triangles) and (b) NiTi09-02, 2nd cycle (blue circles) and NiTi09-02, 20th cycle (red squares). The solid lines are sigmoidal fits ( $y = a \cdot (1 + e^{\frac{x-b}{c}})^{-1} + d$ , with  $a$ ,  $b$ ,  $c$ , and  $d$  as fit parameters) of the data only to demonstrate the trend in the stress behavior. The corresponding volume fractions of austenite have been given as dashed lines (see Figure 4.6).

A “lag” in temperature between the developments of the magnitude of the macroscopic

film stress and the transformed fraction of austenite is evident for the data shown in Figure 4.9. It appears that the accommodation of the volume misfit associated with the developing austenite-volume fraction (see Section 4.3.1) becomes more and more difficult as a larger volume fraction of the film has transformed, i.e. the increment of stress per increment of transformation becomes larger for progressing transformation. Note that the martensite phase is more ductile than the austenite phase [48], making the film less compliant upon progressive martensite to austenite transformation.

The magnitude of the *recovery stress* of about 240 MPa (for NiTi09-02, 20th cycle) is smaller than the *recovery stress* measured in the substrate-bound NiTi thin films investigated in References [10] and [18].

The two “early cycle” experiments (NiTi09-03, 1st cycle and NiTi09-02, 2nd cycle) show a rather significant amount of macroscopic stress in the film at room temperature; see Figure 4.9. This indicates that the accommodation process (twinning processes) in the developed martensite (see discussion at the end of Section 4.3.2.1), in the first cycles, are not capable of *fully* relaxing the misfit experienced by the film: the defect structure has to adapt itself during the first cycles (see discussion of Figure 10 in Reference [15]). Upon further thermal cycling, the (self-)accommodation in martensite is capable to realize a zero film stress at room temperature.

Different phenomenological constitutive models for SMA have been proposed in the literature [49, 50]. They all predict that in the presence of external stresses, the transformation curve is shifted to higher temperatures. The observed increase of the tensile stress in the film with temperature means that the reverse transformation is self-retarding. Conversely, this may explain the reduction in the transformation temperatures for the film, after thermal cycling (see Figure 4.6).

### 4.3.2.3 Stress in martensite; mechanical equilibrium of the film

For the NiTi thin films as a two-phase system ( $\xi_A = 1 - \xi_M$ ), the average stress in the martensite phase  $\langle \sigma_{\parallel} \rangle^M$  can be determined from the stress in the austenite phase  $\langle \sigma_{\parallel} \rangle^A$  (as determined from the lattice strain using the  $\sin^2 \psi$ -method; see Section 4.3.2.1) and the overall macroscopic film stress  $\langle \sigma_{\parallel} \rangle^{\text{film}}$  (as determined from the curvature using XRD rocking curves; see Section 4.3.2.2) according to the mechanical equilibrium condition:

$$\xi_A \cdot \langle \sigma_{\parallel} \rangle^A + \xi_M \cdot \langle \sigma_{\parallel} \rangle^M = \langle \sigma_{\parallel} \rangle^{\text{film}}. \quad (4.7)$$

The thus determined phase stress for martensite is shown in Figure 4.10. Note that the data used for determination of  $\langle \sigma_{\parallel} \rangle^A$  and of  $\langle \sigma_{\parallel} \rangle^{\text{film}}$  are independent. Upon progressive martensite to austenite transformation, the phase stress in the martensite increases from zero to tensile values and then decreases thereafter.

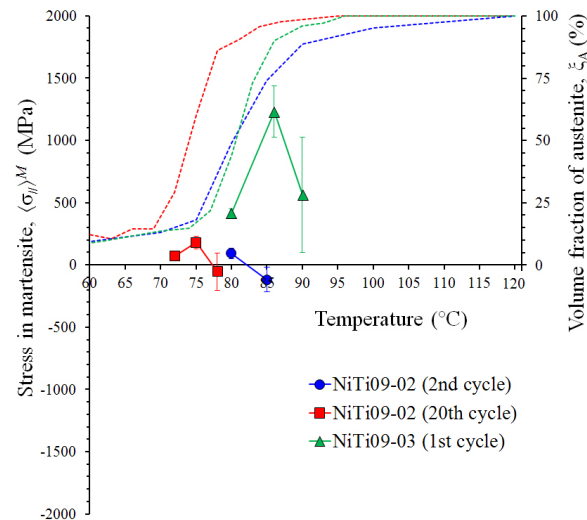


Figure 4.10: Total average stress in the martensite phase  $\langle \sigma_{\parallel} \rangle^M$  (see Equation 4.7) as a function of temperature for NiTi09-03, 1st cycle (green triangles), NiTi09-02, 2nd cycle (blue circles), and NiTi09-02, 20th cycle (red squares) experiments. The solid lines are meant as a guide to the eye. The corresponding volume fractions of austenite have been given as dashed lines (see Figure 4.6).

## 4.4 Conclusions

- The temperature range for the martensite to austenite transformation induced upon heating near-equiatomeric, substrate-bound NiTi thin films shifts to lower temperatures to become stable after about 10–20 thermal cycles (then  $A_s \approx 40^\circ\text{C}$  and  $A_f \approx 80^\circ\text{C}$ ). This is ascribed to the defect structure having to adapt itself so that, upon martensite formation upon cooling, the volume misfit experience can be accommodated fully. An analogous phenomenon is observed for the hcp-fcc transformation in cobalt [15]. Indeed, the macroscopic stress in the fully martensitic film at room temperature becomes nil only upon continued cycling.
- The crystallite size in the parent, martensite phase is small (24 nm) and does not change upon the martensite to austenite transformation. The crystallite size in the product, austenite phase increases from about 8 nm to about 500 nm upon completed transformation, suggesting a heterogeneous transformation by nucleation and growth.
- The microstrain in the parent, martensite phase is strongly anisotropic: in the  $\langle 010 \rangle$  direction it amount to 1% increasing to 2% at 50% transformation, whereas in the  $\langle 110 \rangle$  the microstrain is an order of magnitude smaller.
- The state of macroscopic stress in the developing austenite phase in the film is biaxially, rotationally symmetric and of tensile nature as a consequence of the negative specific volume difference of austenite and martensite (transformation strain).

- The state of stress in the remaining, parent martensite phase in the film increases from zero, i.e. it becomes tensile, and decreases thereafter.
- The evolutions of the overall macroscopic film stress and the volume fraction of austenite do not match: the increment of film stress per increment of transformation increases for progressing transformation.

## Acknowledgements

We are grateful for the permission for measurements at the Synchrotron Light Source ANKA at the MPI-IS beamline for Surface Diffraction. We thank Dr. M. Mantilla, Dipl.-Ing. S. Kurz, and Dr. A. Sharma for assistance during these measurements. The authors also thank Dr. U. Welzel for discussions and advice at the initial stage of this project, Mr. V. Reinhart for assistance with the sputter-deposition of the thin film specimens, Mrs. M. Dudek for assistance with preparation of substrates prior to deposition, and M. Sc. K. M. Gadomska for performing SEM on the thin film specimens.

# Bibliography

- [1] W. L. Bernard, H. Kahn, A. H. Heuer, and M. A. Huff, “A titanium-nickel shape-memory alloy actuated micropump,” *Transducers '97*, 1997.
- [2] B. K. Lai, G. Hahm, L. You, C.-L. Shih, H. Kahn, S. M. Phillips, and A. H. Heuer, “The characterization of the TiNi shape-memory actuated microvalves,” *Material Research Society Symposium Procedures*, vol. 657, pp. 1–6, 2001.
- [3] A. P. Lee, D. R. Ciarlo, P. A. Krulevitch, S. Lehew, J. Trevino, and M. A. Northrup, “A practical microgripper by fine alignment, eutectic bonding and SMA actuation,” *Sensor Actuators A*, vol. 54, pp. 755–759, 1996.
- [4] S. Miyazaki, Y. Q. Fu, and W. M. Huang, *Thin Film Shape Memory Alloys: Fundamentals and Device Applications*. Cambridge University Press, 1st ed., 2009.
- [5] Y. Q. Fu, S. Zhang, M. J. Wu, W. M. Huang, H. J. Du, J. K. Luo, A. J. Flewitt, and W. I. Milne, “On the lower thickness boundary of sputtered TiNi films for shape memory application,” *Thin Solid Films*, vol. 515, no. 1, pp. 80–86, 2006.
- [6] T. Duerig, A. R. Pelton, and C. Trepanier, *Nitinol*. ASM International, 2011.
- [7] Y. Q. Fu and H. J. Du, “Effects of film composition and annealing on residual stress evolution for shape memory TiNi film,” *Materials Science & Engineering A*, vol. A342, pp. 236–244, 2003.
- [8] S. K. Sharma, H. S. Vijaya, and S. Mohan, “Influence of substrate temperature and deposition rate on structural and mechanical properties of shape memory NiTi films,” *Physics Procedia*, vol. 1, pp. 44–51, 2010.
- [9] X. Huang and Y. Lui, “Some factors affecting the properties of sputter deposited NiTi-based shape memory alloy thin films,” *Proceedings of the SPIE*, vol. 4934, pp. 210–218, 2002.
- [10] Y. Q. Fu and H. J. Du, “Relaxation and recovery of stress during martensitic transformation for sputtered shape memory TiNi film,” *Surface and Coatings Technology*, vol. 153, pp. 100–105, 2002.

- [11] J. Kwarciak, Z. Lekston, and H. Morawiec, "Effect of thermal cycling and  $\text{Ti}_2\text{Ni}$  precipitation on the stability of the Ni-Ti alloys," *Journal of Materials Science*, vol. 22, pp. 2341–2345, 1987.
- [12] N. B. Morgan and C. M. Friend, "A review of shape memory stability in NiTi alloys," *Journal de Physique IV*, vol. 11, no. PR8, pp. 325–332, 2001.
- [13] J. Schaab, "X-ray diffraction analysis of shape-memory transformation under load in Ni-Ti thin films." Diploma thesis, 2012.
- [14] M. Pattabi, K. Ramakrishna, and K. K. Mahesh, "Effect of thermal cycling on the shape memory transformation behavior of NiTi alloy: Powder X-ray diffraction study," *Materials Science & Engineering A*, vol. 448, pp. 33–38, 2007.
- [15] R. Bauer, E. A. Jäggle, W. Baumann, and E. J. Mittemeijer, "Kinetics of the allotropic hcp-fcc phase transformation in cobalt," *Philosophical Magazine*, vol. 91, no. 3, pp. 437–457, 2011.
- [16] L. B. Freund and S. Suresh, *Thin Film Materials: Stress, Defects Formation and Surface Evolution*. Cambridge University Press, 2003.
- [17] G. Stoney, "The tension of metallic films deposited by electrolysis," *Proceedings of the Royal Society*, vol. A82, pp. 172–175, 1909.
- [18] B.-K. Lai, H. Kahn, S. M. Phillips, Z. Akase, and A. H. Heuer, "Quantitative phase transformation behavior in TiNi shape memory thin films," *Journal of Materials Research*, vol. 19, no. 10, pp. 2822–2833, 2004.
- [19] S. Kustov, D. Salas, R. Santamarta, E. Cesari, and J. van Humbeeck, "Isothermal and athermal martensitic transformation in the B2-R-B19' sequence in Ni-Ti shape memory alloys," *Scripta Materialia*, vol. 63, no. 12, pp. 1240–1243, 2010.
- [20] J. D. Busch, A. D. Johnson, C. H. Lee, and D. A. Stevenson, "Shape-memory properties in Ni-Ti sputter-deposited film," *Journal of Applied Physics*, vol. 68, no. 12, pp. 6224–6228, 1990.
- [21] J. A. Thornton, "Influence of apparatus geometry and depositions conditions on structure and topography of thick sputtered coatings," *Journal of Vacuum Science and Technology*, vol. 11, no. 4, pp. 666–670, 1974.
- [22] U. Welzel and E. J. Mittemeijer, "Diffraction stress analysis of macroscopically elastically anisotropic specimens: On the concepts of diffraction elastic constants and stress factors," *Journal of Applied Physics*, vol. 93, no. 11, pp. 9001–9011, 2003.
- [23] J. F. Nye, *Physical Properties of Crystals*. Oxford University Press, 1957.



- [24] C. Giacovazzo, H. L. Monaco, G. Artioli, D. Viterbo, G. Ferraris, G. Gilli, G. Zanotti, and M. Catti, *Fundamentals of Crystallography*. Oxford University Press, 2nd edition, ed., 2002.
- [25] U. Welzel, J. Ligot, P. Lamparter, A. C. Vermeulen, and E. J. Mittemeijer, “Stress analysis of polycrystalline thin films and surface regions by X-ray diffraction,” *Journal of Applied Crystallography*, vol. 38, pp. 1–29, 2005.
- [26] L. C. Brinson, “One-dimensional constitutive behavior of shape memory alloys: thermomechanical derivation with non-constant material functions and redefined martensite internal variable,” *Journal of Intelligent Material Systems and Structures*, vol. 4, pp. 229–242, 1993.
- [27] A. C. Larson and R. B. V. Dreele, “General Structure Analysis System (GSAS),” *Los Alamos National Laboratory Report LAUR*, pp. 86–748, 2005.
- [28] B. H. Toby, “EXPGUI, a graphical user interface for GSAS,” *Journal of Applied Crystallography*, vol. 34, pp. 210–213, 2001.
- [29] H.-J. Bunge, *Texture Analysis in Material Science*. Butterworth, 1982.
- [30] H. Sitepu, W. W. Schmahl, and R. B. von Dreele, “Use of the generalized spherical harmonic model for describing crystallographic texture in polycrystalline NiTi shape-memory alloy with time-of-flight neutron powder diffraction data,” *Applied Physics Letters A*, vol. 74, pp. S1676–S1678, 2002.
- [31] H. Sitepu, W. W. Schmahl, J. K. Allafi, G. Eggeler, A. Dlouhy, D. M. Toebbens, and M. Tovar, “Neutron diffraction phase analysis during thermal cycling of a Ni-rich NiTi shape memory alloy using the Rietveld method,” *Scripta Materialia*, vol. 46, no. 7, pp. 543–548, 2002.
- [32] H. Sitepu, W. W. Schmahl, T. Reinecke, J. K. Allafi, and G. Eggeler, “Phase fractions of B2, B19', R-phase and Ni<sub>4</sub>Ti<sub>3</sub> in NiTi alloys during two-step phase transformations,” *Journal de Physique IV*, vol. 112, pp. 677–680, 2003.
- [33] J. Khalil-Allafi, W. W. Schmahl, M. Wagner, H. Sitepu, D. M. Toebbens, and G. Eggeler, “The influence of temperature on lattice parameters of coexisting phases in NiTi shape memory alloys - a neutron diffraction study,” *Materials Science & Engineering A*, vol. 378, pp. 161–164, 2004.
- [34] M. L. Young, M. F. X. Wagner, J. Frenzel, W. W. Schmahl, and G. Eggeler, “Phase volume fraction and strain measurements in an ultrafine-grained NiTi shape-memory alloy during tensile loading,” *Acta Materialia*, vol. 58, pp. 2344–2354, 2010.
- [35] A. M. Hindeleh and D. J. Johnson, “Crystallinity and crystallite size measurement in cellulose fibres: 1. Ramie and Fortisan,” *Polymer*, vol. 13, no. 9, pp. 423–430, 1972.

- [36] E. J. Mittemeijer and U. Welzel, eds., *Chapter 4 in Modern Diffraction Methods*. Wiley, 2012.
- [37] A. March, “Mathematical theory on regulation according to the particle shape in affine deformation,” *Zeitschrift für Kristallographie*, vol. 81, pp. 285–297, 1932.
- [38] W. A. Dollase, “Corrections of intensities for preferred orientation in powder diffraction - application of the March model,” *Journal of Applied Crystallography*, vol. 19, pp. 267–272, 1986.
- [39] Y. Kudoh, M. Tokonami, S. Miyazaki, and K. Otsuka, “Crystal structure of the martensite in Ti-49.2% alloy analyzed by the single crystal X-ray diffraction method,” *Acta Metallurgica*, vol. 33, pp. 2049–2056, 1985.
- [40] S. Sridharan, H. Nowotny, and S. F. Wayne, “Investigations within the quaternary system Ti-Ni-Al-C,” *Monatshefte für Chemie und verwandte Teile anderer Wissenschaften*, vol. 114, pp. 127–135, 1983.
- [41] S. C. Mao, L. F. Luo, Z. Zhang, M. H. Wu, Y. Liu, and X. D. Han, “EBSD studies of the stress-induced  $B2$ - $B19'$  martensitic transformation in NiTi tubes under uniaxial tension and compression,” *Acta Materialia*, vol. 58, no. 9, pp. 3357–3366, 2010.
- [42] E. J. Mittemeijer, *Fundamentals of Materials Science*. Springer, 2011.
- [43] G. Kneer, “Über die Berechnung der Elastizitätsmoduln vielkristalliner Aggregate mit Textur,” *Physica Status Solidi*, vol. 9, no. 39, pp. 825–838, 1965.
- [44] T. M. Brill, S. Mittelbach, W. Assmus, M. Mullner, and B. Luthi, “Elastic properties of NiTi,” *Journal of Physics: Condensed Matter*, vol. 3, no. 48, pp. 9621–9627, 1991.
- [45] U. Welzel, M. Leoni, and E. J. Mittemeijer, “The determination of stresses in thin films; modelling elastic grain interaction,” *Philosophical Magazine*, vol. 83, no. 5, pp. 603–630, 2003.
- [46] C. Urbina and S. De la Flor, “Effect of thermal cycling on the thermomechanical behaviour of NiTi shape memory alloys,” *Materials Science & Engineering A*, vol. 501, pp. 197–206, 2009.
- [47] A. Segmüller, I. C. Noyan, and V. S. Speriosu, “X-ray diffraction studies of thin films and multilayer structures,” *Progress in Crystal Growth and Characterization of Materials*, vol. 18, pp. 21–66, 1989.
- [48] X. Ren, N. Miura, J. Zhang, K. Otsuka, K. Tanaka, M. Koiwa, T. Suzuki, and Y. I. Chumlyakov, “A comparative study of elastic constants of Ti-Ni-based alloys prior to martensitic transformation,” *Materials Science & Engineering A*, vol. 312, no. 1–2, pp. 196–206, 2001.

- 
- [49] K. Malukhin and K. Ehmann, “A model of the kinetics of the temperature-induced phase transformation in NiTi alloys and its experimental verification,” *Journal of Intelligent Material Systems and Structures*, vol. 23, pp. 35–44, 2011.
- [50] L. C. Brinson, A. Bekker, and S. Hwang, “Deformation of shape memory alloys due to thermo-induced transformation,” *Journal of Intelligent Material Systems and Structures*, vol. 7, no. 1, pp. 97–107, 1996.



# Chapter 5

## Summary

Externally or internally applied stresses and strains can pronouncedly influence material properties. Hence, the role of stress on material behavior is an important and developing field of research. Variations in stress throughout a material can lead to either strengthening or weakening of a specimen or engineering component. A clear understanding of stress and strain, and the ability to predict the magnitude of its variation, in a material (as a function of material processing), in the absence and presence of external loading, is of utmost importance to optimize material properties.

### Lattice-strain variation upon elastic loading of polycrystals

Lattice-strain variation in massive, polycrystalline aggregates provides a wealth of information about the grain interaction in an externally loaded specimen. Each grain within the body is confined by its neighbors, and the compliance of these neighboring bodies provides the extent to which a grain in a massive polycrystalline body may deform under loading. As single crystals (with tungsten being an exception) are intrinsically elastically anisotropic, the direction of the applied loading with respect to the grain's crystallographic orientation must also be considered.

Three categories of strain variation may be present in an elastically loaded polycrystalline aggregate: (i) macro-, (ii) meso-, and (iii) microvariation in strain.

- (i) *Macrovariation* in strain is the variation of the average lattice strain, taken for the groups of diffracting grains, that occurs upon changing the orientation of the diffraction vector with respect to the specimen frame of reference.
- (ii) *Mesovariation* in strain is the variation of the average lattice strain, the average now taken per diffracting grain, for the group of diffracting grains sharing a fixed orientation of the diffraction vector.
- (iii) *Microvariation* in strain is the variation of lattice strain within an individual grain.

Various elastic grain-interaction models can be used to approximate the average lattice strain within a crystallite based on its orientation with respect to the aggregate and

the external loading. Each of these grain-interaction models is based on its own set of assumptions for the grain interaction. (See Table 2.1 in Chapter 2 for details on each of the discussed elastic grain-interaction models.) Two main categories of grain interaction can be defined: (i) isotropic grain interaction, where the interactions of the grains in all directions adhere to the same assumptions, and (ii) anisotropic grain interaction, where, conversely, the interactions of the grains do not adhere to the same assumptions in all directions.

The applicability of each set of grain-interaction assumptions (e.g. the individual grain-interaction model) is highly dependent on the specimen and the loading conditions. One shortcoming of the elastic grain-interaction models is that all grains of the same crystallographic orientation are considered to experience identical (average) lattice strains. Also, the lattice-strain variation within an individual grain cannot be calculated according to the models. Hence, these models only calculate approximate solutions for the *macrovariation* of strain and a portion of the *mesovariation* of strain, not taking into account any strain variation induced by local heterogeneities in the neighborhood around the individual crystallites. Therefore, the elastic grain-interaction models provide only an *underestimate* of the total strain variation in a loaded, polycrystalline body.

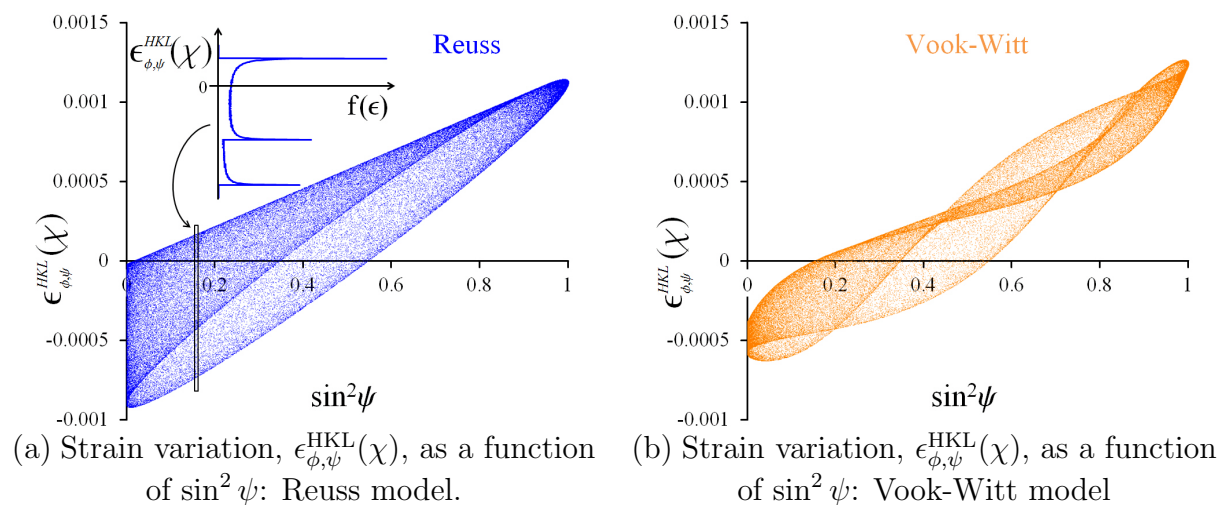


Figure 5.1: Strain variation,  $\epsilon_{\phi,\psi}^{\text{HKL}}(\chi)$  at  $\phi = 0^\circ$  for variable  $\psi$  using the Reuss and Vook-Witt grain-interaction models for the 331 reflection of an untextured Au aggregate under uniaxial tensile loading along the  $\mathcal{S}_1$  axis ( $\sigma_{11} = 100$  MPa). The inset in (a) shows the frequency of strain  $f(\epsilon)$  within the set of grains sharing a common diffraction vector orientation (e.g. fixed  $\phi$  and  $\psi$ ).

In Chapter 2, the lattice-strain variation according to several elastic grain-interaction models is calculated. The influence of parameters such as the state of stress, the magnitude of applied stress, and the crystallographic texture, to name a few, are studied. The lattice-strain variation for the 331 reflection of an untextured gold aggregate calculated according to the Reuss and Vook-Witt models plotted as a function of specimen tilt angle can be seen in Figure 5.1. While such models have been shown to be quite reliable for

calculating the average lattice strain in polycrystalline aggregates under elastic loading, it is concluded here that consideration of the local heterogeneity surrounding each individual grain is necessary to approximate the full extent of lattice-strain variation in an elastically loaded quasi-isotropic aggregate. According to finite element calculations used to approximate the *mesovariation* of strain and *microvariation* of strain, the lattice-strain variation according to the discussed grain-interaction models can underestimate the total variation of strain to the order of 50%.

Whereas the *position* of diffraction lines is directly related to the average lattice spacing of a set of  $hkl$  planes, variations in this lattice spacing (e.g. variation in the lattice strain) will lead to *broadening* of measured diffraction lines for the elastically loaded polycrystalline aggregate. The strain variation calculated according to elastic grain-interaction models can also be applied to approximate the diffraction-line broadening induced by the applied load (and corresponding lattice-strain variation). Analysis of lattice-strain induced diffraction-line broadening can provide much more direct and detailed information on the type of operating grain interactions, than as obtained from “standard” diffraction stress analysis on the basis of diffraction-line positions, e.g. by the so-called  $\sin^2 \psi$ -method.

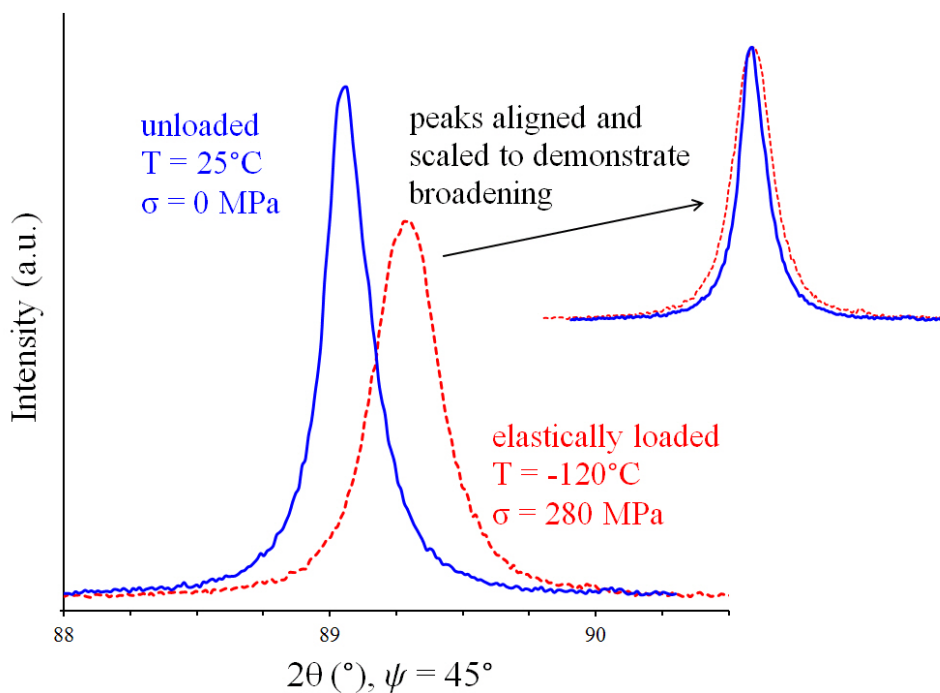


Figure 5.2: The loading induced (peak shift and) broadening of the 311 reflection recorded for a Cu thin film (at tilt angle of  $\psi = 45^{\circ}$ ; radiation  $\lambda = 1.52933 \text{ \AA}$ ). The state of biaxially rotationally symmetric tensile stress (280 MPa) was imposed by cooling to  $-120^{\circ}\text{C}$ . The inset reveals the difference in broadening for loaded and unloaded states by scaling and shifting the peak maximum positions, such that the peak maxima coincide.

The investigation discussed in Chapter 3 provides a detailed account of synchrotron experiments where the diffraction lines of various elastically loaded specimens were measured as an indication of lattice-strain variation within the material, as shown in Figure 5.2.

Comparisons between experimental data and elastic grain-interaction calculations provided information about the extent of applicability of the discussed models. The measured diffraction-line broadening induced by elastic loading greatly exceeds that predicted by any of the discussed elastic grain-interaction models.

The experimental measurements further demonstrated that the strain variation (as observed by the broadening of diffraction lines) induced by elastic loading of a polycrystalline aggregate cannot be fully accounted for by the elastic grain-interaction models. In contrast to the predictions from the isotropic grain-interaction models (which calculate no lattice-strain variation in cubic materials) for the  $H00$  and  $HHH$  reflections, diffraction-line broadening of such reflections was experimentally observed in the elastically loaded specimens. The discrepancy in the magnitude of broadening (and, in turn, strain variation) is clearly an indication that the magnitude of *mesovariation* of strain and *microvariation* of strain not calculated by the grain-interaction models is significant. Thus, the experimental method also provides a sensitive means to study the actual grain interactions (and magnitude of variation in strain) occurring in a specimen.

## Stress development upon austenite-martensite phase transformation in equiatomic NiTi thin films

Near equiatomic compositions of NiTi are shape memory alloys, which are characterized by two unique behaviors: pseudoelasticity (also called super elasticity) and shape memory effect. These material properties make NiTi thin films a prime candidate for application in microelectromechanical systems (MEMS). The two prominent phases of interest in near equiatomic NiTi are a high temperature (cubic) austenite and a low temperature (monoclinic) martensite. Film deposition method, the stress state in the film, and material composition are known to significantly influence the transformation behavior of the material. Thermal loading (i.e. heating) can be used to induce the reverse martensitic phase transformation (from martensite to austenite).

Due to the abrupt structural transition associated with the phase transformation, the material lends itself well to investigation via x-ray diffraction (XRD) techniques. Diffraction line-profile analysis of XRD patterns during such *in situ* experiments is a powerful tool. The study in Chapter 4 focuses on synchrotron XRD experiments of substrate-bound NiTi thin films (49.2(5) at.%Ni) during *in situ* heating. Through *in situ* high temperature XRD measurements, experiments have been performed to track the phase fraction, stress, and crystallite size of the phases during the transformation. A combination of XRD techniques were applied for the investigation to measure the phase fraction (Rietveld analysis, Figure 5.3) and stresses (curvature and  $\sin^2\psi$  methods) as a function of temperature. Measurements of similar samples demonstrated good reproducibility.

Upon continued thermal cycling, the phase transformation temperatures of the material change, shifting to lower values, which can be seen in Figure 5.3. This transient behavior



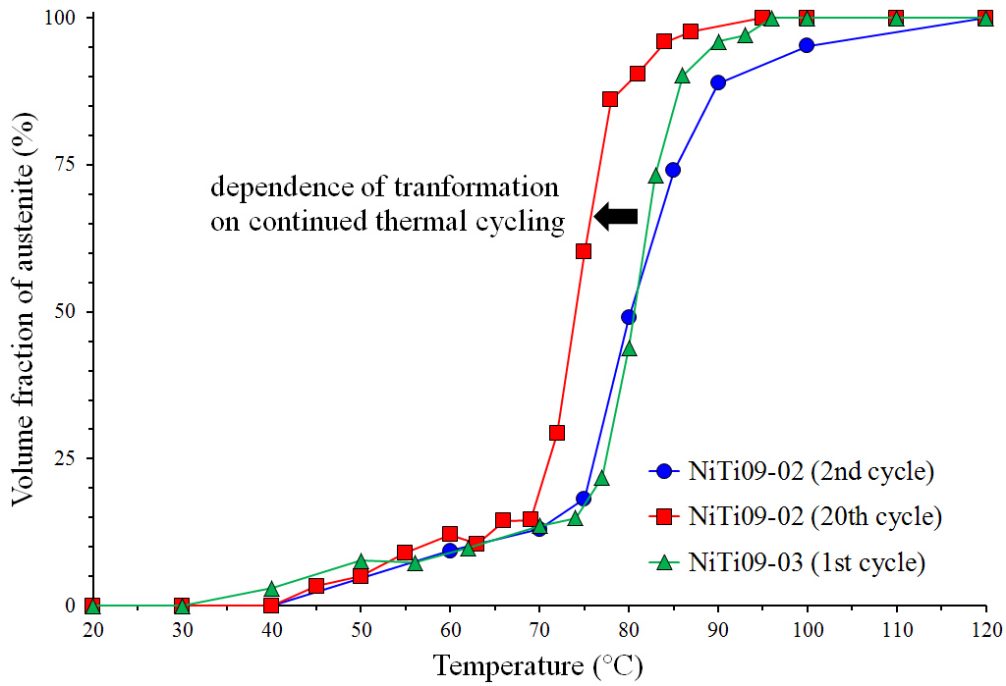


Figure 5.3: Phase fraction of austenite as a function of temperature during heat cycling determined from Rietveld analysis.

is thought to originate from an increase in the density of defects and dislocations. For the forward transformation, this results in a higher degree of undercooling necessary for the transformation to proceed. The stress state in the film is also affected by thermal cycling. After numerous thermal cycles, the magnitude of the macroscopic stress in the film at room temperature (single-phase film in martensite phase) reduces to (practically) zero, demonstrating the “self-accommodating” nature of the martensite microstructure.

The macroscopic film stress was observed to increase with temperature. The stresses pertaining to the individual phases were separated, demonstrating that the magnitude of stress is highly dependent on the phase fraction of austenite in the substrate-bound NiTi thin film. Despite increasing in magnitude, the stress in the austenite phase remains biaxially, rotationally symmetric throughout the entire transformation.



## Chapter 6

# Zusammenfassung

Die Beschreibung der Einflussfaktoren von mechanischen Spannungen auf das Materialverhalten stellt einen wichtigen und sich rasant entwickelnden Bereich der Forschung dar. Deren Auswirkungen bestimmen wesentlich sowohl grundlegende Materialeigenschaften als auch Phänomene wie z.B. Phasenumwandlungen. Spannungsinhomogenitäten innerhalb des Materials können entweder zur Stärkung oder aber Schwächung einer Probe oder eines Bauteils führen. Einerseits ist es wichtig, Spannung und Dehnung im Material zu verstehen, andererseits ist die Fähigkeit nötig, die genaue Amplitude der Variation der Dehnung im Material vorherzusagen.

### Variation der Gitterdehnung in massiven polykristallinen Probekörpern unter Belastungen

Kenntnis und Deutung der Variation der Gitterdehnung in massiven polykristallinen Probekörpern beinhalten eine Fülle von Informationen über die Wechselwirkungen der Körner. Jedes einzelne Korn inmitten eines Körpers wird durch die Beschaffenheit seiner Nachbarkörner eingeschränkt und in seiner möglichen Verformung unter Belastung behindert. Da Einkristalle, mit der Ausnahme von Wolfram, intrinsisch elastisch anisotrop sind, ist die Richtung der angelegten Spannung hinsichtlich der kristallographischen Orientierung der Körner zu berücksichtigen.

Drei Arten von Dehnungsvariation können in einem elastisch beanspruchten polykristallinen Körper vorhanden sein:

- (i) *Makrovariation* der Dehnung ist die Variation der durchschnittlichen Gitterdehnung (von der Gruppe der an der Beugung beteiligten Körner), die beim Wechsel der Ausrichtung des Beugungsvektors zum *Specimen*-Bezug entsteht.
- (ii) *Mesovariation* der Dehnung ist die Variation der durchschnittlichen Gitterdehnung (von dem an der Beugung beteiligten Korn) in der Gruppe der an der Beugung beteiligten Körner mit derselben Orientierung des Beugungsvektors.
- (iii) *Mikrovariation* der Dehnung ist die Variation der Gitterdehnung innerhalb eines

einzelnen Korn.

Verschiedene Modelle der elastischen Wechselwirkung zwischen den Körnern können benutzt werden, um die durchschnittliche Gitterdehnung innerhalb der Kristallite zu berechnen, basierend auf deren Orientierung in Bezug auf eine Gruppe von Körnern und auch auf die äußere Belastung. Jedes dieser Modelle beruht auf einem individuellen Gerüst von Annahmen für die Wechselwirkung zwischen den Körnern. (Siehe dazu Table 2.1 in Chapter 2 für Einzelheiten zu den diskutierten Modellen.) Zwei Hauptkategorien der Wechselwirkungen können definiert werden: (i) isotrope Interaktion zwischen den Körnern, in denen die Wechselwirkungen der Körner richtungsunabhängig denselben Annahmen entsprechen, und (ii) anisotrope Kornwechselwirkung, in denen die Wechselwirkungen der Körner abhängig von der Richtung sind und somit nicht denselben Annahmen entsprechen.

Die Anwendbarkeit der jeweiligen Annahmen der Korn zu Korn Wechselbeziehung (z.B. die individuellen Kornwechselwirkungsmodelle) ist stark abhängig von der Probe und dem jeweiligen Belastungszustand. Eine Unzulänglichkeit der elastischen Kornwechselwirkungsmodelle ist die Annahme, dass alle Körner mit der gleichen Kristallorientierung identische (durchschnittliche) Gitterdehnungen erfahren. Außerdem kann die Variation der Gitterdehnung eines individuellen Kornes nicht mit den Modellen berechnet werden. Das bedeutet, dass diese Modelle weder den gesamten Beitrag zur *Meso-variation* der Gitterdehnung noch die *Mikrovariation* der Gitterdehnung berücksichtigen. Deshalb geben diese Modelle eine zu geringe Dehnungsvariation in einem beanspruchten polykristallinen Körper an.

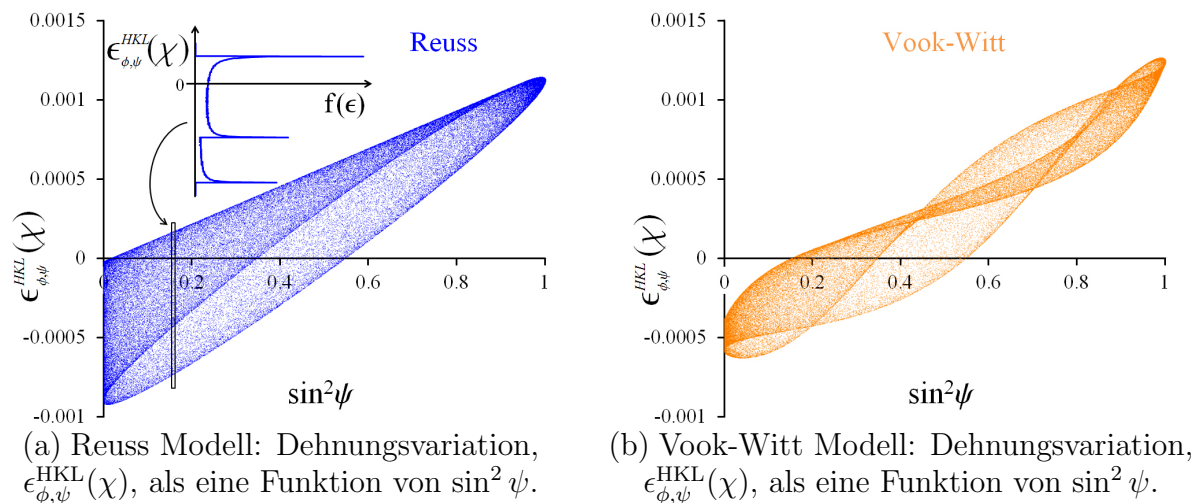


Figure 6.1: Dehnungsvariation,  $\epsilon_{\phi,\psi}^{\text{HKL}}(\chi)$  bei  $\phi = 0^\circ$  für den Winkel  $\psi$  mit den Reuss and Vook-Witt Kornwechselwirkungsmodellen für die 331 Reflexion eines polykristallinen Au Körpers unter uniaxialer Zugbelastung entlang der  $S_1$  Achse ( $\sigma_{11} = 100$  MPa). Das eingeschobene Bild in (a) zeigt die Frequenz der Dehnung  $f(\epsilon)$  innerhalb einer Gruppe von Körnern, die den gleichen Beugungsvektor teilen (d.h. die Winkel  $\phi$  und  $\psi$  sind unveränderlich).

In Chapter 2 ist die Variation der Gitterdehnung mittels mehreren elastischen Kornwechselwirkungsmodellen berechnet. Der Einfluss von Parametern wie dem Spannungszustand, der Höhe der angelegten Spannung und der kristallographischen Struktur wurden untersucht. Die Gitterdehnungsvariation, die mit den Reuss und Vook-Witt Kornwechselwirkungsmodellen berechnet ist, ist für die 331 Reflexion eines polykristallinen Au Köpers in Figure 6.1 dargestellt. Während sich solche Modelle zur Berechnung der durchschnittlichen Gitterdehnung in polykristallinen Proben bei elastischen Belastungen als zuverlässig erwiesen haben, wird gefolgert, dass die lokale Heterogenität um jedes einzelne Korn in Betracht gezogen werden muss, um die komplette Variation der Gitterdehnung in einem elastisch quasi-isotropen Material zu nähern. Finite-Elemente Berechnungen zeigen, dass die berechnete Variation der Gitterdehnung, die aus den Kornwechselwirkungsmodellen stammen, um bis zu 50% unterschätzt wird.

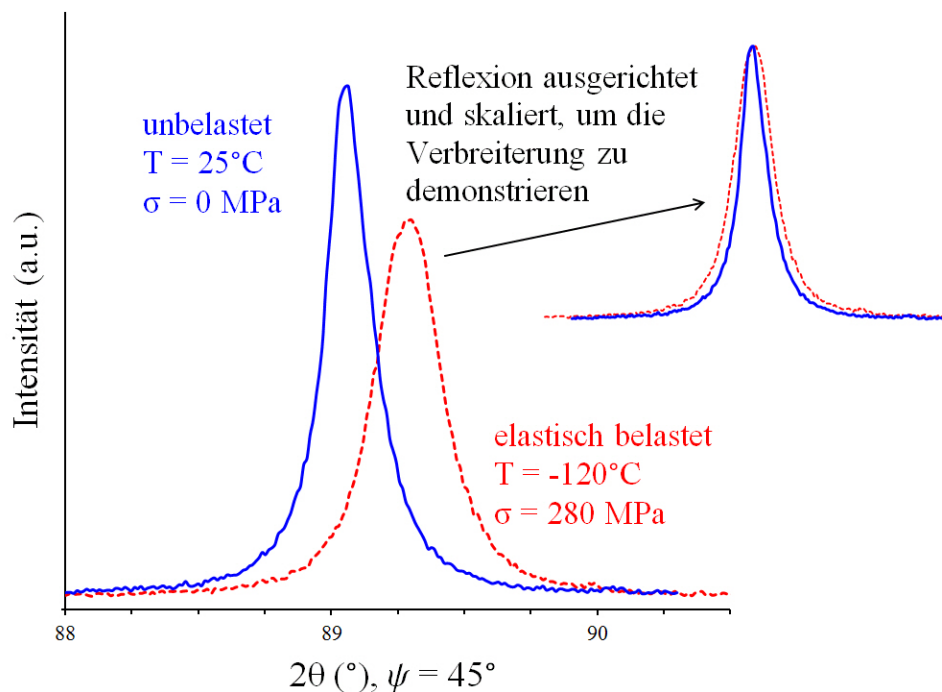


Figure 6.2: Die aufgebrachte Belastung bewirkt (eine Verschiebung und) eine Verbreiterung der 311-Reflexion für einen Cu-Dünnsfilm (bei einem Kippwinkel von  $\psi = 45^\circ$ ; Strahlung  $\lambda = 1.52933 \text{ \AA}$ ). Der Zustand der biaxial rotationssymmetrischen Zugspannung (280 MPa) wurde durch Kühlung auf  $-120^\circ\text{C}$  auferlegt. Das eingeschobene Bild zeigt den Unterschied in der Verbreiterung zwischen belasteten und unbelasteten Zuständen durch Skalieren und Verschieben der Reflex-Maximum Positionen, sodass die Maxima zusammenfallen.

Da sich die Lage der Beugungslinien direkt auf den Gitterabstand eines Satzes von  $hkl$ -Ebenen bezieht, führen Variationen in diesem Gitterabstand (z.B. Variation der Gitterdehnung) zu einer Verbreiterung der gemessenen Beugungslinien der elastisch belasteten polykristallinen Probe. Die Gitterdehnungsvariation, die nach dem elastischen Kornwechselwirkungsmodell berechnet ist, kann auch verwendet werden, um Verbreiterung der Beugungslinien zu bestimmen, die von der induzierten Last (und der entsprechenden

Variation der Gitterdehnung) abhängig ist. Die Analyse der von der Gitterbelastung induzierten Verbreiterung der Beugungslinien kann mehr Informationen über die Art der Kornwechselwirkungen liefern als die "Standard"-Beugungs-Belastungs-Analyse auf Grundlage der Positionen der Beugungslinien, z.B. durch die sogenannte  $\sin^2 \psi$ -Methode.

Die Untersuchung, die in Chapter 3 diskutiert wird, liefert eine detaillierte Darstellung der Synchrotron-Experimente, wobei die Beugungslinien verschiedener elastisch beanspruchter Proben gemessen wurden. Daraus ergeben sich Anzeichen für Gitterdehnungsvariationen innerhalb des Materials, wie in Figure 6.2 gezeigt ist. Vergleiche zwischen experimentellen Daten und Berechnungen für elastische Kornwechselwirkungen bieten Informationen zur Anwendbarkeit der diskutierten Modelle. Die gemessene Verbreiterung der Beugungslinien, induziert durch elastische Belastung, übertrifft bei weitem diejenige, die von den Modellen prognostiziert wird.

Die experimentellen Messungen zeigten außerdem, dass die durch elastische Belastung einer polykristallinen Probe induzierte Gitterdehnungsvariation (beobachtet durch die Verbreiterung der Beugungslinien) nicht vollständig durch die elastischen Kornwechselwirkungsmodelle beschrieben werden kann. Die experimentelle Methode ermöglicht eine hochempfindliche Messung, um die im Korn einer realen Probe auftretenden Kornwechselwirkungen zu untersuchen.

## Die Funktion der Belastung in der Martensit-Austenit Transformation in äquiatomaren NiTi

Nah-äquiatomare Zusammensetzungen von NiTi sind Formgedächtnislegierungen, die sich durch zwei einzigartige Verhalten auszeichnen: die *Pseudoelastizität* (auch Superelastizität genannt) und der *Formgedächtniseffekt*. Diese Materialeigenschaften machen NiTi Dünnschichten einen potentiellen Kandidaten für die Anwendung in mikro-elektromechanischen Systemen (MEMS). Die zwei interessanten Phasen von nah-äquiatomarem NiTi sind der kubische Austenit bei hohen Temperaturen und der monokline Martensit bei niedrigen Temperaturen. Abscheidungsverfahren für Dünnschichten, der Spannungszustand in der Folie und die Materialzusammensetzung haben wesentlichen Einfluss auf das Umwandlungsverhalten des Werkstoffs. Thermische Belastung (d.h. Erhitzen) kann verwendet werden, um die umgekehrte martensitische Phasenumwandlung (von Martensit zu Austenit) einzuleiten. Auch spielen mechanische Belastungen eine wichtige Rolle bei der Phasenumwandlung.

Durch die abrupte Strukturänderung, die mit der Phasenumwandlung verbunden ist, ist das Material prädestiniert für die Untersuchung mittels auf Röntgenbeugung basierenden Techniken. Durch die *in situ* Röntgenbeugung (XRD) wurden Experimente durchgeführt, um Phasenanteil, Belastung und Kristallitgröße der Phasen während der Transformation zu beobachten. Die Analyse der Beugungslinien der XRD-Muster bei diesen *in situ* Experimenten ist eine mächtige Methode. Die Untersuchung in Chapter 4 kon-

zentriert sich auf Synchrotron XRD-Untersuchungen an Substrat-gebundenen NiTi Dünnschichten (49,2(5) at.%Ni.) während des *in situ* Aufheizens. Eine Kombination von XRD-Techniken wurde für die Untersuchung des Phasenanteils (Rietveld Analyse, Figure 6.3) und der Spannung (Krümmung und  $\sin^2 \psi$ -Methoden) als Funktion der Temperatur verwendet. Die Messergebnisse von ähnlichen Proben zeigten eine gute Reproduzierbarkeit.

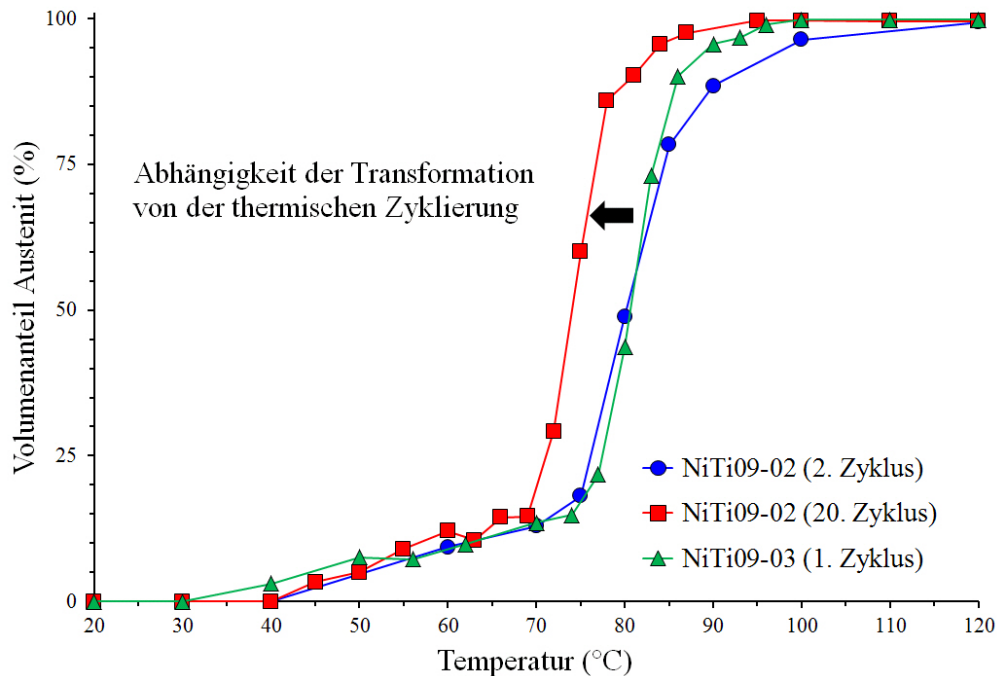


Figure 6.3: Anteil der Austenit-Phase als eine Funktion der Temperatur während der Temperaturzyklen der Rietveld-Analyse.

Bei fortgesetzten Temperaturzyklen werden die Phasenumwandlungstemperaturen niedriger, wie es in Figure 6.3 gezeigt ist. Die Vermutung liegt nahe, dass dieses instationäre Verhalten in einer Erhöhung der Dichte sowohl der Defekte als auch der Versetzungen begründet werden kann. Für die Vorwärtstransformation führt dies zu einer höheren für die Umwandlung nötigen Unterkühlung. Auch der Spannungszustand in dem Film wird durch Temperaturwechsel beeinflusst. Nach zahlreichen Temperaturzyklen reduziert sich die Größe der makroskopischen Spannung in der Folie bei Raumtemperatur (einphasiger Martensit-Film) bis (praktisch) Null, was in dem Verhalten der “self-accommodating” Martensit-Mikrostruktur begründet ist.

Die makroskopische Filmspannung steigt mit der Temperatur. Spannungsbeiträge wurden den jeweiligen Phasen (d.h. Martensit und Austenit) zugeordnet. Dies zeigt, dass die Größe der Spannung in hohem Maße vom Anteil der austenitischen Phase im substratgebundenen NiTi Dünnsfilm abhängig ist. Trotz Erhöhung der Spannung bleibt diese im Austenit durch die gesamte Transformation biaxial und rotationssymmetrisch .





# List of Publications

1. M. K. A. Koker, U. Welzel, and E. J. Mittemeijer, “Elastic mechanical grain interactions in polycrystalline materials; analysis by diffraction-line broadening” *Philosophical Magazine* (submitted October 2012). Chapter 2 of this thesis.
2. M. K. A. Koker, U. Welzel, and E. J. Mittemeijer, “Measurement of x-ray diffraction-line broadening induced by elastic mechanical grain interaction” *Journal of Applied Crystallography* (submitted October 2012). Chapter 3 of this thesis.
3. M. K. A. Koker, J. Schaab, N. Zotov, and E. J. Mittemeijer, “X-ray diffraction study of the temperature-induced reverse martensitic transformation in near-equiatomic NiTi shape memory thin films” *Thin Solid Films* (in preparation). Chapter 4 of this thesis.



# Acknowledgments

The present work was performed at the Max Planck Institute for Intelligent Systems (formerly Max Planck Institute for Metals Research) and at the Institute for Materials Science, University of Stuttgart.

It has been an honor to spend the last three years conducting my research at MPI. I would like to thank Professor Mittemeijer, my *Doktorvater*, for inviting me into his department and for providing me with the professional scientific environment to further myself as a scientist. His continued search for scientific understanding is an inspiration, especially for new scientists entering into the field of research.

I would also like to thank Professor Bill for acting as *Mitberichter* for the thesis defense and Professor Schleid for accepting position of *Chairman* for the defense examination.

I must express my sincere gratitude to Dr. Welzel for his guidance and helpful instruction during my time at MPI. I had much to learn about the field of diffraction, and his patience and support provided me with a wonderful environment for my learning. I am grateful for the permission for measurements at the Synchrotron Light Source ANKA at the MPI beamline for Surface Diffraction. Also, I would not have been able to perform such successful experiments without the technical and scientific support of Ralph Weigel and Miguel Mantilla during my beamtime.

I also extend my gratitude to Gerd Maier and Joseph Bahler for their technical help during beamtime preparation. To the rest of the department, thank you very much for the scientific and community support during my time in Stuttgart. You have provided a delightful working environment.

I am grateful to the International Max Planck Research School for Advanced Materials (IMPRS-AM) for providing part of the financial support for my project.

I am forever in debt to those who support me outside of the field of science. To my parents and my (somewhat extended) family (Walt, Abby, Charlie, Kasia, Tim, . . .), you give me the confidence to always move forward and work harder. Words are not enough to express my gratitude for your encouragement every step of the way. Familie Kaiser, ich danke Euch für Euere Herzlichkeit und die schöne Zeit.

Finally, I'd like to dedicate my thesis in memory of my biggest supporter: my grandpa, a fellow engineer, who passed away this year. His support was always gentle and inspiring.



# Curriculum Vitae

## Personal data

*Name* Margaret Kolbe Annellen Koker  
*Date of birth* 9th of January 1985  
*Place of birth* Lafayette, Indiana, USA  
*Nationality* American

## Education

1999 – 2003 High School Diploma  
Neenah Public High School  
Neenah, Wisconsin, USA

2003 – 2007 Bachelor of Science in Mechanical Engineering  
Department of Mechanical & Aerospace Engineering  
College of Engineering  
Boston University  
Boston, Massachusetts, USA

2007 – 2009 Master of Science in Mechanical Engineering  
Department of Mechanical Engineering & Science  
College of Engineering  
University of Illinois  
Urbana, Illinois, USA

## Dissertation

Sept. 2009 – present  
Title: *Diffraction analysis of materials in a state of stress: elastic loading and phase transformations*  
Max Planck Institute for Intelligent Systems  
(formerly Max Planck Institute for Metals Research)  
Stuttgart, Germany

## Professional experience

Jan. 2006 – Sept. 2006 Design Engineer  
Harley-Davidson Motor Company  
Milwaukee, Wisconsin, USA



# Erklärung über die Eigenständigkeit der Dissertation

Ich versichere, dass ich die vorliegende Arbeit mit dem Titel *Diffraction analysis of materials in a state of stress: elastic loading and phase transformations* selbständig verfasst und keine anderen als die angegebenen Quellen und Hilfsmittel benutzt habe; aus fremden Quellen entnommene Passagen und Gedanken sind als solche kenntlich gemacht.

## Declaration of Authorship

I hereby certify that the dissertation entitled *Diffraction analysis of materials in a state of stress: elastic loading and phase transformations* is entirely my own work except where otherwise indicated. Passages and ideas from other sources have been clearly indicated.

Name/Name: \_\_\_\_\_

Unterschrift/Signed: \_\_\_\_\_

Datum/Date: \_\_\_\_\_